Carbon Nitrides and Metal Nanoparticles: From Controlled Synthesis to Design Principles for Improved Photocatalysis

Ivo F. Teixeira,[1] Eduardo Barbosa,[1] Shik Chi Edman Tsang,[2] Pedro H. C. Camargo[1]

[1]Departamento de Química Fundamental, Instituto de Química, Universidade de São Paulo, São Paulo, SP, Brazil

[2]Wolfson Catalysis Centre, Department of Chemistry, University of Oxford, Oxford, UK

Abstract

The use of sunlight to drive chemical reactions *via* photocatalysis is of paramount importance towards a sustainable future. Among several photocatalysts, earth-abundant graphitic carbon nitride (g-C_3N_4) has emerged as an attractive candidate due to its ability to absorb light efficiently in the visible and near-infrared range, chemical stability, non-toxicity, straightforward synthesis, and versatility as a platform for constructing hybrid materials. Especially, hybrids with metal nanoparticles offer the unique possibility of combining the catalytic, electronic, and optical properties of metal nanoparticles with g-C_3N_4. Here, we provide a comprehensive overview of g-C_3N_4 materials their hybrids, emphasizing heterostructures with metal nanoparticles. We focus on recent advances encompassing synthetic strategies, design principles, photocatalytic applications, and charge-transfer mechanisms. We also discuss how local surface plasmon resonance (LSPR) effect of some noble metals NPs (e.g. Au, Ag, and Cu), bimetallic compositions, and even non-noble metals NPs (e.g., Bi) synergistically contribute with g-C_3N_4 in light-driven transformations. Finally, we provide a perspective on the field, in which the understanding of the enhancement mechanisms combined with truly controlled synthesis can act as a powerful tool to the establishment of the design principles needed to take the field of photocatalysis with g-C_3N_4 to a new level, where the desired properties and performances can be planned in advance, and the target material synthesized accordingly.

1. Introduction

The adverse environmental problems caused by the intensive consumption of fossil fuels have led to an increasing interest in the use of alternative energy sources to serve and deliver power to human activities.[1-3] Solar energy has an enormous potential as a clean, abundant, and economical resource.[4] Therefore, the efficient harvesting and conversion of solar energy have been a worldwide priority target in the past decade.

In this context, the use of sunlight to drive chemical reactions (solar to chemical energy conversion) *via* photocatalysis represents a very promising approach.[5] In photocatalysis, the most studied examples are endothermic reactions, such as H_2O splitting and CO_2 reduction, where the energy of solar photons can be stored in chemical bonds by using semiconductors as photocatalysts.[6, 7] Even though a lot of progress has been achieved in the development of semiconductor photocatalysts, most systems require solar energy input in the UV region for band gap excitation.[8-10] Thus, most photocatalysts present low solar-energy utilization, as solar light is composed of ultraviolet, visible and infrared components (accounting for 5, 43, and 52 %, respectively).[11] These features illustrate that is still very challenging design new photocatalysts that are abundant, stable, facile to fabricate, and showing high performances under visible-light or near-infrared excitation.[10]

The search for suitable semiconductor photocatalysts to optimise existing or design novel chemical processes is one of the persistent goals of sustainable chemistry. An optimal material would combine an ability to absorb light efficiently, especially in the visible and near-infrared range, and be stable in working chemical and thermal conditions. Moreover, it should be non-toxic, preferentially composed by abundant elements, and easily processable. Mostly explored semiconductors are so far constructed from transition metal ions with d^0 or d^{10} electronic configuration, along with counter-anion such as chalcogens.[12, 13] However, it remains challenging to engineer and tune the electronic properties of metal chalcogenides. As a result, rarely these structures have been targets of systematic optimisation.[14, 15] Traditional inorganic semiconductors are limited in the nature of their active sites and thus the scope of applications that they can accomplish.[16, 17] On the other hand, while organic polymeric catalysts have the advantage of flexibility for optimization, they suffer from serious swelling and stability problems.[17] Consequently, it is extremely desirable to have an active and stable photocatalyst that could allow large variation in the structure without having to change its overall composition.

Graphitic carbon nitride (g-C_3N_4) is a highly active photocatalyst which, at least in principle, meets above-mentioned requirements. The history of C_3N_4 can be traced back to the embryonic form, “melon”, made by Berzelius and named by Liebig in 1834 being regarded as one of the oldest synthetic polymers.[14, 16, 18] The framework topology of linear polymer “melon” is presumably consisting of interconnected tri-s-triazines *via* secondary nitrogens, while defect-rich C_3N_4 is in the form of p-conjugated planar 2D sheets of poly(tri-s-triazines) interconnected *via* tertiary amines.[18, 19] The “perfect” g-C_3N_4 material is comprised solely of C and N bonds with no active basicity, due to the lack of electron localized in the π state.[20] However, it is difficult to synthesize “perfect” g-C_3N_4. In general, most of the synthesis routes lead to predominantly materials with medium to poor crystallinity and a high degree of disorder, but still showing high photocatalytic activity.[14-16] Bulk g-C_3N_4 is typically prepared by the direct thermal condensation of low-cost nitrogen containing precursors (cyanamide, dicyandiamide).[21-24] This results in carbon nitrides with several shortcomings, including low specific surface area, insufficient visible light utilization, and, particularly, rapid recombination of photogenerated charge carriers.[24-28] High separation/transfer efficiency of photogenerated electron-hole pairs is the most desirable property in g-C_3N_4-based photocatalysts. Several strategies can be employed to achieve this objective, such as *i*) doping the C_3N_4 structure with sulphur,[29, 30] boron,[31] oxygen[32] and phosphorous[29, 33, 34]; *ii*) modifying its synthesis method (e.g. changing and combining different nitrogen containing precursors,[18, 35, 36] introduce mesoporous using hard templates,[37, 38] microwave-assisted synthesis,[39] synthesis in molten salt,[40] synthesis in ionic liquid[41]); *iii*) performing a post treatment (e.g. exfoliation[42-45] and thermal treatment[18, 35, 36]); *iv*) controlling the defects in its structure;[46] *v*) and/or combining it with other structures (e.g. semi-conductors,[24, 47-51] metal nanoparticles (NPs)[24, 52-54] and metal-organic frameworks (MOFs)[23, 55-57]).

Among the recent strategies in the development of g-C_3N_4 photocatalytic systems, g-C_3N_4-based heterostructures are one the most promising materials due to its feasibility and effectiveness for the spatial separation of photogenerated electron-hole pairs.[24] The g-C_3N_4-based heterostructures are capable to suppress the recombination of photogenerated charge carriers while endowing the photocatalysts with unique features that arise from the synergism between g-C_3N_4 and the other components. Therefore, we believe that the rational design of g-C_3N_4-based heterostructures could provide promising routes for creating highly efficient visible-light-driven photocatalysts for chemical synthesis, environmental remediation, and energy applications.

Herein, we aim at providing a general overview on heterostructures comprised of g-C_3N_4 and metal NPs. The synthesis, applications in photocatalytic reactions, and the mechanisms behind the synergistic effects involving g-C_3N_4 and metal NPs will be covered. This review will also focus on how local surface plasmon resonance (LSPR) effect of some noble metals NPs (e.g. Au, Ag, and Cu), bimetallic compositions (AuPd, AuAg, AuPt, etc), and even non-noble metals NPs (e.g., Bi) can enhance the catalytic properties of g-C_3N_4 in several light-driven transformations.

2. Synthesis of g-C_3N_4

g-C_3N_4 is commonly synthesized by thermal treatment that leads to a combination of polyaddition and polycondensation reactions of the nitrogen-rich precursors such as urea, thiourea, melamine, cyanamide, and dicyandiamide.[58-64] This approach is described in **Fig. 1**. The precursors condensate into dicyandiamide **1** and melamine (triamino-*s*-triazine) **2**, which forms tri-*s*-triazine units, also known as melem **3**, by polycondensation of melamines. Then, the g-C_3N_4 **4** are formed through the further condensation of the tri-*s*-triazine units.[28, 65]

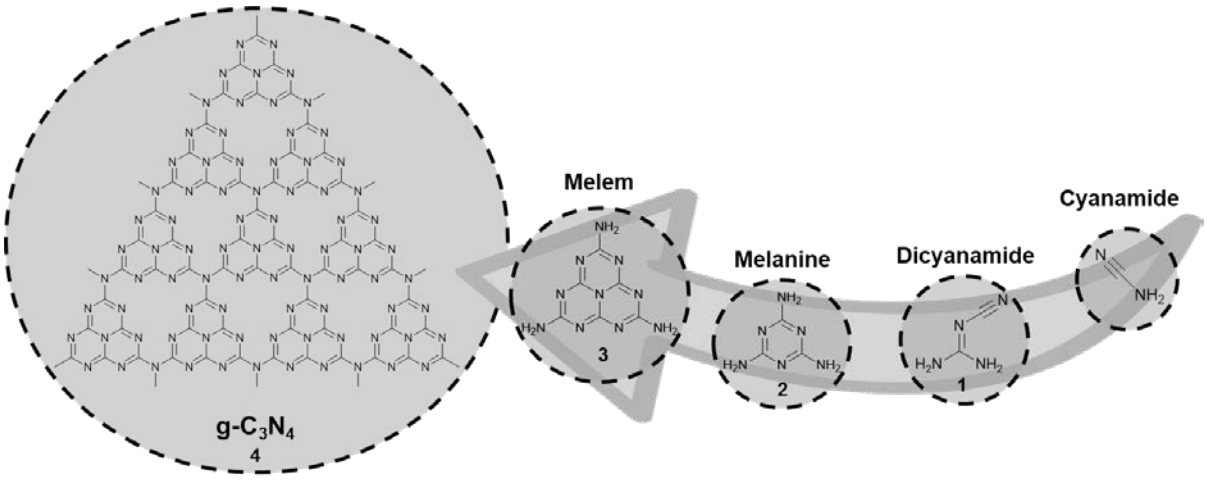

Figure 1. Schematic illustration for the synthesis of g-C_3N_4 by polyaddition and polycondensation of the nitrogen-rich precursors.

Interestingly, it has been established that the choice of precursors significantly influences the electronic band structures and textual properties of obtained pristine bulk g-C_3N_4.[24] For example, when thiourea is used to prepare the g-C_3N_4, it exhibits a slightly smaller bandgap when compared with the g-C_3N_4 prepared from urea.[66, 67] On the other hand, the g-C_3N_4

prepared from urea generally presents much higher specific surface area than that prepared from thiourea and melamine.[18, 66]

Another aspect is that the g-C_3N_4 properties strongly depends on the nitrogen-rich precursors and temperature employed during the thermal polymerization, which represents an attractive method due to its simplicity and low cost. The nitrogen-rich small molecules polymerize into g-C_3N_4 in temperatures ranging between 450 and 650 °C.[24, 66, 68] Bellow 450 °C, the polymerization is incomplete. Over 650 °C, the g-C_3N_4 start to decompose.[59] Different precursors calcined at different temperatures can lead to a range of band-gaps and specific surface areas. For instance, urea can produce g-C_3N_4 with band gaps varying from 2.68 to 2.78 eV and surface areas from 31 to 288 m^2 g^{-1}, while thiourea can lead to carbon nitrides with band gaps from 2.58 to 2.76 eV and surface areas significantly smaller 11-52 m^2 g^{-1}.[18] It is important to highlight that these examples involve only the modification in the nature of precursors and calcination temperature. Many other approaches can also be employed to tune carbon nitride properties, such as doping the C_3N_4 structure,[29-34] introduce mesoporous using hard templates,[13, 37, 38] using other synthesis methods apart from thermal condensation,[39-41] adding a post-treatment (e.g. exfoliation[42-45] and thermal treatment[18, 35, 36]), controlling the defects in its structure,[46] and combining it with other structures, such as semiconductors,[24, 47-51] metal NPs,[24, 52-54] and metal-organic frameworks (MOFs).[23, 55-57]

The successful preparation of g-C_3N_4 photocatalysts can be confirmed by several analytical measurements, such as X-rays diffraction (XRD), X-ray photoelectron spectroscopy (XPS) and thermogravimetric analysis (TGA). XRD is an important technique due the two characteristic diffraction peaks at ca. 27.4 and ca. 13.0° that appear for the g-C_3N_4.[18] XPS measurements are especially useful to investigate the chemical environment of carbon and nitrogen elements in g-C_3N_4, evidencing sp^2-bonded carbon in N-C=N (ca. 288.1 eV) and the sp^2-bonded nitrogen in C-N=C (ca. 398.7 eV). Furthermore, XPS allows to characterize elemental doped g-C_3N_4 and estimates the degree of defects in the g-C_3N_4 structure by the nitrogen in tertiary nitrogen groups (ca. 400.3 eV) and the presence of amino groups (C–N–H, ca. 401.4 eV). Because the high thermal stability of g-C_3N_4, the decomposition temperature obtained by TGA can be a simple way to confirm the proper polymerization of the nitrogen-rich precursors[18]

3. Properties

3.1 Morphological features

As a polymer, g-C_3N_4 has a flexible structure and is suited to form different morphologies with the assistance of different templates during the synthesis as well as post-treatments. However, differently from most polymeric materials, g-C_3N_4 can endure high temperatures (until 650 °C), even in oxidizing atmosphere.[66] g-C_3N_4 have been obtained in several morphologies, such as porous g-C_3N_4 (3D nanostructures),[37, 38, 69] hollow spheres,[70] nanorods/[71]nanowires/[72]nanotubes[73] (1D nanostructures), and nanosheets (2D nanostructures).[45, 74]

Mesoporous carbon nitrides (mpg-C_3N_4) can be easily obtained by a hard template method. It has been successfully synthesized using various nitrogen-rich precursors in the presence of silica NPs [37, 38] or ordered mesoporous silica (e.g. SBA-15)[69] as a hard template. The removal of those silica structures by a treatment with HF then generates a 3D structure of g-C_3N_4 with a large surface area, which can reach up to 373 m^2 g^{-1}.[18] The mpg-C_3N_4 synthesis, functionalization, and applications was recently reviewed by Lakhi and colleagues.[75]

The preparation of hollow g-C_3N_4 spheres is challenging due to its layered structure, which is more susceptible to collapse. However, Sun *et al.*[70] were successful in coating monodisperse silica NPs with thin mesoporous silica shells and then used it as a hard template to prepare hollow g-C_3N_4 nanospheres. This strategy is similar to the one used to prepare mesoporous g-C_3N_4. The silica was then removed by a post-treatment with HF at the end of the synthesis. g-C_3N_4 in the form of hollow spheres are very attractive because they are able to harvest more incident light through successive reflections within the hollow structure, producing more photoinduced charge carriers serving as light-harvesting antennas.[18]

1D nanostructured g-C_3N_4 such as nanorods, nanowires, nanobelts, and nanotubes are also attractive morphologies because their length, diameter, and aspect ratio can be tuned. This, in turn, can lead to unique and tunable chemical, optical and electronic properties.[18] 1D nanostructured g-C_3N_4 displaying porous structures, large surface areas, and charge-carrier mobility can be prepared using different templating (e.g. SBA-15)[69, 71] or non-templating (e.g. reflux in solvent)[73, 76, 77] methods.

Bulk g-C_3N_4 display a low specific surface area, corresponding to <10 m^2 g^{-1}, due to the stacking of g-C_3N_4 layers. Thus, several studies have been focused on exfoliation methods to obtain nanosheets from bulk g-C_3N_4. The most common strategies include ultrasonication-assisted liquid exfoliation,[43, 45, 74, 78-83] acid exfoliation,[84, 85] liquid ammonia-assisted lithiation,[79] and thermal oxidation.[43, 86] 2D g-C_3N_4 nanosheets exhibit interesting features, such as large specific surface areas, prolonged lifetime of charge carriers, enhanced electron transport property, reduced recombination rate of charge carriers, and improved charge transfer and separation efficiencies.[28] Due to the combination of these very attractive features, it represents the most studied g-C_3N_4 morphology.

3.2 Surface Basic and Acid Sites

Among the several features of g-C_3N_4, the presence of acid and basic sites in its surface is one of the most interesting but poorly understood properties. g-C_3N_4 has Lewis basic sites (**Fig. 2a**), which can be the nitrogen present in the six-membered ring (**A**) or nitrogen present as primary (**C**) and/or secondary (**B**) amine groups on the terminating edges due to defects in the g-C_3N_4 structure.[59] The surface basicity of g-C_3N_4 can be confirmed by temperature-programmed desorption of CO_2 (CO_2-TPD).[59] This powerful technique also allows differentiate and estimate the amount of the three basic site types. These basic sites can be applied to catalyze several reactions, such as C−C coupling,[37] α−C-H activation,[31] NO decomposition,[87] and Knoevenagel condensations.[20, 88-90]

The formation of Brønsted acid sites on g-C_3N_4 surface under oxidation conditions was first proposed by Shiraishi *et al.*[91] in 2014 by the approach shown in **Fig. 2b**. Ever since, many recent studies have confirmed the presence of highly labile hydrogen adsorption sites at the g-C_3N_4 edges under photooxidation conditions (O_2 atmosphere and light) in the presence of alcohol, which can be the substrate or the solvent in the reaction.[92, 93] These Brønsted acid sites were recently confirmed experimentally by post-mortem temperature programmed desorption and *in-situ* X-ray photoelectron spectroscopy analysis (XPS), which indicates H_{ads} weakly adsorbed on the catalyst surface.[92] This same study also confirmed the presence of H_{ads} on g-C_3N_4 by semi-empirical MOPAC2016 calculations and estimated the relative adsorption energies of H pairs (two H atoms) on a model crystalline g-C_3N_4 structure consisting of two H-bonded strips with 6 melem units, which evidenced that the Brønsted acid sites are more likely to be present at the edges of the g-C_3N_4 and bonded to N atoms in

the same ring adjacent to the bridging N atoms between melem units, as shown in **Fig. 2b**.[92] The Brønsted acid sites can be applied to catalyse a series of reactions, especially those which depend on a dehydration, which include the conversion of nitroaromatics into azo- and azoxyaromatics[92] and the photoacetalization of ketones and aldehydes.[93] Moreover, Lewis acid sites can be introduced into g-C_3N_4 by elemental doping with boron[31, 94-96] or phosphorous.[29, 33, 34, 97] Despite that fact that Lewis acid sites are less active than the Brønsted ones, they presented helpful synergistic effects in a range of photoreactions, such as H_2 evolution,[34, 94] photodegradation,[34, 96] photooxidations,[95] C-H activations[31] and CO_2 cycloaddition.[97]

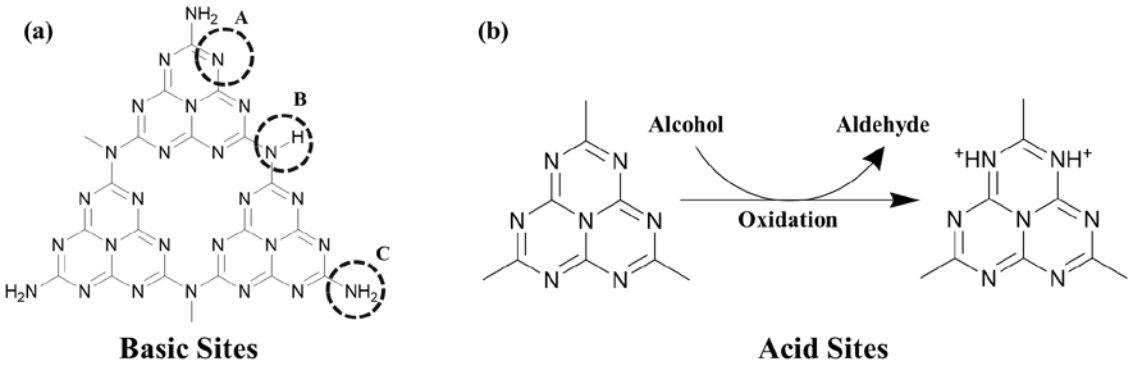

Figure 2. Acid and basic sites on g-C_3N_4 surface. (a) Lewis basic sites present on the g-C_3N_4 surface: N in six-membered ring (**A**), secondary amine (**B**), and primary amine (**C**).[59] (b) Proposed mechanism for the formation of Brønsted acid sites on the g-C_3N_4 surface.[91]

4. g-C_3N_4 Based Heterojunctions: Non-Noble Metals, Metal Oxides, Metal Sulphides, and Metal-Organic Frameworks

Elemental doping is widely used to engineer the band gap of g-C_3N_4 through the addition of other elements instead of C and N in the g-C_3N_4 structure. This makes it possible to modulate the light absorption and redox band potentials for targeted photocatalytic applications according to **Fig. 3**.[28] As previously mentioned, the most commonly used elements are S,[29, 30, 98] B,[31, 96] O,[32] I[29, 99, 100] and P.[29, 33, 34] However, metal cations also can be included into g-C_3N_4 framework, such as Zn^{2+}, Fe^{2+},[101] Ni^{2+}, Cu^{2+}, Co^{3+},[102] Cu^{1+},[103] Mn^{3+}, K^+,[104] Na^+ and Li^+.[105-108] The recent review by Zhang *et. al*. provides a detailed discussion of several strategies that can be employed to obtain g-C_3N_4 structures and how they affect photocatalytic activities.[109] In another interesting review Jiang and collaborators overview the

recent advances in doping of g-C_3N_4 for photocatalytic applications.[110] Among them, we believe that an efficient way to improve the g-C_3N_4 electronic properties is by combining it with other semiconductors and nanostructures to form g-C_3N_4 based heterojunctions.

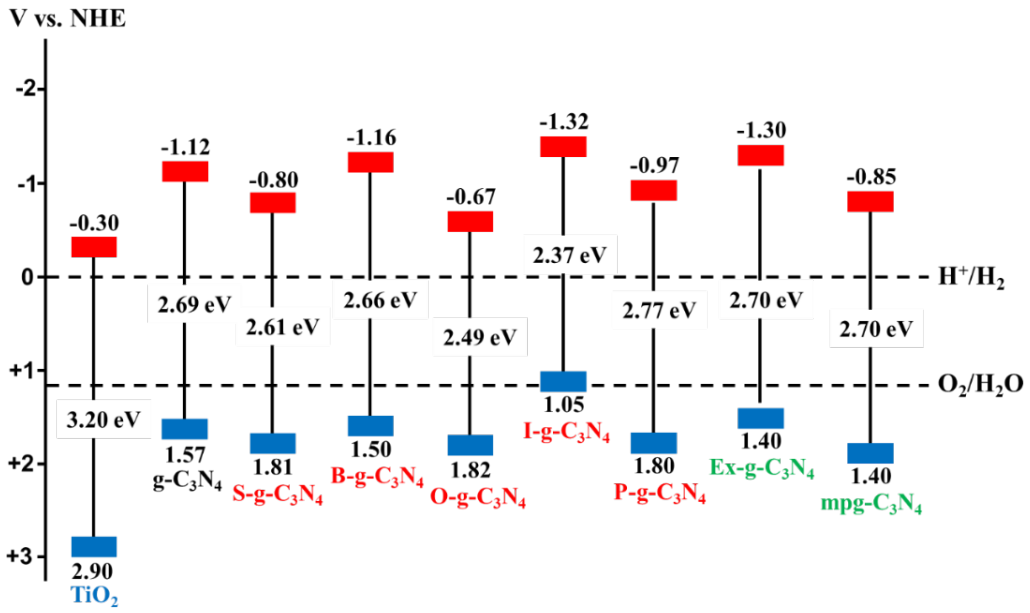

Figure 3. Schematic illustration of the band structure of typical g-C_3N_4 samples, including g-C_3N_4,[111] S-g-C_3N_4,[98] B-g-C_3N_4,[96] O-g-C_3N_4,[32] I-g-C_3N_4,[29] P-g-C_3N_4,[33] ex-g-C_3N_4,[112] mpg-C_3N_4.[113] The band structure for TiO_2 is also shown for comparison. Adapted from ref 18. Copyright 2015 John Wiley & Sons, Inc.

Similarly to other typical inorganic semiconductor photocatalysts (e.g., TiO_2), g-C_3N_4 also suffers several intrinsic drawbacks such as low electrical conductivity, high recombination rate of electron-hole pairs, and limited absorption above 460 nm.[114] Highly efficient g-C_3N_4-based nanostructures must attend some important criteria. These include low recombination rates, enhanced solar light absorption, and high photochemical stability. In this context, the development of g-C_3N_4-based nanohybrids is attractive for several reasons: *i*) in enables more efficient charge transfer and separation through the Schottky junction (metal/semiconductor heterostructures) or the p-n junction (semiconductor/semiconductor heterostructures); *ii*) the presence of cocatalysts lowers the redox overpotential at the active sites; *iii*) the visible light utilization can be improved; and *iv*) the system stability by protecting the active sites and functional groups on the surface of the semiconductor through proper surface passivation is ameliorated.[28]

It is well established that charge recombination processes are disadvantageous to the photocatalytic efficiency. When the recombination process takes place, excited electrons return to the valence band, dissipating the energy as heat without reacting with the adsorbed species on the surface of g-C_3N_4. Thus, many strategies have been investigated to suppress recombination in g-C_3N_4 and consequently improve the photocatalytic performances.[28] Among them, the construction of g-C_3N_4-based heterojunction nanohybrids is particularly appealing has received a lot of attention in the field of photocatalysis. This strategy will be discussed in the subsequent sections.

4.1. g-C_3N_4 and Noble-metal Free Materials

Noble-metal free materials (e.g. g-C_3N_4, graphene, carbon nanotubes, etc) have various advantages, such as being low cost and environmentally friendly. Hence, they have attracted tremendous attention to their potential in tacking environmental and energy problems. Thus, it becomes attractive to construct hybridized materials *via* coupling two noble-metal free materials. For example, graphene, a two-dimensional macromolecular sheet of carbon atoms, has received much attention due to its outstanding mechanical, thermal, easily-obtained, and electrical properties.[115, 116] Thus, it represents an intuitive noble-metal free candidate to construct heterojunction nanohybrids with g-C_3N_4.[117]

Sun *et al.* prepared graphene/g-C_3N_4 heterojunctions which presented enhanced conductivities and electrocatalytic performance towards the oxygen reduction reaction (ORR).[118] Xiang *et al.* obtained graphene/g-C_3N_4 nanohybrids by a combined impregnation-chemical reduction strategy, and successfully tested it towards the photocatalytic H_2-production in the presence of Pt as a cocatalyst under visible light.[117, 119] Li and collaborators synthesised cross-linked g-C_3N_4/rGO (reduced graphene oxide) nanohybrids with tunable band structure, which demonstrated significantly enhanced visible light photocatalytic activity.[120] In another example, Ong *et al.* have assembled rGO and g-C_3N_4 for successful CO_2 hydrogenation into methane.[121] Other successful attempts have been made to explore novel materials coupling carbon nanostructures with g-C_3N_4, such as MWNTs (multi-walled carbon nanotubes)/g-C_3N_4,[122, 123] C_{60}/g-C_3N_4,[124, 125] carbon nanodots/g-C_3N_4[126-131] and polymers/g-C_3N_4.[132-137]

Another carbon structure that has gained huge attention recently is carbon nanodots. They present excellent optical and electronic features, acting as both light absorbers and electron

reservoirs.[126] Different methods have been used to synthesize carbon nanodots on g-C_3N_4, such as hydrothermal[138] and pyrolysis.[126] Due to the unique nature of carbon nanodots as spectral converters, they allow for the up conversion of infrared light to visible light. The emitted light can then be used by the g-C_3N_4 for various photo-driven transformations. Carbon nanodots can also be employed as a cocatalyst in some reactions. For example, H_2O_2 is a typical intermediate of photocatalytic water splitting and its adsorption on the surface of the g-C_3N_4 results in the poisoning of the active sites. When carbon nanodots are added on g-C_3N_4 surface, the photocatalyst maintain a high activity during the entire process.[128]

It is important to mention noble-metal free heterojunctions between carbon nitrides displaying different electronic structures. For instance, Wang *et al.* obtained two types of host-guest CN/CNS heterojunctions with a facile band alignment by the surface-assisted polymerization: CNS-CN (CN serving as the host) and CN-CNS (CNS serving as the host).[139] This heterojunction is called isotype heterojunctions. Interestingly, these two types of CN/CNS heterojunctions have demonstrated significant enhancement in the photocatalytic activity and stability for H_2 evolution. Inspired by Wang's work, Dong *et al.* synthesised layered g-C_3N_4/g-C_3N_4 metal-free isotype heterojunction by treating the molecular composite precursors of urea and thiourea under the same thermal conditions. This CN-T/CN-U heterojunction was constructed on the basis that the g-C_3N_4 prepared from urea and thiourea have different band structures. Upon visible light irradiation, the photogenerated electrons transfer from g-C_3N_4 (thiourea) to g-C_3N_4 (urea). This is driven by the conduction band offset of 0.10 eV. Also, the photogenerated holes transfer from g-C_3N_4 (urea) to g-C_3N_4 (thiourea) driven by the valence band offset of 0.40 eV.[35] These two charge transfer processes are beneficial for overcoming the high dissociation barrier of the Frenkel exciton and for the stabilization of electrons and holes. The redistribution of electrons on the one side of the heterojunction (CN-U) and holes on the opposite side (CN-T) reduces the electron-hole pair recombination, extending the lifetime of charge carriers and resulting in noticeably higher photocatalytic activity. These two examples demonstrated that the rational design and construction of isotype heterojunctions could open new strategies to development of more efficient visible-light photocatalysts.[117]

4.2. g-C_3N_4 and Metal Oxides or Sulphides

During the past few years, many groups have reported different types of heterojunction photocatalysts comprised of g-C_3N_4 and metal oxides or sulphides showing improved efficiencies relative to their individual components.[24, 28, 117, 140 141]

Among abundant metal oxides, TiO_2 (e.g. 3.2 eV), which represents one of the most widely used photocatalyst, has been employed as a promising candidate for constructing g-C_3N_4 based heterojunctions. Several studies on the successful formation of TiO_2/g-C_3N_4 hybrid nanohybrids have been reported to enhance photocatalytic activities.[142-153] Zhou *et al.* reported the synthesis of TiO_2 nanotube array/g-C_3N_4 heterojunction photocatalysts by a facile electrochemical approach.[47] Recently, heterojunctions between g-C_3N_4 and TiO_2 with different morphologies (0D nanoparticles, 1D nanowires, 2D nanosheets, and 3D mesoporous crystals)[154] and exposed facets ({001} and {101}) have been reported.[144, 155-159] Besides the incorporation anatase TiO_2 with g-C_3N_4, other TiO_2 crystal phases such as brookite and rutile have been coupled with g-C_3N_4 for photocatalytic applications.[160-162]

In addition to the widely reported TiO_2/g-C_3N_4 photocatalysts, ZnO/g-C_3N_4 have also been reported (ZnO presents a band gap of around 3.2 eV).[163-166] Several examples on the synergism between ZnO and g-C_3N_4 have been observed, such as increase in photocurrent of ZnO/g-C_3N_4 hybrid nanomaterials by 5 folds under visible light irradiation ($\lambda > 450$ nm)[48] and the use of N-doped ZnO/g-C_3N_4 core-shell nanoplates for visible-light photodegradation of Rhodamine B (RhB).[167]

Differently from TiO_2 and ZnO, WO_3 has a relatively lower band gap of ca. 2.6-2.8 eV, which lies in the visible light region. Therefore, WO_3/g-C_3N_4 heterostructures exhibits the Type II heterojunction charge transfer process, which drastically suppress the recombination of charge carriers.[168-170] It is noteworthy that other oxides have also been employed to generate g-C_3N_4 based hybrids, such as Cu_2O/g-C_3N_4 (which promoted a red-shifted in the absorption edge from 460 to 600 nm)[171], Fe_2O_3/g-C_3N_4 (makes the material magnetically recoverable and improves photoredox activity),[172] and the Co_3O_4 /g-C_3N_4 water oxidation catalysts displaying high stabilities.[173] Hybrid photocatalysts containing composite oxides have also been receiving attention. For instance, Bi_2WO_6 has been the most widely employed example. Ge *et al*. prepared Bi_2WO_6/g-C_3N_4 heterostructured photocatalysts, which presented a strong light absorption in the visible region.[174] The synergistic effect between g-C_3N_4 and Bi_2WO_6 promoted the charge transfer and separation due to the joined electric fields, whereby the excited electrons from g-C_3N_4 were injected into the conduction band of the

Bi_2WO_6. Simultaneously, the holes on the valence band of Bi_2WO_6 were transferred to that of g-C_3N_4, retarding charge recombination.[28]

In addition to metal oxides, cadmium sulphide (CdS) is a fascinating semiconductor with a relatively low band gap of 2.4 eV, which makes it able to absorb solar light up to 520 nm or even longer wavelengths.[175] The well-matched energy levels of g-C_3N_4 and CdS allows for the formation of heterostructures through the Type II band alignment, which enables charge migration transfer upon light irradiation.[28, 176, 177] To date, CdS/g-C_3N_4 materials, that are composed of two visible light responsive semiconductors, have been fabricated *via* an *in situ* precipitation-deposition method developed by Fu *et al.* The resulting CdS/g-C_3N_4 heterostructure exhibited outstanding visible light photocatalytic in 4-aminobenzoic acid removal.[178] Other studies have also reported higher stability and inhibition of photocorrosion of CdS when it is combined with g-C_3N_4.[179, 180] Two-dimensional (2D) MoS_2 nanosheets have become a promising cocatalyst to produce hybrid photocatalysts with g-C_3N_4. MoS_2 nanosheets are robust, highly active (especially for the H_2 evolution reaction), can be obtained in the layered morphology, and it is relatively inexpensive.[181-183] Interestingly, under the same loading of cocatalysts (MoS_2 or Pt), it has been shown that MoS_2/g-C_3N_4 outperformed the Pt/g-C_3N_4 for H_2 production under similar experimental conditions.[50] Mechanistic investigations extensively examined the interface region between g-C_3N_4 and MoS_2. These studies concluded that valence band maximum and conduction band minimum of g-C_3N_4 were greater by ca. 0.15 and 0.83 eV, respectively, relative to MoS_2. This led to the formation of a Type II heterojunction system.[184] As the charge redistribution occurs preferentially at the heterointerfaces, a polarized field is created at the interface region, which inhibited the recombination of charge carriers and prolonged the lifetime of photogenerated charge carriers.[28, 184] Apart from CdS and MoS_2, many other sulphides have been employed for improved charge separation in hybrids with g-C_3N_4. These include WS_2/g-C_3N_4,[50, 185] SnS_2/g-C_3N_4,[186] NiS_2/g-C_3N_4,[187] CoS/g-C_3N_4,[188] ZnS/g-C_3N_4,[189-191] and Ag_2S/g-C_3N_4.[192]

4.3. g-C_3N_4 and metal-organic frameworks (MOF)

Metal-organic frameworks (MOFs) are compounds composed by metal ions coordinated to organic ligands to form one-, two-, or three-dimensional structures. Similar to what has been described for metal oxide and sulfide semiconductors, MOF materials can photogenerate holes and electrons upon visible-light irradiation, which can lead to the

transfer of holes and electrons to target reactant molecules to initiate light-driven photoredox processes.[28, 193] In terms of band structures, the MOF's valence band correspond to the outer orbitals of organic linkers, whereas the empty outer orbitals of the metal contribute to the conduction band. In this context, the incorporation of MOFs with g-C_3N_4 is interesting due to the variety of MOF structures and species as well as their tunable cavities, porosities, and high surface areas. Several successful examples of MOF/g-C_3N_4 systems have been reported, including MIL-125(Ti)/g-C_3N_4,[56] ZIF-8/g-C_3N_4,[194] and UiO-66/g-C_3N_4.[55] These systems have shown improved photocatalytic activities, high porosity and surface area, thermal stability and accelerated mass transfer processes relative to g-C_3N_4.[57, 195]

5. g-C_3N_4 based Heterojunctions with Metal NPs

5.1. Plasmonic Photocatalysis with Metal Nanoparticles (NPs)

Among all classes of nanomaterials, metals deserve special attention. They represent almost two-thirds of all elements in the periodic table. Moreover, metal nanostructures display remarkable chemical, electronic, optical and magnetic properties that have enable novel and/or improved applications in areas such as catalysis, electronics, plasmonics, biomedicine, separation, information storage, and biomedicine.[5, 196-203]

Some metals, such as silver (Ag) and gold (Au), present remarkable optical properties in the visible range. These properties probably represent one of the most visual examples of property change as we transition from the macro to the nano dimension. The unique optical properties of Ag and Au in the visible and near-infrared range occur as a result of their localized surface plasmon resonance (LSPR) excitation, and enable applications in areas such as surface-enhanced Raman scattering (SERS), plasmonic photocatalysis, plasmon-enhanced fluorescence, the development of plasmonic solar cells, water splitting, and theranostics.[204] The LSPR refers to the oscillation of free charges on a metallic nanoparticle relative to the static nuclei in response to an oscillating electric field from an incoming electromagnetic wave (**Fig. 4**).[205]

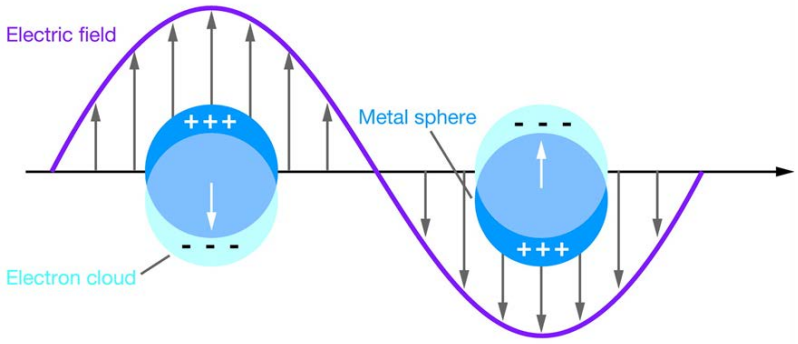

Figure 4. Schematic diagram illustrating the localized surface plasmon. Reprinted with permission from ref [206]. Copyright 2018 Annual Reviews.

Upon electromagnetic irradiation, the oscillating electric field component of light imposes a force onto the conduction electrons of the nanoparticle, which results in the formation of an induced dipole moment. In order to counterbalance this excitation, charge redistribution acts to provide a restoring force on the free electrons, thus granting these NPs an associated resonant frequency at a specific wavelength. The LSPR frequency is dependent on size (**Fig. 5a**), shape (**Fig. 5b**), composition (**Fig. 5c**), and structure of the nanoparticle as well as and the dielectric constant of the environment.[205,196] The LSPR excitation leads to absorption and scattering of the incoming electromagnetic wave at frequencies close to the LSPR resonance together with the generation of intense electric fields close to the surface of the nanostructure. **Fig. 5a** displays the influence of size in Ag nanocubes over the LSPR resonance position. From the extinction spectra (that combines absorption and scattering), the LSPR band red shifted as size increased. This red shift can be assigned to the increased charge separation during plasmon oscillation as size increased. **Fig. 5b** shows the influence of Ag NPs shape their optical properties, illustrating that the optical properties are very sensitive over nanocrystal shape.

Among the metals, Ag, Au, and cooper (Cu) display LSPR in the visible and/or near-infrared range (**Fig. 5c**). Because of this, these systems have been receiving increasing attention in the field of photocatalysis.[207-209] In addition, non-noble metals such as Al, Bi, Ga, In, Pb, Th, and Sn have also been receiving attention.[210] These elements normally present LSPR at the UV region. In one example to circumvent this limitation, the LSPR excitation Al has been already expanded onto the visible side of the spectrum by tuning nanocrystal shape.[211-216]

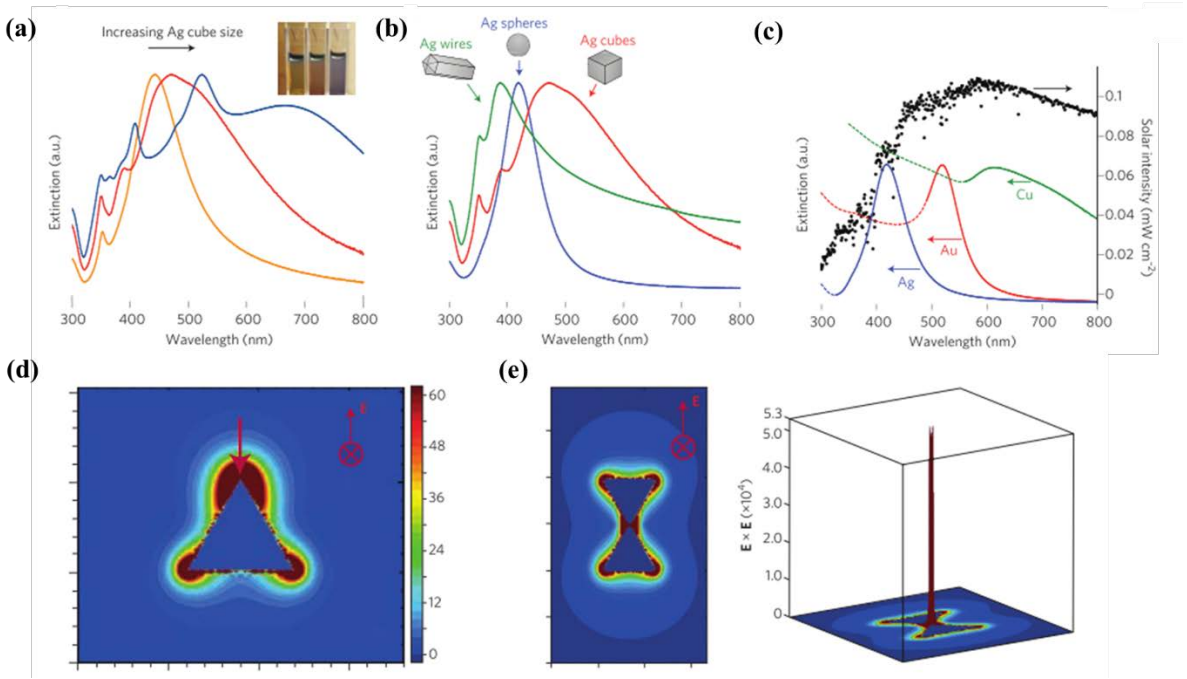

Figure 5. (a) LSPR extinction spectra as a function of size recorded for Ag nanocubes. (a) LSPR extinction spectra as a function of shape recorded for Ag nanowires, nanospheres, and nanocubes. (c) LSPR extinction and solar spectra (black) for Ag, Au and Cu NPs. Reprinted with permission from ref [217]. Copyright 2015 Springer Nature. (d) Simulated electric field enhancement distribution contours around an isolated silver nanoprism with a 60 nm edge length, excited at 700 nm. (e) Simulated electric field enhancement distribution contours for a nanoprism dimer in a tip-to-tip configuration. The two Ag nanoprisms are set 2 nm from each other, and the 3D plot emphasizes the magnitude of field enhancement on the 'hot spot'. Reprinted with permission from ref [218]. AIP Publishing.

It has been recently established that the LSPR excitation in plasmonic nanoparticles can be put to work towards the enhancement in the rates of several chemical transformations .[5, 217] This field, named plasmonic catalysis or plasmonic photocatalysis, has emerged as a new frontier in the field of catalysis and allows for the utilization of visible light as an abundant and green energy input to drive and, at least in principle, control chemical reactions. [203, 217, 219] Importantly, plasmonic photocatalysis allows one to overcome some of the intrinsic limitations of conventional semiconductor photocatalysts, such as short-range light response, low light absorption, and high photo-generated carrier recombination rates. Photocatalytic transformations on plasmonic metallic nanostructures are singular in several respects, exhibiting different behavior as compared with semiconductors.[220] Initial studies have revealed that the rates of photocatalytic reactions on excited plasmonic metallic

nanostructures may show a super-linear power law dependence on light intensity (that is, rate is proportional to intensity^n, with n>1).[203, 217, 219] Consequently, photocatalytic reactions on plasmonic nanostructures may display a positive relationship between quantum efficiency and photon flux (semiconductors exhibit lower quantum efficiency at higher light intensity). Also, it has been recently observed that the rate and quantum efficiency of photocatalytic plasmonic reactions may increase with operating temperature (semiconductor photocatalysts exhibit lower reaction rates at higher temperatures). [203, 217, 219] This positive dependence of quantum efficiency and photocatalytic reaction rate on light intensity and operating temperature provides the possibility that, unlike semiconductor photocatalysts, plasmonic nanostructures may effectively couple thermal and photonic stimuli to drive chemical transformations.[5, 217, 219-222]

Two main enhancement mechanisms have been proposed for the observed activities in plasmonic photocatalysis: localized heating and charge transfer of LSPR-generated charge carriers at the metal-molecule interface *via* direct and indirect mechanisms.[223] Upon light LSPR excitation (**Fig. 6a**),[205] the LSPR oscillation decays *via* non-radiative and radiative pathways [197, 217, 224] While radiative damping involve scattering and is not so attractive for plasmonic photocatalysis, non-radiative damping (Landau damping) leads to the generation of hot electrons and hot holes (**Fig. 6b**). In other words, this creates the probability of finding the excited electrons between the fermi level of the nanoparticle (E_F) and $E_F + h\nu$.[223] Further decay *via* electron-electron and electron-phonon coupling lead to a Fermi-Dirac distribution of charge carriers (**Fig. 6c**), which also decays *via* thermal dissipation to the surroundings (**Fig. 6d**).[225, 226,217, 227,228,223] This localized heating can provide the energy input to accelerate chemical reactions. It has also been employed in several biomedical applications[229, 230] and the development of photothermal motors using self-assembled Au NPs. Under light incidence, these NPs are responsible for raising the local temperature, which thus generates water vapor that propels the material to the opposite side of the vapor current.[231 219, 232] Another important application included the utilization of aluminium (Al) NPs for the desalinization of water. A three-dimensional porous membrane containing Al NPs, fabricated by its self–assembly, was employed as a plasmonic heat source. Through water vapor generation, saline water was efficiently purified under solar light irradiation. These applications provide huge environmental impact at remote locations where pure water is scarce.[233]

Regarding the enhancement mechanism *via* charge transfer of LSPR excited hot carriers, two potential microscopic pathways, indirect and direct, can take place. In the indirect

pathway, charge carriers are excited from occupied states to higher-energy unoccupied states in the metal particle. This leads to an excited electron distribution. Charge carriers of appropriate energy from this distribution can then scatter through the adsorbate states (orbitals) forming transiently charged adsorbates. The facilitation/activation of these species then lead to increased reaction rates. The role of LSPR in this process is to increase the rates of charge excitation. On the other hand, the direct transfer pathway involves an LSPR-induced electron excitation from occupied to unoccupied orbitals of the molecule-nanoparticle complex that is not mediated by the formation of an excited electron distribution within the metal. Instead, there is the excitation of an electron directly into an unoccupied adsorbate orbital of matching energy.[234, 235]

As aforementioned, the LSPR excitation also leads to the generation of intense electric fields close to the surface of the nanostructure. These electric fields are fundamental for applications such as the Surface-enhanced Raman scattering (SERS) phenomenon according to the electromagnetic mechanism of enhancement (**Fig. 5d-e**).[236,237] In addition to its applications towards the development of ultrasensitive sensors, SERS can also be employed to monitor transformations triggered by the LSPR excitation. One example is the SPR-mediated oxidation of 4-aminothiophenol (PATP) to 4,4'-dimercaptoazobenzene (DMAB).[238] Moreover, some reports have shown that these electric fields may be related to plasmonic catalytic enhancements.

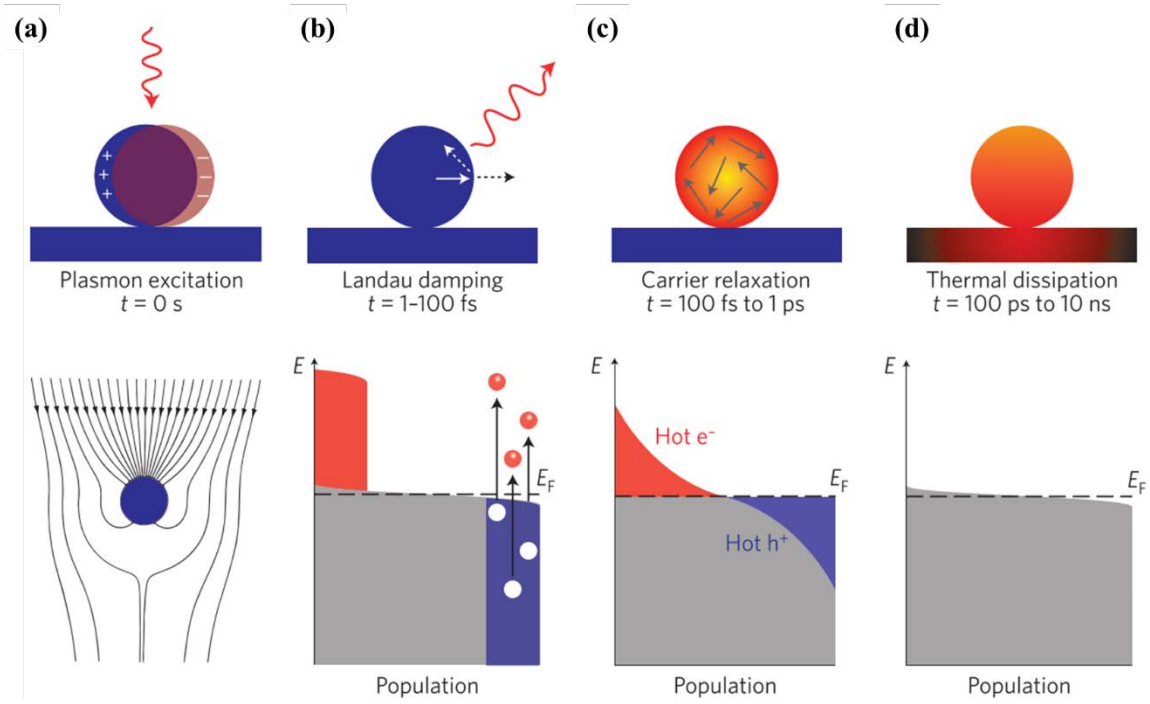

Figure 6. Photoexcitation and subsequent relaxation processes following the illumination of a metal nanoparticle with a laser pulse, and characteristic timescales; (a) First, the excitation of a localized surface plasmon redirects the flow of light (Poynting vector) towards and into the nanoparticle; (b-d) Schematic representations of the population of the electronic states (grey) following plasmon excitation: hot electrons are represented by the red areas above the Fermi energy E_F and hot hole distributions are represented by the blue area below E_F; (b) In the first 1-100 fs following Landau damping, the a thermal distribution of electron-hole pairs decays either through re-emission of photons or through carrier multiplication caused by electron-electron interactions. During this very short time interval, the hot carrier distribution is highly non-thermal; (c) The hot carriers will redistribute their energy by electron-electron scattering processes on a timescale ranging from 100 fs to 1 ps; (d) Finally, heat is transferred to the surroundings of the metallic structure on a longer timescale ranging from 100 ps to 10 ns, *via* thermal conduction. Reprinted with permission from ref [228]. Copyright 2015 Springer Nature.

Therefore, based on the remarkable optical properties of Ag, Au, and Cu NPs in the visible and near-infrared range as a result of the LSPR excitation, it becomes intuitive that their hybrids with g-C_3N_4 may lead to materials with interesting properties that combine plasmonic and photocatalytic effects. In the following sections, we will start by discussing some general aspects and principles involved in the construction of hybrid materials composed of plasmonic nanoparticles and semiconducting materials. Then, we will focus on the emerging class of hybrids composed of g-C_3N_4 and plasmonic nanoparticles.

5.2. Coupling plasmonic NPs and semiconducting materials

It is well known that plasmonic NPs can act as both light absorbers and electron traps, enabling the lowering recombination rates when combined with semiconducting materials. [239] When metal NPs are deposited on a semiconductor surface, a contact potential difference is generated at their interface due to their different work functions. This potential difference is called the Schottky barrier, and the band bending when a contact is formed after reaching equilibrium is dependent on the relative energies of the work functions of the metal and semiconducting component as illustrated in **Fig. 7**. This phenomenon can induce the directional migration of photogenerated electrons from semiconductor to metal, greatly enhancing the charge separation efficiency.[24] Therefore, this system behaves as an effective electron trapping site to suppress the electron-hole recombination.

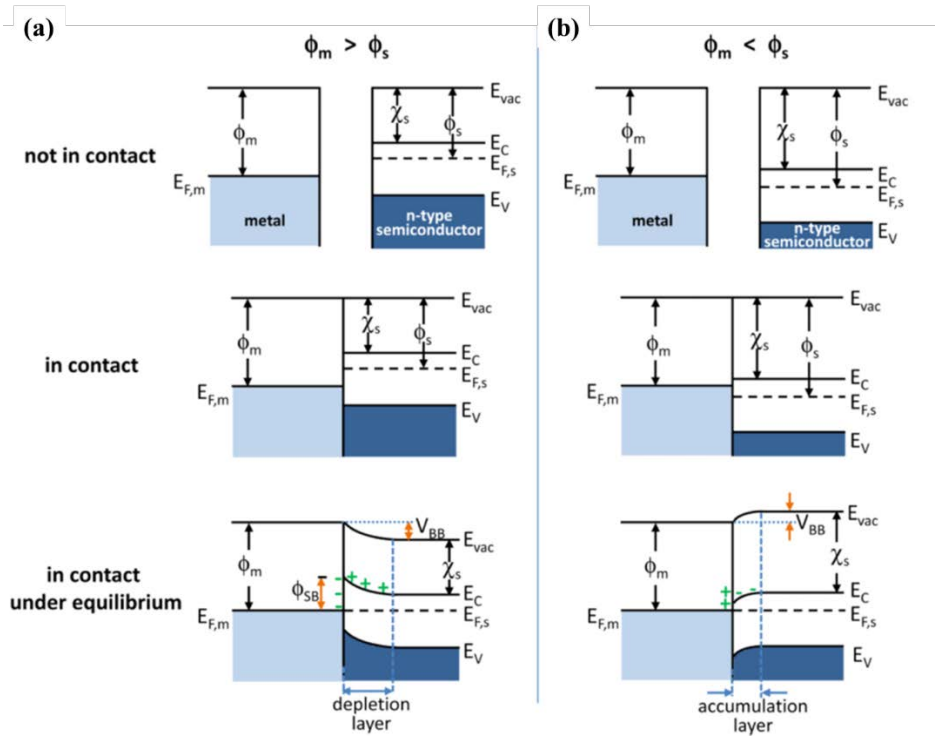

Figure 7. Band structures for a hybrid composed of a metal and a semiconductor nanoparticle (the not in contact, in contact, and in contact under equilibrium scenarios are shown in the top, middle and bottom panels, respectively.). (a) and (b) represent the band-bending effect on a metallic nanoparticle (light blue) attached to an n-type semiconductor (dark blue) in two scenarios: when the semiconductor work function (ϕ_s) is higher than the metal work function (ϕ_m) (a), and when the semiconductor work function (ϕ_s) is lower than the metal work function (ϕ_m) (b). Reprinted with permission from ref [240]. Copyright 2012 American Chemical Society.

Fig. 8 displays the common mechanisms by which the LSPR excitation in hybrids between plasmonic NPs and semiconductors hybrids can lead to improvements in photocatalytic activities.[223] When plasmonic NPs are coupled with semiconductors, in addition as acting as electron traps, localized heating (**Fig. 8a**) and near-field enhancements (**Fig. 8b**) as a result of the LSPR excitation can lead to an enhancement in the generation of charge carries at the semiconductor. Moreover, charge-transfer processes of SPR-excited hot electrons and holes between the metal and semiconductor can also take place (**Fig. 8c**). These processes also occur simultaneously in the hybrids. In this case, the elucidation of the mechanistic contribution of each effect over the detected activities represents an important challenge in the field.[238,196, 223, 241]

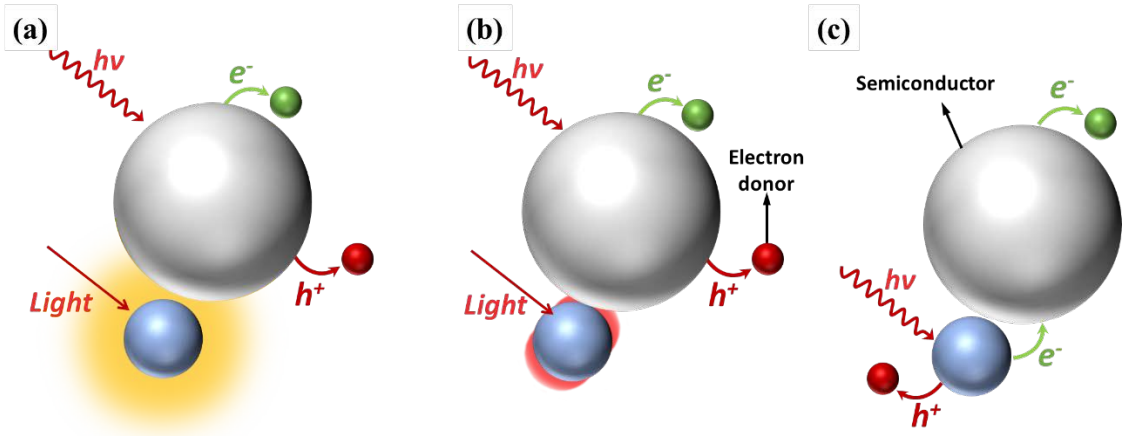

Figure 8. (a-c) LSPR-related mechanisms on hybrid materials composed of plasmonic NPs and semiconducting materials; (a) Local temperature increase causes the enhancement of exciton formation on the semiconductor; (b) Optical near-field enhancement promotes the transfer of photons to the semiconductor, thus increasing the exciton formation; (c) Hot-electrons and holes are transferred to the semiconductor, so reactions on their surface can also be enabled by LSPR. Reprinted with permission from ref [223]. Copyright 2014 Royal Society of Chemistry.

Three main approaches can be employed for the synthesis of these hybrids. The first consists in the heterogeneous nucleation and growth of metal NPs at the surface of the semiconductors, which are employed as seeds or physical templates for the formation of metal NPs. The second comprises the impregnation of pre-formed NPs at the surface of the semiconductor. Finally, the third involves the one-pot synthesis of both semiconductor and metal NPs.[242-250] It is important to note that metal/semiconductor NPs hybrids displaying core-shell and other morphologies have also been reported (such as metal NPs decorated at the tips of semiconducting nanorods). However, these systems will not be the focus of our discussion in this review.

Among the several reported materials, hybrids composed of Au NPs and TiO_2 represent one of the most widely studied examples of a material comprising a plasmonic and semiconducting component.[251-256] In the context of g-C_3N_4, it is clear that the LSPR excitation of noble (Au and Ag)[4] and even non-noble (e.g. Bi) metals can expand the optical spectral response of g-C_3N_4 to visible light, while the excellent catalytic activity enabled by the metal NPs can provide catalytic sites for target transformations.[28, 257-261]

5.3. Hybrids between noble metal NPs and g-C_3N_4

Au and Ag represent the most investigated noble metal NPs displaying LSPR effect in the visible or near-infrared range. Au-loaded on bulk[53, 262, 263] and exfoliated[264] g-C_3N_4 have been reported for various photocatalytic applications.[265] Different methods to decorate the g-C_3N_4 surface with the metal NPs are commonly used, such as photoreduction,[263, 264, 266] impregnation,[265] and deposition-precipitation.[53] Di *et al.* compared Au/g-C_3N_4 synthesized by photoreduction, impregnation, and deposition-precipitation. They reported a higher photocatalytic activity for the composite prepared by the deposition-precipitation, due to the formation of tight Au-semiconductor heterojunctions effectively promoting the transfer of charge from light-excited g-C_3N_4.[53] The stronger the interfacial contact between Au and g-C_3N_4, the easier the electron migration process will be. Moreover, the LSPR effect in Au helped in visible light absorption in the hybrid, also contributed to the superior photocatalytic activities. Samanta *et al.* compared pure g-C_3N_4 with 1 wt% Au/g-C_3N_4. The plasmonic photocatalyst presented a photocurrent density that was 3000 folds higher than pure g-C_3N_4. The dramatically enhanced photocurrent density of Au/g-C_3N_4 was ascribed to the strong visible light absorption and boosted charge carrier separation due to the LSPR effect from Au NPs.[54] Furthermore, it can be observed that the Au Fermi level can shift towards more negative potentials when the electrons were transferred from the sp^2-hybridized π-conjugated g-C_3N_4 network to Au. Essentially, Au played a dual-function role as an electron collector and also as a plasmonic cocatalyst.[28]

Ag, which presents a characteristic LSPR peak centered at ca. 450 nm, has also been employed to form heterojunctions with g-C_3N_4.[52, 267-272] It is important to note that in both Au and Ag, the LSPR frequency can be tuned by maneuvering their size and shape.[5] Yang *et al.* reported that Ag/g-C_3N_4 nanohybrids prepared by photo deposition were active under visible light due to the LSPR excitation in Ag NPs as well as the fast transportation and separation of charge carriers.[273] It was demonstrated that the LSPR effect of Ag promoted an enhancement of local electromagnetic fields, which improved the generation of electron and holes within g-C_3N_4. In addition to the LSPR effect, the photogenerated electrons on g-C_3N_4 can be scavenged promptly by Ag NPs, forming a Schottky barrier to inhibit the charge recombination process.[28] Further details about Ag modified g-C_3N_4 hybrid synthesis and their applications can be found in a recent review written by Patnaik *et al.*[274]

An interesting example that illustrated the importance of the strength of interaction between the noble metal and g-C_3N_4 to ensure the smooth transfer of photoinduced electrons

was reported in the Pt/g-C_3N_4 material by Shiraishi and co-workers. They investigated the influence of two different synthesis methods over photocatalytic activities: *i*) reduction of Pt precursor by H_2 at a high temperature, and *ii*) photoreduction. Both approaches yielded nearly similar Pt particle sizes (ca. 3.5−4 nm). Surprisingly, the catalyst prepared by the high-temperature method exhibited 10 times higher photocatalytic activity for H_2 evolution when compared with samples prepared by photoreduction method.[275] Several other studies also reported increased photocatalytic activity in Pt/g-C_3N_4 heterojunctions, especially for photodegradation[276] and CO_2 photoreduction.[277, 278]

In addition to Pt, Pd/g-C_3N_4 heterojunctions have been widely investigated. A range of publications have addressed synthesis routes to decorate g-C_3N_4 with Pd NPs.[279-284] Among them, it is worth to highlight the results reported by Bai and co-workers on the effect of Pd facet selectivity as a cocatalyst in photocatalysis. They produced uniformly dispersed Pd NPs with different preferential exposed facets, {100} and {111}, on 2D g-C_3N_4. They showed that reduction of CO_2 can better occur on Pd {111} facets while H_2O prefers to generate H_2 on Pd-{100}. The authors justified the higher activity of the Pd {111} facets towards CO_2 reduction as a result of the higher adsorption energy of CO_2 in these surface facets (0.230 eV) when compared to Pd {001} (0.064 eV), as indicated by first-principles theoretical calculations.[283]

5.4. Hybrids Between Non-Noble Metals NPs and g-C_3N_4

Apart from the noble metals, Bi, Ni and Cu have also been used to form hybrid composited with g-C_3N_4. The semimetal Bi exhibits intriguing properties, being able to act as an electron reservoir and possessing plasmonic properties (which are in essence similar to the noble metals). Dong *et al.* deposited Bi nanospheres on thin g-C_3N_4 layers and observed a wide additional absorption peak at ca. 500 nm, thus improving visible light absorption and thus the generation of charge carriers. They also observed a higher surface photovoltage (SPV) response for Bi/g-C_3N_4 due to the electric field generated from Bi accompanied by the transfer of electrons from g-C_3N_4 to Bi metal as an electron channel. These local electromagnetic fields emerge from the LSPR effect in Bi, which was confirmed by using a finite integration technique simulation.[285] Another non-noble metal displaying plasmonic properties which was reported in g-C_3N_4 based hybrids is Cu. To the best of our knowledge, only Zhang *et al.* have investigated Cu NPs to improve photocatalytic reactions in this context. They observed a red-shift on light absorption due to LSPR effect of Cu NPs and an

increment in the H_2 evolution rate under visible light irradiation.[286] Wang *et al.* have tested Cu/g-C_3N_4 NPs composite as peroxidase-like to help in glucose detection in blood samples, which allow lower detection limits.[287] Studies on Cu/g-C_3N_4 heterojunctions have remained scarce mainly due to the instability of the Cu NPs towards oxidation in air. Hence, most of the reports tested Cu oxides or hydroxides with g-C_3N_4.[171, 288, 289]

Ni has also been studied as a cocatalyst with g-C_3N_4. Bi *et al.* reported increment on the SPV due to efficient charge separation at the heterojunction interface of Ni/g-C_3N_4.[290] Kong and collaborators developed a robust and visible light active Ni/g-C_3N_4 catalyst for H_2 production. Their mechanistic studies concluded that the hybrid composite presented high visible light activity due to Ni NPs effectively preventing the recombination of the photogenerated electrons and holes of g-C_3N_4.[291] In a recent publication, Wen and co-workers reported that the H_2-evolution activity for the system Ni/g-C_3N_4 can be further improved by the addition of NiS. They reported a significant synergistic effect between the multifunctional metallic Ni interface layers and amorphous NiS improving the charge separation/transportation. This effect could enhance both H_2-production and TEOA-oxidation kinetics, thus resulting in the significantly boosted photocatalytic H_2 evolution over the ternary composite photocatalysts.[292] It is worth to highlight the recent Al decorated g-C_3N_4 reported by Choi and colleagues. The incorporation of this inexpensive and abundant metal significantly changed optical and photocatalytic properties and led to increments for H_2-evolution and organic pollutant degradation under light excitation.[293]

5.5. Hybrids between bimetallic NPs and g-C_3N_4

Compared to monometallic NPs, bimetallic NPs have attracted massive interest in catalysis, in which the synergy between the two metals (electronic effect) have led to improved performances.[24,294] In addition to catalytic activity, selectivity and stability have also been dramatically affected in the bimetallic systems.[295] Han *et al.* reported g-C_3N_4 nanohybrids modified with PtCo bimetallic alloy NPs. They were formed on g-C_3N_4 by an *in situ* strategy based on chemical reduction. This material was investigated towards the photocatalytic H_2 evolution. They showed that the bimetallic NPs increased the surface defect density and changed the Fermi level in comparison to monometallic Pt NPs. This lead to the better separation of photogenerated charge carriers and consequently to a more active catalyst for generate H_2 under visible light irradiation.[296] The same group also reported AuPd/g-C_3N_4 bimetallic photocatalysts with enhancement of visible light absorption and more efficient

separation of electron-hole pairs as compared to g-C_3N_4 and their monometallic counterparts.[297]

The effect of the exposed facet (shape effect) is also important in bimetallic systems. PtCu concave nanocubes displaying high-index {730} surface facets loaded on g-C_3N_4 nanosheets exhibited higher photocatalytic activity and selectivity in CO_2 reduction for methane (CH_4) production as compared to PtCu nanocubes (enclosed by {100} facets) loaded on g-C_3N_4. This enhancement was assigned to the presence of more low-coordinated, active metal active sites in the concave nanocubes with high index surface facets, favouring adsorption and activation of CO_2.[298]

5.6. Metal NPs in g-C_3N_4-based Z-scheme photocatalysts

An important class of application of metal NPs is to work as a conductor in Z-scheme photocatalytic systems. Metal NPs (such as Au, Ag, Pt, Cu, and Bi), as well as carbon materials (such as GO, CNTs, rGO and carbon), can be applied as solid-state electron mediators for the g-C_3N_4-based Z-scheme systems. They can promote a fast separation of the photogenerated electron-hole pairs at the interface of the two semiconductors.[299-302] The metal NPs can also serve as a charge transmission bridge. When a conductor is added between two semiconductors, it forms an Ohmic contact with low contact resistance as depicted in **Fig. 9**.[303, 304] The photoinduced electrons in the conduction band semiconductor 2 can directly recombine with the holes in the valence band of semiconductor 1 through the Ohmic contact. Consequently, the holes and electrons with more efficient redox ability can be mostly reserved for efficient photocatalytic reactions.[305, 306] Z-scheme systems have attracted considerable attention because it not only boosts the spatial separation efficiency of photoinduced electron-hole pairs but also minimizes undesirable backward reaction of the photocatalytic process due to two different redox sites.[307, 308] Moreover, maximum overpotentials can be obtained with this unique Z-scheme system, which benefits from the effective utilization of a high conduction band from semiconductor S2 and a low valence band from semiconductor S1.[309, 310] Many recent advances have been done using g-C_3N_4 in Z-scheme heterojunctions. This topic was recently reviewed by Jiang *et al.*, which covered the preparation and catalytic application of g-C_3N_4-based Z-scheme systems.[305]

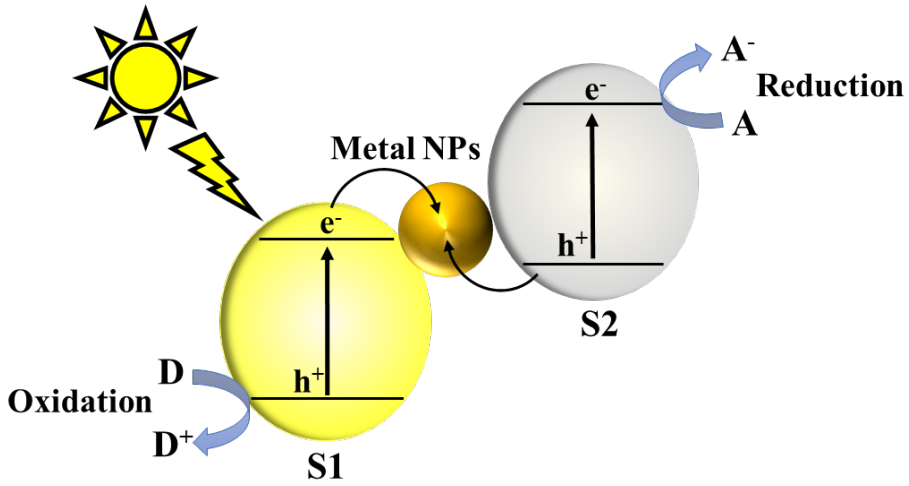

Figure 9. Schematic illustrations of two semiconductors (S1 and S2), coupled in a Z-scheme in the presence of a metal NPs as an electron mediator. Adapted with permission from ref [306]. Copyright 2015 John Wiley and Sons.

6. Photocatalytic Applications of Metal NPs and g-C_3N_4 Hybrids

Metal NPs can have a wide range of catalytic applications. In fact, they can be coupled with g-C_3N_4 to accomplish one or more of the following tasks: *i*) improve charge separation through heterojunctions with g-C_3N_4; *ii*) improve the visible light utilization; and *iii*) act as a cocatalysts lowering the redox overpotential at the active sites and helping in the activation of the reactant molecules.[28] This section will focus on how each metal presented in the last section help to address one or more of those tasks when coupled with g-C_3N_4 in different catalytic reactions together with a detailed discussion of their enhancement mechanisms.

6.1 Photocatalytic Water Splitting

Hydrogen is considered as an ultimate clean fuel because of its high-energy density (140 MJ kg^{-1}), environmental benignancy, and recycling.[1, 117, 311] The generation of H_2 from water by employing a photocatalyst and solar energy has been considered a promising approach to produce hydrogen energy.[312, 313] A range of semiconductor photocatalysts have been reported to catalyse the evolution of H_2 from water. However, the practical applications of this strategy are limited by the prompt recombination of photogenerated electron-hole pairs within photocatalysts. According to the requirement of thermodynamics, the conduction band potential should be more negative than the reduction potential of H_2O (0 V vs. NHE) for H_2

generation, and the valence band potential should be more positive than the oxidation potential of H_2O (1.23 V vs. NHE) for O_2 generation. g-C_3N_4 possess appropriate conduction and valence band positions to catalyse the water splitting reaction.[24, 314] Moreover, its visible-light-driven properties and high specific surface area makes g-C_3N_4 a promising photocatalyst to promote the H_2-evolution from water.[314, 315] The U.S. Department of Energy (DOE) has concluded that photocatalyst for water splitting must have solar-to-hydrogen (STH) efficiency equal or higher than 5% to meet the economically viable price of US$ 2-4 /kg H_2. Up to now, one of the photocatalysts that are closer to this efficiency is a g-C_3N_4-based catalyst comprised of carbon nanodots on g-C_3N_4.[128] Despite all the great properties of the g-C_3N_4, when it is used to catalyse the water-splitting reaction, it produces 0.1−4 μmol h^{-1} of H_2 with a quantum efficiency (QE) of less than 1% under visible light.[28, 261, 316, 317] Hence, it is highly important modify g-C_3N_4 to allow higher rates of H_2 production and quantum efficiencies. For instance, **Table 1** summarizes the recent advances in the photocatalytic water splitting photocatalysed by metal NPs/g-C_3N_4-based nanohybrids.

Platinum is one of the most efficient cocatalysts for H_2 generation and has been widely used for enhancing the performance of g-C_3N_4-based hybrid.[13, 260, 261, 275-278, 318-322] The intriguing mechanism of how the noble metals, especially Pt, act during the water-splitting reaction has been widely investigated. Fina *et al.* found that the oxygen content of the cocatalyst does not seem to affect the photocatalysts activity. Their investigation concluded that the main factor affecting the H_2 evolution rate of the materials was the coverage, represented as the Pt:N ratio, with a lower coverage being more beneficial. Following the coverage, the crystallite size of the metal NPs also played an important role in the catalytic activity. Pt/g-C_3N_4 materials in which Pt NPs were characterised by a higher crystallinity resulted in a higher H_2 evolution.[260] Li and co-workers investigated single-atom Pt as a cocatalyst for g-C_3N_4 in H_2 production. They showed that isolated single Pt atoms induces an intrinsic change of the surface trap states leading to a longer lifetime of photogenerated electrons and thereby improved photocatalytic performance (**Fig. 10**). Single-atom Pt cocatalyst led to tremendous enhancements on photocatalytic H_2 generation, being 8.6 times higher than that of Pt NPs the per Pt atom basis, and nearly 50 times of that for bare g-C_3N_4.[318]

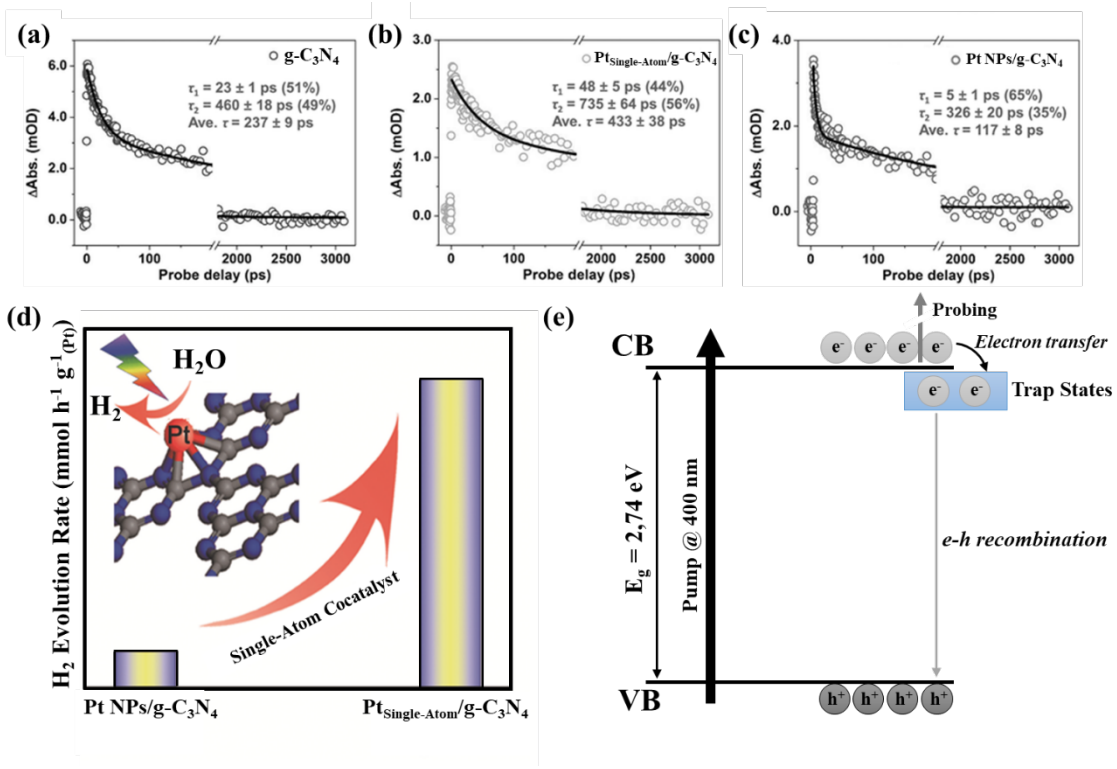

Figure 10. Representative ultrafast transient absorption (TA) kinetics probed at 750 nm (pump at 400 nm) for (a) g-C_3N_4; (b) $Pt_{Single\text{-}Atom}$/g-C_3N_4 and (c) Pt NPs/g-C_3N_4. (d) Schematic model of $Pt_{Single\text{-}Atom}$/g-C_3N_4 and photocatalytic comparison with Pt NPs/g-C_3N_4; (d) Schematic illustration of the mechanisms which led to a longer lifetime of photogenerated electrons. Adapted with permission from ref [318]. Copyright 2016 John Wiley and Sons.

Although Pt is essentially the most efficient cocatalyst for water splitting, it is prohibitively expensive, which strongly limits its practical applications. In the past few years, the Pt-free approach has been successfully demonstrated for H_2 evolution by combining g-C_3N_4 with a more inexpensive metal, such as Ni, Cu, Zn, Co, and Fe. Chen *et al.* introduced single Ni active sites onto the surface of g-C_3N_4 by using a molecular-level design strategy.[323] The resulting catalyst family (with less than 0.1 wt% of Ni) was shown to generate H_2 with a rate close to that attained with a 3 wt% Pt on g-C_3N_4. In another contribution, Bi *et al.* synthesized a series of Ni-doped g-C_3N_4 and demonstrated a surface band bending change of g-C_3N_4 when contacted with Ni. The results indicated that Ni-coating deepened the surface band bending of g-C_3N_4, thereby resulting in higher separation efficiency of photoinduced electron-hole pairs and improved H_2 generation activity.[290] Indra and collaborators proved that Ni^{2+} mesoporous g-C_3N_4 can be reduced to Ni^0 NPs during the photocatalytic reaction in the presence of sacrificial agent (e.g., TEOA), and act as a cocatalyst to reduce protons to

H_2.[324] Zhang *et al.* deposited cobalt on g-C_3N_4 by using a homogeneously engineered strategy *via* chemical interaction. This modification promoted the surface kinetics of oxygen evolution reaction increasing its activity by two when compared with pure g-C_3N_4.[325]

Zhang *et al.* added the noble metal rhodium (Rh) as the cocatalyst on g-C_3N_4 and investigated the influence of Rh NP size on the photocatalytic activity for H_2 evolution. The authors demonstrated that the light-absorption properties of the g-C_3N_4 were not influenced by the presence of Rh and its activity is not significantly affected by the NPs size. However, the number of Rh NPs on the surface of g-C_3N_4 and the metallic nature of Rh^0 greatly influenced the photocatalytic H_2 production activity of g-C_3N_4.[259]

Another metal which has shown promising results when coupled with g-C_3N_4 is Ag. Sridharan and co-workers compared the activity Ag NPs and Ag quantum clusters (Ag \QC) on g-C_3N_4 towards the H_2 evolution reaction. The authors reported an enhanced absorbance for the AgQC/g-C_3N_4 originating from quantum confinement effect. Despite the fact that this improvement confers an activity 1.7 times higher than g-C_3N_4 for H_2 production, the AgQC/g-C_3N_4 still was slightly less active than AgNP/g-C_3N_4, because of surface hydroxyl radical formation on the AgQC/g-C_3N_4 surface.[326] Qin and Zeng reported improved activity using Ag NPs combined with carbon quantum dots (CQDs) and g-C_3N_4. The authors demonstrated a synergistic effect due to the combination of LSPR effect from Ag NPs with upconverted PL superiority of CQDs allowing a broader spectrum application (**Fig. 11a**), which lead to photocatalytic activities for H_2 evolution 6.7 times higher than pure g-C_3N_4 and 2.8 higher than CQDs/g-C_3N_4.[327] The same research group also reported the improvement in photocatalytic H_2 generation of Ag/g-C_3N_4 nanohybrids, under visible-light illumination, through dye-sensitization with fluorescein.[328] The addition of the photosensitizer fluorescein lead to an activity for H_2 production 4.8 times higher than that of 3 wt% Ag/g-C_3N_4 in the absence of dye molecules, which was approximately 4.8 times higher than that of 3 wt% Ag/g-C_3N_4 in the absence of dye molecules. The LUMO orbital of fluorescein is more negative than the conduction band of g-C_3N_4, while its HOMO is more positive than the redox potential of the sacrificial reagent, TEOA.[28, 328] Upon the irradiation of visible light, both fluorescein and g-C_3N_4 were excited, and the electrons from fluorescein can easily migrate to the conduction band of g-C_3N_4. Subsequently, the electrons rapidly migrated to the Ag, accumulating onto Ag NPs to create a Schottky barrier, which could hinder the recombination of electron-hole pairs. The strong local electromagnetic field induced by the LSPR effect of Ag could also improve the captured electron energy and transfer rate, allowing them to react with H^+ increasing the H_2 production (**Fig. 11b**). Simultaneously, the

photogenerated holes of fluorescein and g-C_3N_4 could be packed by electrons from TEOA for reuse.[28, 328]

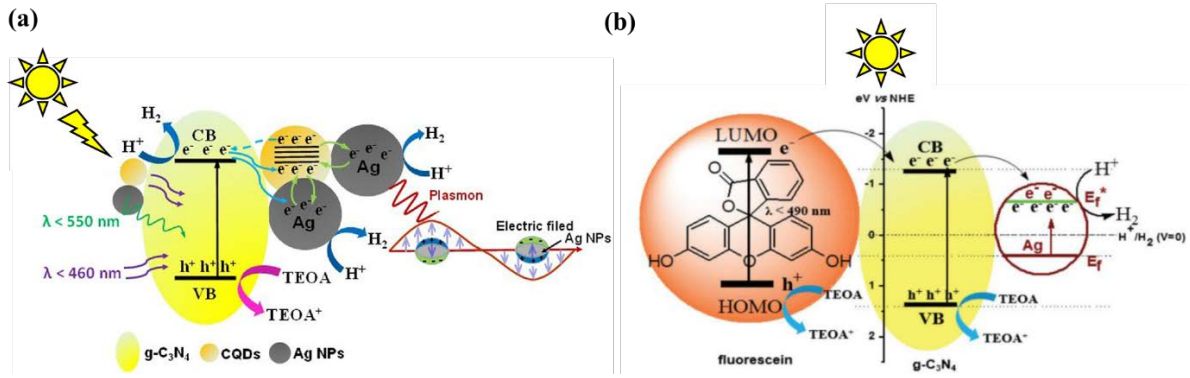

Figure 11. (a) Scheme showing the charge generation, transfer process, and photocatalytic H_2 evolution mechanism over the Ag/CQDs/g-C_3N_4 hybrids. Reproduced with permission from ref [327]. Copyright 2017 Elsevier; (b) Schematic representation of the charge migration and separation improvement promoted by fluorescein on Ag/g-C_3N_4 hybrids. Reproduced with permission from ref [328]. Copyright 2015 Royal Society of Chemistry.

The promotion mechanism in Ag-modified g-C_3N_4 photocatalysts was investigated for the first time by Bu and collaborators through an electrochemical method.[268] The decoration of the g-C_3N_4 surface with Ag NPs improved the conductivity and reduced the energy barrier of the interface reactions. As displayed in **Fig. 12**, both Fermi levels of g-C_3N_4 and Ag are shifted positively when Ag is in contact with the g-C_3N_4 surface because the conduction band potential of g-C_3N_4 is less positive than the Fermi level of Ag. Therefore, when the Fermi level of g-C_3N_4, which is situated below the conduction band, is shifted to the positive direction. The conduction band of g-C_3N_4 is simultaneously moved in the same direction. Consequently, the conduction band generates an upward band bending near to the interface between Ag and g-C_3N_4 for the transfer of photoexcited electrons from g-C_3N_4 to Ag NPs. This phenomenon leads to the formation of an interfacial electric field. When the electron exchange is held in equilibrium, the flat band potential (E_{fb}) is positively shifted. This enhances the separation efficiency and prolongs the lifetime of electron-hole pairs, accredited to the heterojunction electric field formed on the interface of Ag and g-C_3N_4.

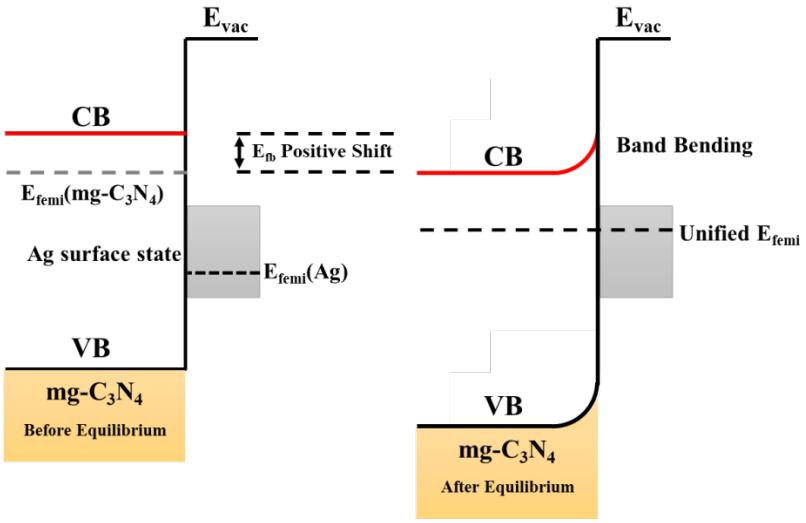

Figure 12. Schematic illustration of the electron energy level when Ag NPs are in contact with g-C_3N_4. Adapted with permission from ref [268]. Copyright 2014 Elsevier.

In fact, when the LSPR absorption of the noble metal partly coincides with the optical absorption of the photocatalyst, the LSPR induces plasmon resonance energy transfer (PRET) from the plasmonic metal to the adjacent semiconductor will excite charge carriers at the interface of noble metal/semiconductor.[329, 330] Thus, the PRET effect facilitates the generation of charge carriers and, for this reason, it suppresses the charge recombination by reducing the migration distance for the surface catalysis.[5] It is noted that the LSPR-induced electric field and the PRET effect will become greater when the distance between the semiconductor and the noble metal is optimised.[220] For the system Ag/TiO_2, this optimal distance corresponds to around 5 nm as reported by Linic *et al.*[5] If the semiconductor is located too near the noble metals, the nonradiative energy transfer, Förster resonance energy transfer (FRET), will primarily occur thus quenching the photoexcited semiconductor.[331] As a result, the distance between a semi-conductor and a noble metal is essential to balance the PRET and FRET effects. Chen and collaborators using an approach similar to that reported by Linic's group investigated the distance-dependent plasmonic influence in the system g-C_3N_4 and Ag NPs. They used a nanogap-engineering approach by loading the Ag@SiO_2 plasmonic core-shell NPs onto the g-C_3N_4 nanosheets.[269] In view of the distance-dependent plasmonic influence, the nanogaps between g-C_3N_4 and Ag NPs were tuned from 8 to 21 nm by modulating the SiO_2 shell thickness (**Fig. 13a-f**) in order to balance both PRET and FRET effects. The electromagnetic field intensity induced by Ag NPs could be viewed from the finite difference time domain (FDTD) simulation, as shown in **Fig. 13g-l**. By this the nanogap engineering approach, the optimum activity for the H_2 production reported by the authors was for the

system with a nanogap of 12 nm. This optimum distance balanced the positive PRET and the negative FRET effects on plasmonic photocatalysis (**Fig. 13m**).[269] This interesting finding will be particularly helpful to designing more effective metal NPs/g-C_3N_4 systems for photocatalytic applications.[28]

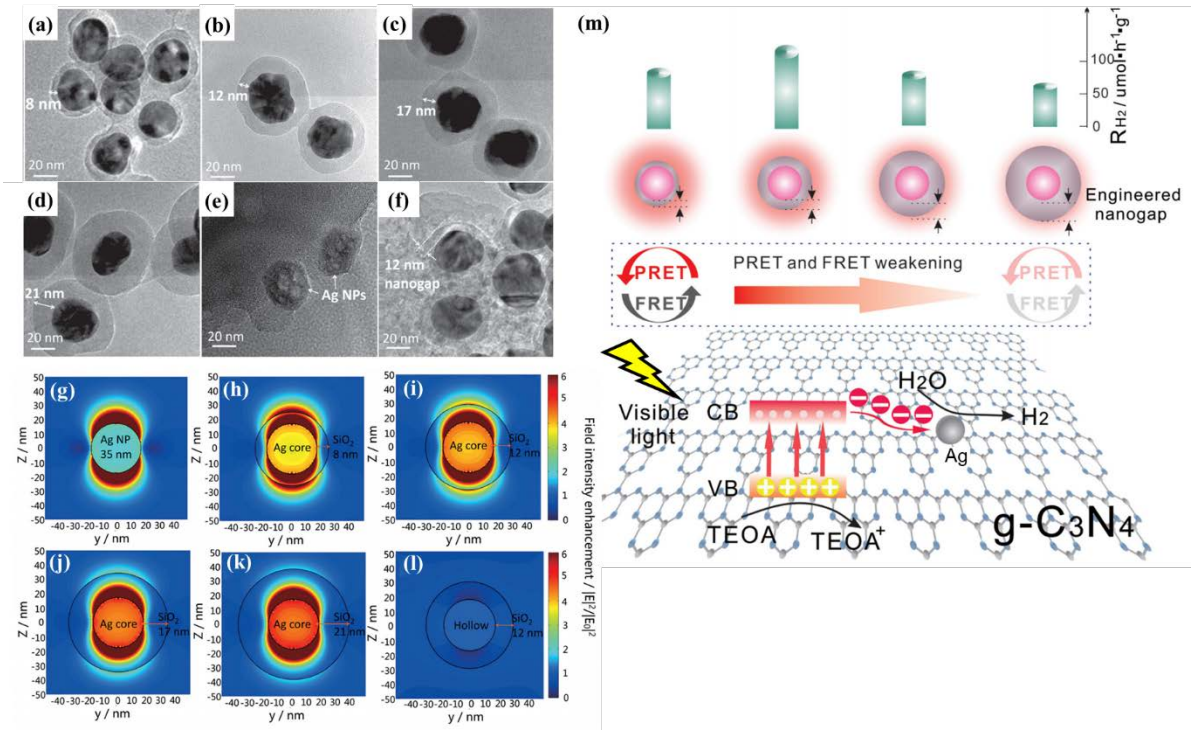

Figure 13. (a-d) TEM images of Ag@SiO_2 core-shell NPs in which the SiO_2 shell thickness corresponding to 8 (a), 12 (b), 17 (c), and 21 nm (d). (e) TEM image of Ag NPs without the silica coating. (f) TEM image for Ag/g-C_3N_4 without SiO_2 capping.; (g-l) FDTD simulation for the field enhancements for Ag NPs (g), Ag@SiO_2-8 nm (h), Ag@SiO_2-12 nm (i), Ag@SiO_2-17 nm (j), Ag@SiO_2-21 nm (k), and a hollow SiO_2 sphere with 12 nm shell thickness (l). (m) Representation of the mechanism for H_2 production over Ag@SiO_2/g-C_3N_4 in which the PRET and FRET effects gradually become weakened with the widening of the nanogap, as well as the H_2 evolution rate for each system. Reprinted with permission from ref [269]. Copyright 2015 John Wiley and Sons.

Regarding Au NPs, their combination with g-C_3N_4 presented higher activity for H_2 evolution than Pt/g-C_3N_4, as reported by Di *et al.*[53] They proposed that the Au NPs on the surface of g-C_3N_4 trapped and stored the photogenerated electrons from the substrate. This shifted the Fermi level to more negative values, promoting the transfer, with low resistance, of electrons from the conduction band of g-C_3N_4 to Au. Despite the good activity presented by the Au NPs, the Au/g-C_3N_4 photocatalytic system can have its activity further improved

by combining it with other metals to generate bimetallic compositions as shown in **Fig. 14**.[53] Other bimetallic cocatalysts, such as PtCo,[296] PdAg,[332] AuPd[297, 333] and AuPtO,[334] also have exhibited higher H_2 photocatalytic activity than their monometallic counterparts.

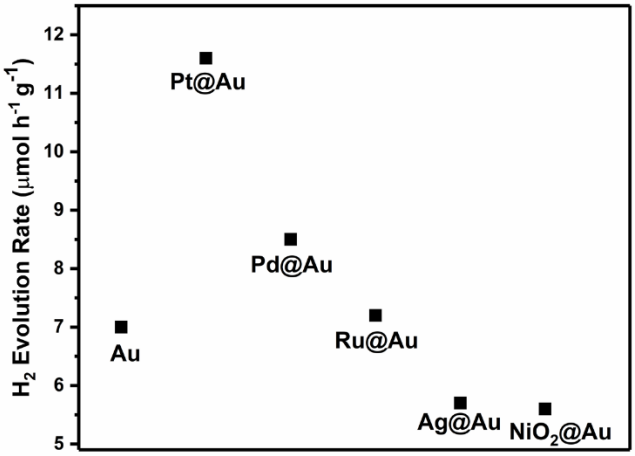

Figure 14. H_2 evolution over various bimetallic cocatalysts loaded on g-C_3N_4 under visible-light irradiation. Reproduced with permission from ref 53. Copyright 2010 John Wiley and Sons.

Metal NPs can have an important role in Z-scheme systems as explained in Section 5.6 and some of those properties can be exploited to enhance the photocatalytic activity for the water-splitting reaction. For example, when sulphur-doped g-C_3N_4/CdS is decorated with Au NPs, it becomes almost 2 times more active for H_2 evolution and 20 times more active than only sulphur-doped g-C_3N_4 under visible light irradiation. The Au NPs in this Z-scheme system act as an intermediate agent between sulphur-doped g-C_3N_4 and CdS, promoting the efficient transfer of excited electrons.[302] Ding *et al.* reported excellent results using a similar system comprised of an Au-core and CdS-shell (Au@CdS) NPs supported over g-C_3N_4. The author evaluated this Z-scheme photocatalyst for H_2 evolution under visible-light irradiation ($\lambda > 420$ nm) using methanol as a sacrificial reagent and observed that its activity was about 125.8 times higher than g-C_3N_4 (and was even higher than that of Pt/g-C_3N_4).[335] Au NPs were also successfully used in other Z-scheme systems to improve its activity in water splitting reaction, such as g-C_3N_4/Au/CdZnS[336] and $Cd_xZn_{1-x}S$/Au/g-C_3N_4.[337]

Another interesting result for improved water splitting was reported by Yin and co-workers using core-shell nanocubes composed of a Pd-core and Cu_2O-shell (Pd@Cu_2O), as shown in **Fig. 15**. The embedded Pd nanocubes not only promote the electron-hole separation by trapping the charge carriers from the semiconductors, but also act as a Z-scheme "bridge" in keeping the strong redox ability of the electrons/holes for surface reactions (as depicted in

Fig. 15h). The authors observed a H_2 evolution activity dramatically higher than that of its counterpart g-C_3N_4/Cu_2O structure without Pd.[338]

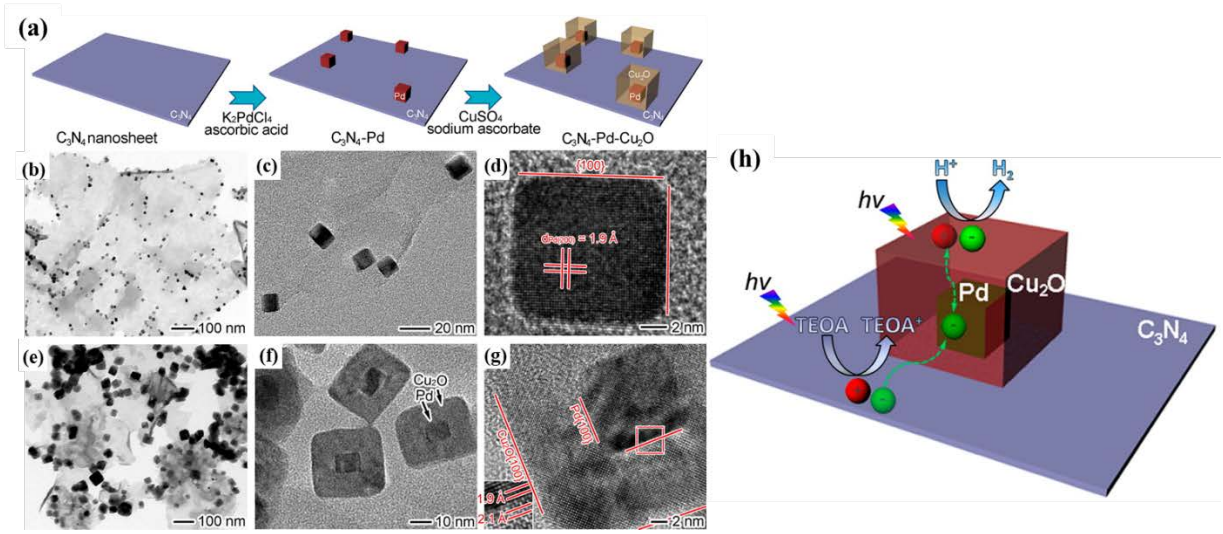

Figure 15. (a) Scheme of the synthesis of the Pd@Cu_2O/g-C_3N_4 hybrids. (b-g) TEM and HRTEM images of Pd/g-C_3N_4 (b-d) and Pd@Cu_2O/g-C_3N_4 hybrids (e-g). (h) Representation of the photocatalytic mechanism of H_2 evolution on the Pd@Cu_2O/g-C_3N_4 hybrids. Reproduced with permission from ref [338]. Copyright 2016 American Chemical Society.

Other Z-scheme system that deserves attention is the g-C_3N_4/Ag/MoS_2 ternary plasmonic photocatalyst. This material displayed a flower-like architecture of about 0.4-0.6 μm in diameter (**Fig. 16**). It was successfully synthesized by Lu and collaborators.[339] The authors reported that g-C_3N_4/Ag/MoS_2 was 8.78 and 2.08 times more active in the production of H_2 out of water than Ag/MoS_2 and g-C_3N_4/MoS_2, respectively. The excellent photocatalytic activities were attributed to the synergistic effects of Ag, g-C_3N_4, and MoS_2 nanostructures in the g-C_3N_4/Ag/MoS_2 composites, which result in a Z-scheme-mechanism-assisted fast separation and slow recombination of photoinduced electron-hole pairs and consequently higher photocatalytic activity.[339]

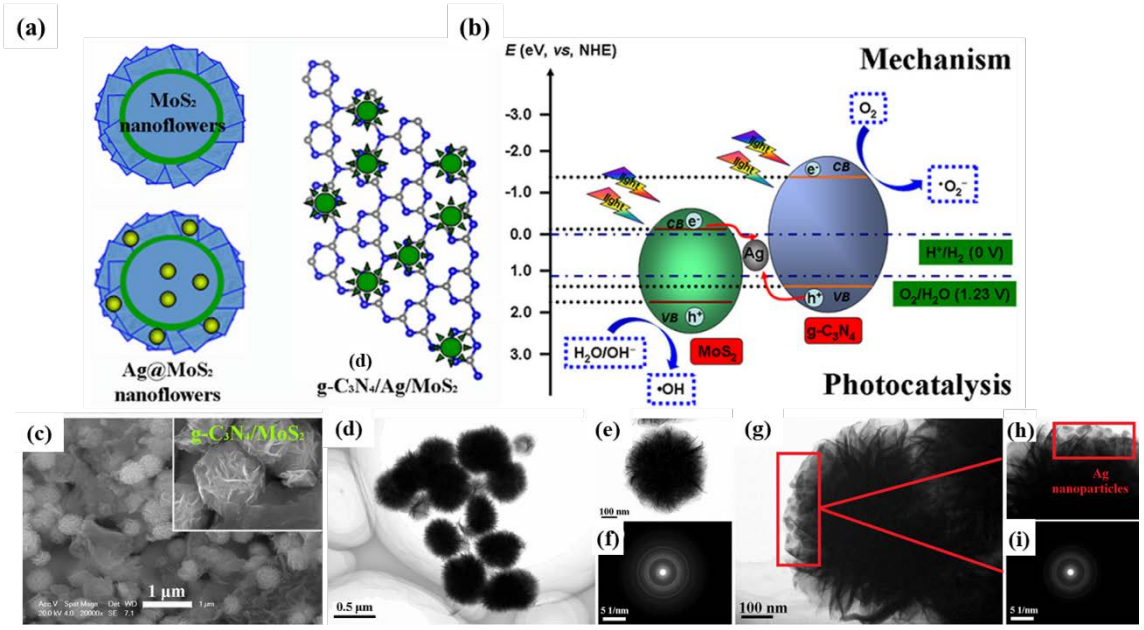

Figure 16. (a) Schematic illustration of hybrids composed of Ag/MoS_2 nanoflowers on g-C_3N_4; (b) Separation and transfer of photogenerated charges in the Ag/MoS_2/g-C_3N_4 nanohybrids; (c) SEM image of MoS_2/g-C_3N_4; (d-f) TEM images and SAED pattern for MoS_2; (g-i) TEM images and SAED pattern of Ag/MoS_2. Reproduced with permission from ref [339]. Copyright 2017 American Chemical Society.

A comparison of the photocatalytic activity towards the water-splitting reaction of all the systems discussed in this section is shown in **Table 1**.

Table 1. Photocatalytic H_2 evolution on metal NPs/g-C_3N_4 heterostructures

Catalysts	Fraction of cocatalysts	Total mass of catalysts	Reactant solution	Light source (wavelength-nm)	Activity (μmol h^{-1})	QE (%)	Ref.
g-C_3N_4	-	0.1 g	100 mL of 10 vol% TEOA and methanol aqueous solution	300 W Xe lamp (>420 nm)	0.1-4	<0.1%	[13]
CDots/ g-C_3N_4	0.016 wt%	0.080 g	150 mL of water	300 W Xe lamp (>420 nm)	8.4	6.29% (420 nm)	[128]
Pt/g-C_3N_4	1.13 wt%	0.080 g	100 mL of water	300 W Xe lamp (>400 nm)	0.531	N/A	[261]
Au/g-C_3N_4	1.0 wt%	0.1 g	100 mL of 10 vol% TEOA aqueous solution	500WHBO lamp (> 420 nm)	8.6	N/A	[53]
CdS/Au/g-C_3N_4	2.0 wt%	0.1 g	50 mL of 25 vol% methanol aqueous solution;	300 W Xe lamp (>420 nm)	19.0	N/A	[335]
$Pt_{Single-Atom}$/g-C_3N_4	0.16 wt%	0.05 g	100 mL of 10 vol% TEOA aqueous solution;	300 W Xe lamp (>420 nm)	318	N/A	[318]

$PtCo/g-C_3N_4$	1.0 wt%	0.05 g	100 mL of 10 vol% TEOA aqueous solution;	300 W Xe lamp (>400 nm)	48	N/A	[296]
$PdAu/g-C_3N_4$	0.5 wt%	0.05 g	100 mL of 10 vol% TEOA aqueous solution;	300 W Xe lamp (>400 nm)	16.3	N/A	[297]
$PdAg/g-C_3N_4$	1.0 wt%	0.01 g	22.5 mL of 10 vol% TEOA aqueous solution;	Solar Irradiation (840 W m^{-2})	1250	8.7%	[332]
$PtOAu/g-C_3N_4$	1.0 wt%	0.05 g	80 mL of 25 vol% methanol aqueous solution;	350 W Xe lamp (>400 nm)	16.9	N/A	[334]
$Rh/g-C_3N_4$	0.25 wt%	0.1 g	36 mL of 11 vol% methanol aqueous solution;	Xe Arc Lamp (320 mW/cm^2)	14.9	N/A	[259]
$Ni/g-C_3N_4$	10 wt%	0.05 g	100 mL of 10 vol% TEOA aqueous solution	500 W Xe lamp	15.66	0.4% (365 nm)	[340]
$Ni/g-C_3N_4$	10 wt%	0.05 g	100 mL of 10 vol% TEOA aqueous solution	500 W Xe lamp	8.41	N/A	[290]
$Ni_{(Single\ site)}/g-C_3N_4$	0.1 wt%	0.05 g	50 mL of 10 vol% TEOA aqueous solution	Xe lamp (125 mW/cm^2); (>420 nm)	5.5	2.6% (420 nm)	[323]
$NiS/Ni/g-C_3N_4$	0.5 wt%	0.05 g	100 mL of 15 vol% TEOA aqueous solution	300 W Xe lamp (160 mW/cm^2); (>420 nm)	515	N/A	[292]
$Ag/g-C_3N_4$	~8%	0.01 g	40 mL of 25 vol% methanol aqueous solution;	Solar simulator	2.8	N/A	[326]
$AgQC/g-C_3N_4$	7.46 wt%	0.01 g	40 mL of 25 vol% methanol aqueous solution;	Solar simulator	2.43	N/A	[326]
$Ag/CQDs/g-C_3N_4$	3 wt%	0.005 g	70 mL of 14 vol% TEOA aqueous solution;	300 W Xe lamp	626.93	4.81% (400 nm)	[327]
Fluorescein/$Ag/g-C_3N_4$	2.95 wt%	0.005 g	70 mL of 10 vol% TEOA aqueous solution;	300 W Xe lamp	2014.20	N/A	[328]
$CdZnS/Au/g-C_3N_4$	-	0.1 g	100 mL of 0.25 M Na_2S and 0.35 M Na_2SO_3 aqueous solution;	300 W Xe lamp (>420 nm)	6150	N/A	[336]
$Cd_{0.8}Zn_{0.2}S/Au/g-C_3N_4$	2.0 wt%	0.05 g	70 mL of 0.1 M glucose aqueous solution;	300 W Xe lamp (>420 nm)	123	N/A	[337]
$g-C_3N_4/Pd/Cu_2O$	-	0.015 g	20 mL of 10 vol% TEOA aqueous solution;	300 W Xe lamp (100 mW cm^{-2}); (>400 nm)	32.5	0.9% (420 nm)	[338]
$g-C_3N_4/Ag/MoS_2$	2.0 wt%	0.10 g	20 mL of 10 vol%	300 W Xe lamp	10.4	N/A	[339]

	TEOA aqueous solution;	(172 mW cm^{-2}); (>420 nm)

6.2 Photocatalytic Reduction of CO_2

Over the past century, our society has become heavily dependent on fossil fuel sources such as coal, gas, and oil to produce our daily energy needs and chemicals.[341] The carbon dioxide produced by these non-renewable carbon sources has been significantly altering the climate on Earth[342] and our heavy reliance make them more expensive and less abundant.[341] A larger demand on fossil resources for the next few decades is expected since the global economy will continue to grow steadily.[343] Recently, a great effort towards reducing the regional and global CO_2 emissions has been pursued. However, a breakthrough technology which allows converting CO_2 into energy-bearing products is required. Inspired by the natural photosynthesis, the photocatalytic conversion of CO_2 into energy-bearing products has been regarded as an alternative option to address the diminishing of fossil resources and mitigate the greenhouse gas effect to attain solar energy conversion.[344, 345] In this artificial photosynthesis approach, a photocatalyst directly captures CO_2 and solar energy and converts them into hydrocarbon fuels. The photocatalytic CO_2 reduction process is a multielectron transfer process. The possible reaction processes and corresponding redox potentials (vs. reversible hydrogen electrode, RHE) are shown below:

(1)	$CO_2 + 2H^+ + 2e^- \rightarrow HCOOH$	(E_{redox}= -0.20V)
(2)	$CO_2 + 2H^+ + 2e^- \rightarrow CO + H_2O$	(E_{redox}= -0.12V)
(3)	$CO_2 + 4H^+ + 4e^- \rightarrow HCHO + H_2O$	(E_{redox}= -0.07V)
(4)	$CO_2 + 6H^+ + 6e^- \rightarrow CH_3OH + H_2O$	(E_{redox}= +0.03V)
(5)	$CO_2 + 8H^+ + 8e^- \rightarrow CH_4 + 2H_2O$	(E_{redox}= +0.17V)

The CO_2 reduction reactions are complex with many pathways and products. Moreover, the CO_2 molecule is extremely difficult to be activated and further reduced at room temperature due to its thermodynamic stability. These factors make photocatalytic CO_2 reduction very challenging.[24]

Despite the very low efficiency, pure g-C_3N_4 (without any cocatalyst) can catalyse the reduction of CO_2 into other chemicals (e.g. CO,[346] CH_3CHO[347] and CH_4[347]), and the nature of the major CO_2 reduction product in the presence of water vapor can be modulated by the

band structure of bulk g-C_3N_4 and g-C_3N_4 nanosheets, as reported by Niu *et al.*[347] Other studies about the influence of electronic structure of g-C_3N_4-based systems on the product selectivity in CO_2 reduction were also performed and proposed that not only band position is responsible by this effect, but also the electron sink effect as well as the promoted charge transfer between composite components.[24, 277, 348-352]

Similar to photocatalytic water splitting, noble metals can be used as efficient cocatalysts for enhancing the photocatalytic CO_2 reduction performance of g-C_3N_4 (as summarized in **Table 2**). Yu *et al.* reported a great enhancement on the photocatalytic activity of g-C_3N_4 for reduction of CO_2 into hydrocarbon when Pt was added as cocatalyst in a range from 0.25 to 2 wt%. More interestingly, they also reported an important influence on the product by the Pt loading (**Fig. 17a**).[278] Other research group reported the reduction of CO_2 to CH_4 using g-C_3N_4 loaded with 0.5-10 wt% of Pt. As shown in **Fig. 17b**, better yields for CH_4 were obtained over the 2Pt/g-C_3N_4 with an optimal 2 wt% content of Pt, this catalyst presented reaction rate 5.1 times greater than pure g-C_3N_4. The noticeably improved photoactivity of Pt/g-C_3N_4 was assigned to the increased light absorption and effective interfacial electron transfer from g-C_3N_4 to Pt due to its lower Fermi level that prohibited the recombination of electron-hole pairs (**Fig. 17c**). In order to better understand the role of noble metals in the photocatalytic CO_2 reduction process, Gao and collaborators investigated the photocatalytic CO_2 reduction over g-C_3N_4 modified with single-atom of Pd or Pt by using DFT calculation. Comparing the rate-determining barriers of different possible reaction pathways, they found that the HCOOH was the favourable product of CO_2 reduction on the Pd/g-C_3N_4 catalyst, while over Pt/g-C_3N_4 was CH_4 (**Fig. 17d-e**). This work provided a theoretical support for the empirically observed product selectivity of photocatalytic CO_2 reduction.[353]

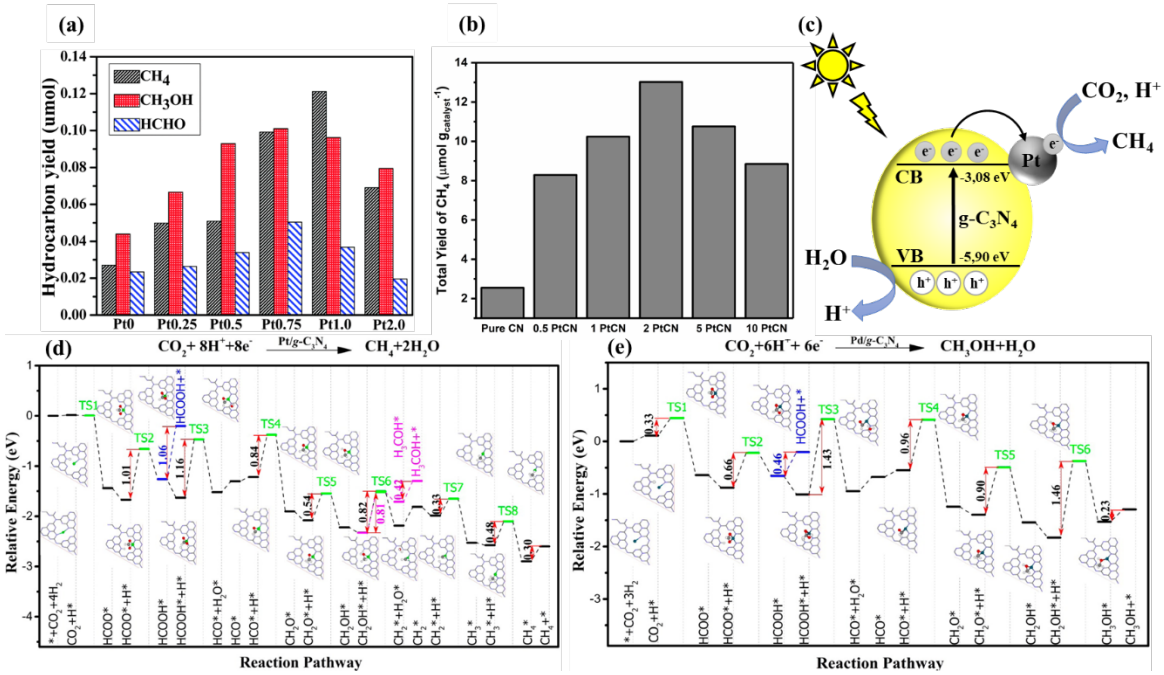

Figure 17. (a) Hydrocarbon yield produced by g-C_3N_4 decorated with Pt displaying different metal loadings (0-2.0 wt%) under the simulated solar light irradiation for 4 h of reaction. Reprinted with permission from ref [278]. Copyright 2014 Royal Society of Chemistry; (b) Total yield pf CH_4 over g-C_3N_4 loaded with Pt (0.25-2 wt%) after 10h of reaction. Reprinted with permission from ref [277]. Copyright 2014 Royal Society of Chemistry; (c) Schematic representation of the reduction of CO_2 with H_2O to CH_4 catalysed by Pt/g-C_3N_4 heterostructures. Adapted with permission from ref [277]. Copyright 2014 Royal Society of Chemistry; (d) Reaction pathways for CO_2 reduction to HCOOH, CH_3OH, and CH_4 on the Pt/g-C_3N_4 catalyst and (e) Pd/g-C_3N_4 catalyst. Under standard conditions (pH 0, $p(H_2)$=1 bar, U = 0 V vs SHE), the total energies of $H^+_{(aq)}$ + e^- and (1/2)$H_{2(g)}$ are equal. The reference energy (the total free energy of the catalyst, isolated CO_2, and four H_2) is set to zero. Color code: Pd, pine green; C, gray; O, red; H, white. Reprinted with permission from [353]. Copyright 2016 American Chemical Society.

Tu and collaborators have studied the impact of tuneable nitrogen vacancies on photocatalytic activities of Pt/g-C_3N_4 towards the CO_2 reduction into CO.[321] They observed a synergistic effect between nitrogen vacancies and Pt NPs, in which the density of nitrogen vacancies in an optimum range has a positive effect on the photocatalytic activities. This was due to the gradual enhancement of light harvesting, efficient charge separation and transportation, and the uniform binding of Pt on g-C_3N_4 as active reaction sites (**Fig. 18**). However, further increase of nitrogen vacancies decreased the photocatalytic activity,

because the deeper midgap states induced by overdoped nitrogen vacancies could become recombination sites of photogenerated electron-hole pairs.[321] Pt NPs cocatalyst on g-C_3N_4 were also used in combination with other heterostructures and tested to reduce CO_2 into CH_4, such as $NaNbO_3$ nanowires[354] and $KNbO_3$.[355] Enhancements in the photocatalytic activity were observed in these systems.

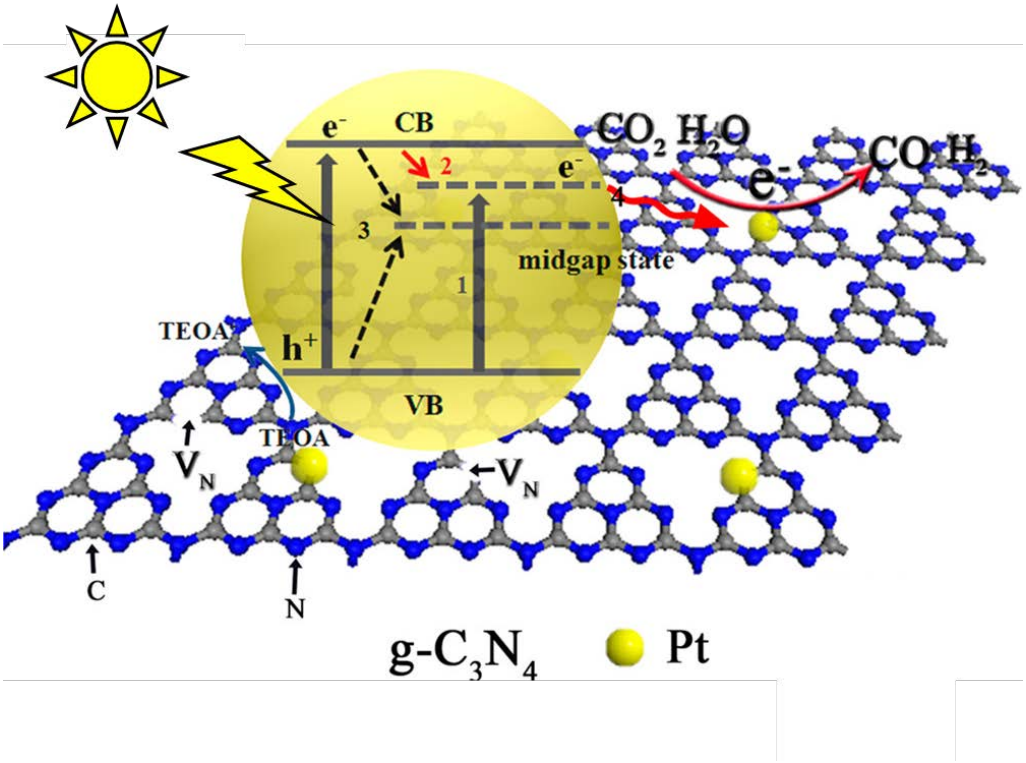

Figure 18. Schematic illustration of g-C_3N_4 nanosheets with nitrogen vacancies (VN) for photoreduction of CO_2 to CO and H_2 evolution. Paths 1, 2, and 4 refer to the electron excitation from the valence band to midgap states, the electron trapping from the conduction band to midgap states, and the electron transfer to reaction sites, respectively. Path 3 refers to deeper midgap states that act as recombination sites for trapping photogenerated electrons and holes. Reprinted with permission from ref [321]. Copyright 2017 American Chemical Society.

The nature of the exposed facet in noble metals (shape effect) can also significantly influence the product selectivity in CO_2 reduction, as demonstrated by Bai *et al.*[283] The authors investigated the facet-dependent selectivity of CO_2 reduction over Pd cocatalysts in the Pd/g-C_3N_4 system employing Pd NPs with {100} and {111} surface facets (cubes and tetrahedrons, respectively). The photocatalytic CO_2 reduction activity was significantly higher for g-C_3N_4 loaded with Pd tetrahedrons. Analysing the facet-dependent CO_2 reduction

process by first-principles calculations, it was found that the adsorption energy of CO_2 on the Pd-{100} (E_a = 0.064 eV) was lower than that for Pd-{111} (E_a = 0.230 eV). Moreover, the activation barrier E_B was reduced from 7.15 to 3.98 eV and from 6.79 to 4.15 eV for Pd-{111} and Pd-{100} facets, respectively, when two electrons were brought to the surfaces to initiate the activation of CO_2 (**Fig. 19**). This observation helped to explain why the Pd-{111} facets were more reactive for the reduction of CO_2. The Pd/g-C_3N_4 system works essentially similar to the Pt loaded system. When it is irradiated by light, the photoexcitation of electrons took place in g-C_3N_4. Due to larger work functions of Pd-{100} (5.05 eV) and Pd-{111} (5.23 eV) as compared with the g-C_3N_4 (4.31 eV) (**Fig. 19e-f**), the photoexcited electrons were rapidly shuttled to the Pd cocatalysts to retard the recombination of charge carriers, resulting in increased CO_2 reduction to CH_4, CO and C_2H_5OH.[28, 283] Similar results were reported by Cao *et al.* They found that during this reduction reaction, tetrahedral Pd NPs with exposed Pd-{111} facets are more active than cubic Pd NPs with exposed Pd-{100} facets. Their mechanistic investigation revealed that the structure-sensitive photocatalytic CO_2 reduction activity is mainly attributed to the more preferable electron sink effect, CO_2 adsorption capability and CH_3OH desorption capability of the Pd-{111} surface, as compared to Pd-{100}, due to their different surface atomic structures.[356]

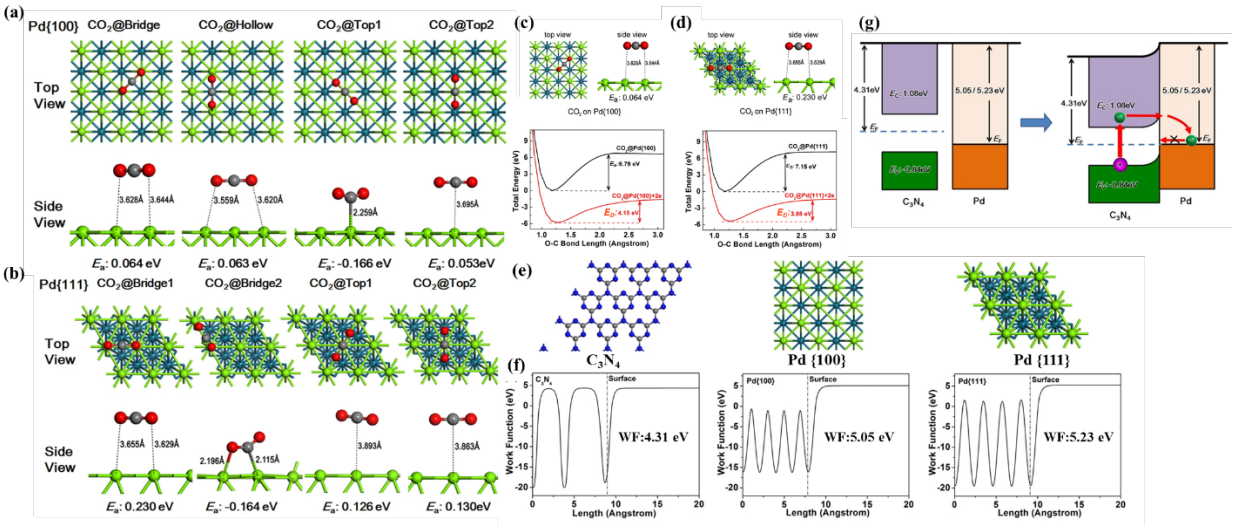

Fig. 19. (a and b) Top and side views of CO_2 adsorption configurations for Pd-{001} (a) and Pd-{111} (b) and their respective adsorption energy (E_a) according to the geometry optimization simulations; (c) Optimized configurations for the adsorption of CO_2 on the Pd-{100} and (d) Pd-{111} facets and their respective potential energy along the bond length O-C of the CO_2 molecule adsorbed under neutral conditions or charged with two electrons, from which the activation energy E_B of CO_2 is subtracted; (e) Model systems and (f) calculated

potentials with work functions for C_3N_4, Pd-{100}, and Pd-{111}; (g) Energy level diagrams for C_3N_4 and Pd before and after forming the interfaces for electron transfer based on first-principles calculations. Reprinted with permission from [283]. Copyright 2014 Royal Society of Chemistry.

Park and co-workers have investigated Pd/g-C_3N_4 on the direct synthesis of HCOOH under neutral conditions from CO_2. The g-C_3N_4 support was able to adsorb CO_2 and provide an activated form of carbonate or formate species to the Pd NPs. As a result, the activity of Pd/g-C_3N_4 catalyst was remarkably higher when compared to an inert support such as CNT. Moreover, the Pd/g-C_3N_4 catalyst exhibits remarkable stability during the catalytic reaction under neutral conditions, which is an essential property for the practical applications.[357] Pd NPs were also tested as a cocatalyst on g-C_3N_4 combined with layered double hydroxides (LDH). The authors reported that the close interaction of LDH nanosheets with g-C_3N_4 and Pd NPs leads to a more efficient interlayer CO_3^{2-} reduction as compared with the system without LDH.[358]

Au NPs have been tested towards the CO_2 reduction in a g-C_3N_4-based system only in Z-schemes, where the Au NPs and g-C_3N_4 are coupled with BiOBr.[359] Bai *et al.* studied the influence of the Au NPs size in Au/g-C_3N_4/BiOBr system for photocatalytic CO_2 reduction. The results revealed that larger Au NPs (100-150 nm) mainly displayed Z-scheme bridge role and presented higher photocatalytic activity than g-C_3N_4/BiOBr under 380 nm monochromatic light irradiation. Smaller Au NPs (10-20 nm) mainly displayed LSPR effect and showed higher photocatalytic activity than g-C_3N_4/BiOBr under 550 nm monochromatic light irradiation.[359] Ag NPs were also tested in a Z-Scheme for CO_2 reductions. He *et al.* observed the photoreduction of Ag^+ in Ag_3PO_4/g-C_3N_4 after 1h of irradiation (500 W Xe lamp). The resulting Ag_3PO_4/Ag/g-C_3N_4 system presented an enhanced photocatalytic activity for CO_2 reduction due to efficient separation of electron-hole pairs by a Z-scheme mechanism. The optimal Ag_3PO_4/Ag/g-C_3N_4 photocatalyst showed a CO_2 conversion rate of 57.5 μmol h^{-1} g_{cat}^{-1}, which was 6.1 higher than pure g-C_3N_4, under simulated sunlight irradiation.[360] Ag NPs were also tested in a system combining g-C_3N_4 and TiO_2. Despite not claimed by authors, the reported system seems to work in a Z-scheme. They reported that Ag/g-C_3N_4/TiO_2 was 12.7 times more active for CO_2 reduction than TiO_2 and 7.9 relatives to g-C_3N_4. According to the authors, the Ag NPs deposited on the g-C_3N_4/TiO_2 surface played an important role. They not only retarded the recombination of electron-hole pairs through extracting electrons from the conduction band of TiO_2 but also utilized the LSPR effect to

enhance the energy level of electrons accumulated on their surface.[361] It is important to highlight the urchin-like α-Fe_2O_3/g-C_3N_4 hybrid in Z-scheme recently reported by Jiang and collaborators, which presented excellent activity (10.3 μmol g^{-1} h^{-1}) to reduce CO_2 into CO without cocatalyst and sacrifice reagent.[309] A comparison of the photocatalytic activity for CO_2 reduction of all the systems presented in this section is shown in **Table 2**.

Table 2. Photocatalytic CO_2 reduction on metal NPs/g-C_3N_4 heterostructures

Catalysts	Fraction of cocatalysts	Total mass of catalysts	Light source (wavelength-nm)	Activity (unit)	QE (%)	Ref.
g-C_3N_4	-	0.20 g	300 W Xe lamp (>420 nm)	CH_3OH: 6.28 μmol g^{-1} h^{-1} C_2H_5OH: 4.51 μmol g^{-1} h^{-1}	0.18% (420 nm)	[351]
g-C_3N_4 nanosheets	-	N/A	300 W Xe lamp (>420 nm)	CH_4: 7.47 μmol $g^{-1}h^{-1}$	N/A	[362]
Pt/ g-C_3N_4	2 wt%	N/A	15 W LED-Lamp	CH_4: 13.02 μmol g^{-1}	N/A	[277]
Pt/g-C_3N_4	0.75 wt%	0.10 g	Solar simulator	CH_4: ~0.1 μmol CH_3OH:~0.12 μmol HCHO:~0.05 μmol	N/A	[278]
Pd-(111) /g-C_3N_4	11.6 wt%	0.01 g	300 W Xe lamp (>400 nm)	CH_4: 0.18 μmol g^{-1} h^{-1} CO: 14.90 μmol g^{-1} h^{-1} C_2H_5OH: 1.72 μmol g^{-1} h^{-1}	N/A	[283]
Pd-(001) /g-C_3N_4	11.9 wt%	0.01 g	300 W Xe lamp (>400 nm)	CH_4: N.d. CO: 5.6 μmol g^{-1} h^{-1} C_2H_5OH: 7.4 μmol g^{-1} h^{-1}	N/A	[283]
Ag_3PO_4/Ag/g-C_3N_4	Ag_3PO_4/g-C_3N_4 molar ratio: 30%	0.15 g	500 W Xe lamp (>420 nm)	CO_2 Reduction rate: 57.5 μmol g^{-1} h^{-1}	N/A	[360]
Ag/g-C_3N_4/TiO_2	55 wt%	0.05 g	300 W Xe lamp	CH_4: 28 μmol g^{-1} CO: 19 μmol g^{-1}	N/A	[361]
Pt/g-C_3N_4/$NaNbO_3$	0.5 wt%	0.05 g	300 W Xe lamp (>420 nm)	CH_4: 6.40 μmol g^{-1} h^{-1}	N/A	[354]
Pt/g-C_3N_4/$KNbO_3$	0.5 wt%	0.10 g	300 W Xe lamp (>420 nm)	CH_4: 0.25 μmol h^{-1}	N/A	[355]
Pd/g-C_3N_4/LDH	0.5 wt%	0.20 g	500 W Hg (Xe) lamp	CH_4: 3.7 μmol CO: 0.1 μmol C_2H_6: 0.06 μmol	0.093% (420 nm)	[358]
Au/g-C_3N_4/BiOBr	1.0 wt%	0.10 g	300 W Xe lamp	CH_4: 0.39 μmol g^{-1} h^{-1} CO: 0.05 μmol g^{-1} h^{-1}	N/A	[359]
α-Fe_2O_3/g-C_3N_4	-	0.025 g	300 W Xe lamp (0.21 W cm^{-2})	CO: 10.3 μmol g^{-1} h^{-1}	0.96% (420 nm)	[309]

6.3 Photocatalytic Degradation of Pollutants

Environmental pollution is a serious problem faced by the human race, hindering our sustainable development. In this context, the photocatalytic degradation of pollutants and environmental remediation constitute an important and wide-impact concern of the scientific community.[28] Photocatalysis has proven to be a promising strategy for environmental

decontamination due to its high efficiency and low cost.[363-365] g-C_3N_4 is a promising photocatalyst for pollutants degradation, due to its band position which exhibits moderately high oxidation ability. Its photogenerated electrons can reduce O_2 to produce $\bullet O_2^-$, while the photogenerated h^+ in some g-C_3N_4-based heterojunctions can oxidize OH^- to produce the highly oxidant radical •OH. These active species (h^+, $\bullet O_2^-$, •OH) can be put towards the oxidation of certain pollutants to mineralization (CO_2 and H_2O). In general, the photocatalytic degradation reactions over g-C_3N_4 can be categorized into two types: liquid phase removal of organic pollutants and gas phase degradation of pollutants, as summarized in **Table 3**. The photocatalytic degradation of pollutants also represents a simple approach to evaluate the photocatalytic activity of g-C_3N_4-based composites. Therefore, many studies which focus on the mechanistic investigation of the photoactivity of g-C_3N_4-based composites employ the photocatalytic degradation of pollutants as a model transformation.

Table 3. Utilization of g-C_3N_4-based photocatalysts in the degradation of pollutants

Catalysts	Fraction of cocatalysts	Total mass of catalysts	Light source (wavelength-nm)	Photocatalytic Experiment	Activity (%)	Ref.
g-C_3N_4	-	0.04 g	500 W Xe lamp (36 mW cm^{-2}) (>420 nm)	Degradation of RhB	100% degradation in 3.3h	[366]
Ag/ g-C_3N_4	4.0 wt%	0.10 g	500 W Xe lamp (>420 nm)	Degradation of MO Degradation of MB	98.2% degradation in 9 min 99.3% degradation in 45 min	[367]
Ag/g-C_3N_4	8 .0wt%	0.10 g	800 W Xe lamp (>420 nm)	Degradation of RhB	92.0% degradation in 0.5h	[368]
Ag/g-C_3N_4	1.0 wt%	0.15 g	500 W Xe lamp (>420 nm)	Degradation of MO	100% degradation in 3h	[272]
Ag/g-C_3N_4	5.0 wt%	0.10 g	300 W tungsten halogen lamp (>420 nm)	Degradation of MO	92.0% degradation in 1h	[273]
Ag@g-C_3N_4	0.5 wt%	0.025 g	500 W Xe lamp (>420 nm)	Degradation of MO	100% degradation in 5 min	[52]
Ag/mpg- C_3N_4	3.0 wt%	0.10 g	300 W tungsten halogen lamp (>420 nm)	Degradation of RhB	100% degradation in 25 min	[268]
Ag@AgBr/g-C_3N_4	70 wt% Ag@AgBr/ g-C_3N_4	0.10 g	300 W Xe lamp (>400 nm)	Degradation of MO Degradation of RhB	95% degradation in 10 min 92% degradation in 10 min	[369]
C_3N_4@Ag-Bi_2WO_6	2.7 wt%	0.05 g	350 W Xe lamp (>420 nm)	Degradation of RhB	70% degradation in 1.5h	[370]
g-C_3N_4/Ag/MoS_2	6.7 wt%	0.10 g	300 W Xe lamp	Degradation of	~100% degradation in 1h	[339]

			(172 mW cm^{-2}) (>420 nm)	RhB		
g-C_3N_4/Ag/Ag_3VO_4	1.5 wt%	0.05 g	250 W Xe lamp (>420 nm)	Degradation of RhB	95% degradation in 1.75h	371
g-C_3N_4@Ag@Ag_3PO_4	30 wt%	0.006 g	350 W Xe lamp (>420 nm)	Degradation of RhB	94.8% degradation in 1h	372
AgQC/g-C_3N_4	7.46 wt%	0.05 g	100 W Halogen lamp (>400 nm)	Degradation of MB Degradation of MO	~90% degradation in 0.5h ~90% degradation in 1.8h	326
g-C_3N_4/Ag/Ag_2CrO_4	8 wt% (Ag_2CrO_4/g-C_3N_4)	0.05 g	300 W Xe lamp (>420 nm)	Degradation of MB	58% degradation in 2h	373
g-C_3N_4/Ag/Ag_2PO_4	N/A	0.04 g	LED white-light lamp	Degradation of RhB	95% degradation in 10 min	374
g-C_3N_4/Ag/Ag_2PO_4	25 wt% (Ag_2PO_4/g-C_3N_4)	N/A	300 W Xe lamp (>400 nm)	Degradation of MO	100 % degradation in 5min	375
g-C_3N_4/Ag/Ag_2PO_4-(111) facet	10 wt% (g-C_3N_4/ Ag_2PO_4)	0.04 g	300 W Xe lamp (>400 nm)	Degradation of MB Removal of NO_x	100 % degradation in 0.2h 49.3% removal	376
g-C_3N_4/Ag/Ag_2PO_4	2.1 wt% (Ag_2PO_4/g-C_3N_4)	0.005 g	300 W Xe lamp (>400 nm)	Degradation of sulfamethoxazole (SMX)	100 % degradation in 1h	377
g-C_3N_4/Ag/Ag_2CO_3	25 wt% (g-C_3N_4/ Ag_2CO_3)	0.10 g	300 W Xe lamp (>400 nm)	Degradation of RhB	100% degradation in 0.5h	378
Ag/$SrTa_2O_6$/g-C_3N_4	2.0 wt%	0.025 g	300 W Hg lamp (3.45 mW/cm^{-2}) (>420 nm)	Degradation of MO Cr^{6+} photoreduction	100% degradation in 1.2h 100% reduction in 1.7h	379
Ag/AgO/ g-C_3N_4	10 wt%	0.10 g	12 lamps of 100 Oreva)	Degradation of Acid Violet-7	98% degradation in 10 min	380
Pt/g-C_3N_4	2.0 wt%	0.10 g	300 W Xe lamp (>420 nm)	Degradation of PCP	~100% degradation in 7h	276
Pd/mpg- C_3N_4	1.5 wt%	0.10 g	Solar simulator	Degradation of BPA	93.9% degradation in 3h	284
Au/g-C_3N_4	N/A	0.045 g	500 W Xe lamp (>400 nm)	Degradation of MO	92.6 % degradation in 2.5h	264
Au/TiO_2/g-C_3N_4	2.0 wt%	0.20 g	150 W Xe lamp (>400 nm)	Degradation of PCP Degradation of BPA	46% degradation in 1h 37% degradation in 1h	381
Au/g-C_3N_4/Fe_2O_3	N/A	0.05 g	N/A	Degradation of RhB	100% degradation in 50 min	382
Au/CNT/g-C_3N_4	5.5 wt%	0.05 g	Visible light source (50 mW/cm^{-2})	Degradation of RhB	~100% degradation in 50 min	383
Au/graphene/g-C_3N_4	1.0 wt%	0.10 g	500 W Xe lamp (>420 nm)	Degradation of MB	96.7% degradation in 4h	384
Au/GO/g-C_3N_4	1.0 wt%	0.05 g	500 W Xe lamp (>420 nm)	Degradation of RhB	99.4% degradation in 2h	385
CdS/Au/g-C_3N_4	N/A	0.05 g	300 W Xe lamp	Degradation of	90.1% degradation in 10	386

			(>400 nm)	RhB	min	
Au/Pt/g-C_3N_4	2.0 wt% (Au) 0.5 wt%(Pt)	0.10 g	500 W Xe lamp (>400 nm)	Degradation of TC-HCl	93% degradation in 2h	[387]
Au-Ag/g-C_3N_4	3.0 wt% (Au) 1 wt%(Ag)	0.10 g	450 W Xe lamp (>400 nm)	Degradation of RhB	90% degradation in 4h	[388]
Au-Pd/g-C_3N_4	3.2 at%(Au) 6.0 at% (Pd)	0.50 g	Solar Ligth (600-900 W m^{-2})[389]	Degradation of Phenol	94.4% degradation in 5h	[389]
Cu/g-C_3N_4	33 wt%	0.04 g	300 W Xe lamp (>400 nm)	Degradation of MB	~100% degradation 0.25h	[390]
Cu_2O/Cu/g-C_3N_4	20 at%(	0.05 g	300 W Xe lamp (>420 nm)	Degradation of MO Degradation of Phenol Degradation of RhB	99% degradation in 40 min ~100% degradation 4h 94.3% degradation in 2h	[391]
Bi@BiOCl/g-C_3N_4	N/A	0.02 g	300 W Xe lamp	Degradation of DCP Cr^{6+} photoreduction Degradation of MO	80% degradation in 2h 82.3% reduction in 1.3h 70% degradation in 2h	[301]
Bi/g-C_3N_4@Bi_2WO_6	4.6 wt%	0.10 g	300 W Xe lamp (>400 nm)	Degradation of RhB Degradation of DCP	100% degradation in 0.5h 70% degradation in 3h	[392]
Bi/g-C_3N_4	11.8 wt%	0.20 g	150 W Tungsten halogen lamp (>420 nm)	Removal of NO_x	60.8% removal in 1h	[393]
Ag/g-C_3N_4	10.0 wt%	0.20 g	300 W Xe lamp (>400 nm)	Removal of NO_x	54.3% removal	[394]
Ag/g-C_3N_4/WS_2	2.0 wt%	0.10 g	300 W Xe lamp	Removal of NO_x	72.5% removal in 1h	[395]

6.3.1 Liquid Phase Degradation of Pollutants

The removal of pollutants in wastewater effluents, especially organic pollutants (e.g. dyes, antibiotics, bisphenol A, phenols), has been addressed by advanced oxidation processes commonly catalysed by a variety of photocatalysts, which include g-C_3N_4-based materials. In these studies, the dyes methyl orange, methylene blue and Rhodamine B (RhB) have been employed as model molecules (so that the reaction can be monitored by a spectrophotometer). In the context of water purification, H_2O_2 is one of the most widely used green oxidants, which typically requires a catalyst for activation into more reactive oxidizing intermediates.[28, 366] Cui *et al.* have demonstrated the metal-free activation of H_2O_2 by g-C_3N_4

under visible light irradiation, using the decomposition of RhB in aqueous solution as a proof-of-concept reaction. The authors reported that g-C_3N_4 was capable of activating H_2O_2 to generate reactive oxy-radicals, which in turn led to the mineralization of the dye.[366] Interestingly, other studies have used O_2 as oxidant. For example, Yang *et al.* exploited the LSPR effect of Ag NPs in Ag-deposited g-C_3N_4 plasmonic photocatalysts towards the methyl orange degradation. In general, when g-C_3N_4 is excited by visible-light, the generation of $\bullet O_2^-$ and h^+ takes place. Here, its band structure does not promote the formation of •OH species. It was found that for Ag/g-C_3N_4 systems, •OH radicals also took part in the photocatalytic reactions, thus giving the direct evidence to contribute to its increased catalytic performance.[273] The same research group later reported the fabrication of Z-scheme plasmonic photocatalyst Ag@AgBr/g-C_3N_4 to further enhance the photocatalytic activity. The high activity achieved in the degradation of methyl orange was attributed to the Z-scheme system, which retained the photoinduced electrons with strong reduction power in the conduction band of g-C_3N_4 and h^+ with strong oxidation power in the valence band of AgBr.[369]

Recently, Ag NPs have been used to improve photocatalytic activities in g-C_3N_4-based Z-scheme systems.[299, 339, 370, 396] For example, Xiao *et al.* reported enhanced photocatalytic performances for degradation of RhB by a C_3N_4@Ag-Bi_2WO_6 material.[370] Ag NPs also have been used in a Z-scheme system for RhB[339, 371, 372] and methyl orange (MO)[326, 373] photodegradation. Several studies have reported the spontaneously photodeposition of Ag NPs during the photocatalytic reaction for Ag compounds/g-C_3N_4 materials due to the Ag^+ photoreduction to generate Ag NPs under light irradiation.[373, 374, 397] g-C_3N_4 have been reported to construct Z-scheme systems *via* the formation of Ag NPs during the photocatalytic reaction with Ag_3PO_4,[360, 374-377, 397] Ag_2CrO_4[373] and Ag_2CO_3.[378] Generally, the Ag-compounds/g-C_3N_4 system behaves according to a traditional heterojunction. However, the excited electrons have enough reduction ability to convert Ag^+ into Ag^0. Consequently, the two-phase system is gradually transformed into a three-phase Z-scheme system under light illumination. Notably, Ag NPs can strongly absorb the visible light by LSPR effect.[398-400] It has been reported that Ag NPs can simultaneously exhibit the LSPR effect and serve as electron mediators in some Ag-compound/Ag/g-C_3N_4 systems improving its photocatalyst activity.[299, 339, 369, 401]

g-C_3N_4-based Z-scheme systems were also applied for NO oxidation[396] and Cr(VI) photoreduction.[379] Su *et al.* decorated $SrTa_2O_6$/g-C_3N_4 with Ag NPs as catalysts. An enhancement of the visible light absorption efficiency and a promotion of the photocatalytic

activity by a factor of 2.8 for Cr(VI) photoreduction and 4.6 for methyl orange degradation were observed as compared with only $SrTa_2O_6$/g-C_3N_4 (**Fig. 20a-d**). Ag decoration on $SrTa_2O_6$/g-C_3N_4 not only extended the visible light absorption region due to LSPR effects but also act as an electron mediator for efficient migration of photogenerated electrons and simultaneously prevent the recombination of photogenerated electron-hole pairs (**Fig. 19e**).[379]

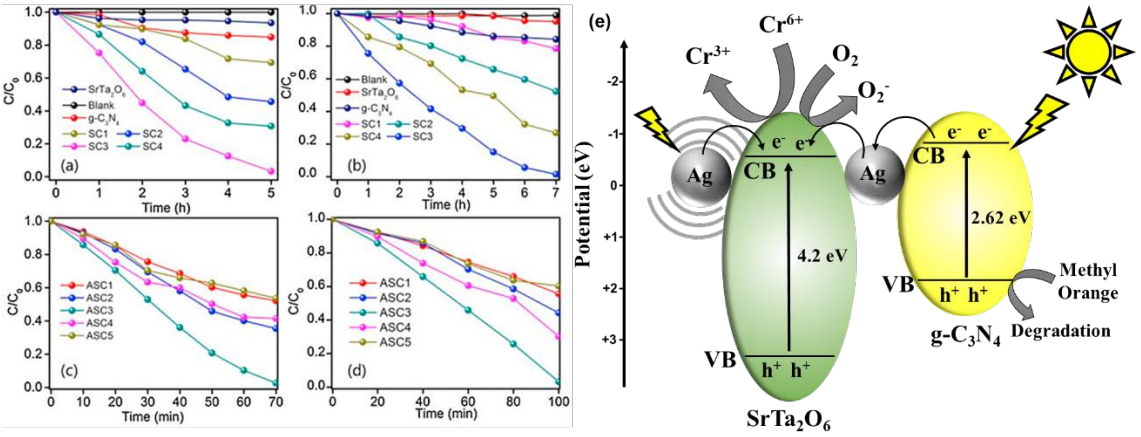

Figure 20. Change in methyl orange concentration (a and c) and in Cr(VI) concentration (b and d) as a function of the irradiation time for $SrTa_2O_6$/g-C_3N_4 (a and b) and Ag/$SrTa_2O_6$/g-C_3N_4 photocatalysts. Reprinted with permission from ref [379]. Copyright 2015 Elsevier; (e) Schematic representation of a possible mechanism for Cr(VI) photoreduction and methyl orange degradation over Ag/$SrTa_2O_6$/g-C_3N_4 photocatalytic system under visible light irradiation. Adapted with permission from ref [379]. Copyright 2015 Elsevier.

Ag NPs also display antibacterial activity. Bing and co-workers successfully improved visible-light-driven antibacterial activity and dispersal of biofilms by embedding Ag NPs on g-C_3N_4.[271] The Ag/g-C_3N_4 hybrids were much more effective to reactive oxygen species (ROS) generation under visible light. The composite was efficient as a bactericidal agent for both Gram-negative (G^-) *E. coli* and Gram-positive (G^+) *Staphylococcus aureus* (*S. aureus*) under visible-light illumination.[271] Muñoz-Batista *et al.* tested Ag/g-C_3N_4 biocidal capability against *E. coli* and it system displayed significantly higher antibacterial capabilities compared to the single components of Ag NPs and g-C_3N_4.[270] Upon UV light illumination, the Ag/g-C_3N_4 system was demonstrated be more effective on charge separation, which left hole-related radicals at the g-C_3N_4 support and electrons on the Ag NPs. Meanwhile, under visible excitation, the LSPR effect of Ag played an essential role in the biocidal action. In this regard, a complex phenomenon involving adsorption, radical attack as well as deactivation process of the interaction between microorganism and photocatalyst took place

simultaneously.[270] It is noteworthy that the bactericidal action was greatly influenced by both electron and hole-related charge species, which could be confirmed by the EPR measurements of the charge radicals produced from the photoactivity.[28]

In addition to Ag, Au also has been widely used to improve the g-C_3N_4 photodegradation performance. Cheng *et al.* reported superior photocatalytic activities for the decomposition of methyl orange under visible-light after decorating g-C_3N_4 nanosheets prepared by ultrasonication-assisted liquid exfoliation of bulk g-C_3N_4 with Au NPs deposited *via* green photoreduction of $HAuCl_4$.[264] Chang *et al.* reported an Au/g-C_3N_4 nanorods with high activity for photodegradation of a range of pollutants, such as RhB, 4-chlorophenol (4-CP), tetracycline (TC) and reduce (Cr(VI)).[402] Au NPs also have been used to decorate g-C_3N_4 combined with other heterostructures (e.g. TiO_2,[381] Fe_2O_3[382] and CdS)[386] for the photodegradation of pollutants. It is noteworthy the results obtained by Zada and co-workers using the ternary component Au/TiO_2/g-C_3N_4), which presented an improvement of 5.11-folds for photodecomposition of 2,4-dichlorophenol (2,4-DCP) when compared with pure g-C_3N_4. They reported an exceptional visible-light for the fabricated Au-(TiO_2/g-C_3N_4) nanohybrids, which was attributed to the extended visible-light response due to the Au NPs LSPR and its catalytic function, and to the enhanced charge separation by transferring electrons from g-C_3N_4 and Au to TiO_2. This promoted electron transfer for the TiO_2 favored the formation of hydroxyl radicals (•OH), which are very effective in the photocatalytic oxidation process of 2,4-DCP.[381] Furthermore, Au NPs also have been widely used in combination with carbon nanostructures, such as CNT[383] and GO.[385] This carbon nanostructures, in general, work as an electron transporter and acceptor facilitating the charge transfer and avoiding the recombination of photoexcited electron-hole pairs.[385]

Despite its more restrict use in photodegradation applications, possibly due to its prohibitive price, the activity of Pt NPs has also been evaluated to degradation of pollutants. In order to minimize the influence of the Pt price in the application feasibility of Pt/g-C_3N_4 for photodegradation, Xu and collaborators wisely coupled the photodegradation of the macrolide antibiotics Roxithromycin (Rox) with H_2 production reaction. The authors found that macrolide antibiotics present in water act as a sacrificial agent to consume H_2O_2 (side product from H_2 production), itself being degraded, leading to an enhancement of the H_2 yield (**Fig. 21**).[403] Pt NPs were also tested on g-C_3N_4 nanotubes towards the photodegradation of p-chlorophenol, p-nitrophenol, methylene blue and RhB, under visible-light irradiation. The authors reported a superior photocatalytic activity as compared to only g-C_3N_4 nanotubes

and attributed it to the synergic effect of Pt NPs on the unique tubular nanostructure of g-C_3N_4 nanotubes.[276]

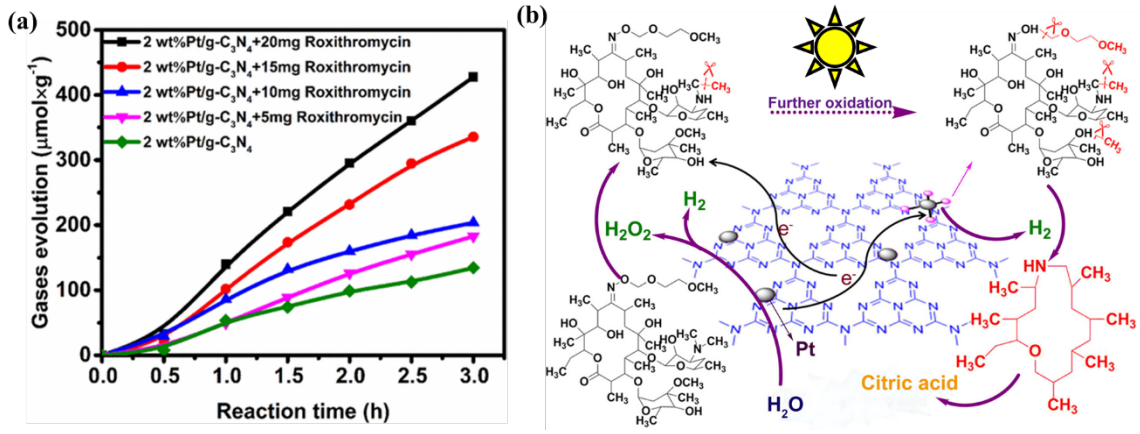

Figure 21. (a) Photocatalytic water splitting to H_2 catalyzed by 40 mg of 2 wt% Pt/g-C_3N_4 in 100 mL of water with different amounts of Rox; (b) Proposed reaction mechanism for the enhancement in the simultaneous water splitting and degradation of the Rox reaction by using Pt/g-C_3N_4 under the visible light irradiation. Reprinted with permission from ref [403]. Copyright 2017 American Chemical Society.

Bisphenol A (BPA) is another common pollutant. It is widely used in the manufacturing of consumer goods. Owing to its wide application, a large amount of bisphenol A has been released into the environment, leading to ubiquitous presence of bisphenol A in natural water.[404] Thus, an extensive research effort has been devoted to the remediation of this problem. Chang *et al.* investigated the degradation of BPA in water by Pd decorated mesoporous g-C_3N_4 (Pd/mpg-C_3N_4).[284] The catalyst modified with Pd NPs presented a higher photoactivity compared with only mpg-C_3N_4. This higher activity was attributed to the enhanced light absorbance in the UV-VIS region, along with the ability of the Pd NPs to act as electron traps and facilitate the separation of charge carriers.[284]

There are some successful examples where g-C_3N_4 was decorated with bimetallic NPs in order to improve its photocatalytic activity towards photodegradation reactions. Xue *et al.* fabricated Au/Pt co-decorated g-C_3N_4 heterostructure by a facile calcination-photodeposition technique, which displayed enhanced photocatalytic activity for antibiotic tetracycline hydrochloride (TC-HCl) degradation. The degradation rates were up to 3.4 times higher than that of pure g-C_3N_4 under visible light irradiation. The authors attributed this enhancement in the photocatalytic activity to the LSPR effect of Au and electron-sink function of Pt NPs, which improve the optical absorption property and photogenerated charge carriers separation

of g-C_3N_4, synergistically facilitating the photocatalysis process.[387] Gondal *et al.* used a different approach, instead of using co-decorated bimetallic NPs, they used AuAg NPs alloys in order to take better advantage of the LSPR properties of these NPs. As a result, AuAg/g-C_3N_4 photocatalysts exhibited significantly higher activity for the decolorization of RhB in the visible light as compared to the monometallic Ag and Au NPs counterparts on g-C_3N_4.[388] Bimetallic AuPd NPs alloys on g-C_3N_4 was recently applied for photodegradation of carcinogenic phenolic compounds and displayed superior photocatalytic activity compared with the previously reported AuPd/rGO. Photoluminescence results demonstrated that the efficient charge separation and delayed recombination of photo-induced electron-hole pairs in the AuPd/g-C_3N_4 nanocomposite were responsible for its superior activity.[389]

Besides the noble metals, non-noble metals such as Bi and Cu can be very useful to improve photocatalytic properties of g-C_3N_4. The most common strategy consists in making use of the plasmonic properties of the metal NPs to improve visible light absorption and reduce the recombination of electron-hole pairs. This strategy has been reported by Sierra *et al.* for the Bi spheres/Bi mixed oxides/g-C_3N_4 nanohybrids[405] and Gao *et al.* for the system Cu-g-C_3N_4 synthesised by a supramolecular approach.[390] Other interesting example using the low-cost metal Bi to improve progradation was reported by Wang *et al.*[392] The authors deposited plasmonic Bi NPs on g-C_3N_4@Bi_2WO_6 microspheres *via* a hydrothermal method. Bi NPs inserted in the interlayer between g-C_3N_4 and the surface of Bi_2WO_6 microspheres worked as an electron-conduction bridge enhancing the visible light absorption due to the LSPR effect, consequently facilitating the efficient electron-carrier separation. As a result, they observed an extraordinary enhanced photocatalytic activity for decomposition of 2,4-DCP relative to the g-C_3N_4, Bi_2WO_6, and g-C_3N_4(20%)@Bi_2WO_6 samples. It implies that the heterostructured combination of g-C_3N_4, metallic Bi NPs, and Bi_2WO_6 microspheres provided synergistic photocatalytic activity *via* an efficient electron transfer process. The low-cost metals Bi and Cu were also used to fabricate Z-scheme systems, such as Bi@BiOCl/g-C_3N_4 and Cu_2O/Cu/g-C_3N_4,[391] which were applied for photodegradation of pollutants.[301]

6.3.2 Gas Phase Degradation of Pollutants

The use of metal NPs/g-C_3N_4 heterostructures in the topic of gas phase photodegradation is essentially limited to the oxidation of nitric oxide (NO). Nitrogen dioxide and nitric oxide, also known as NO_x, are common air pollutants generated from the combustion of fossil fuels

and vehicle exhaust. They are responsible for atmospheric pollutions (e.g. acid rain and urban smog). In view of these facts, there is a growing environmental concern and thereby an intense search for efficient catalysts capable to oxidize NO.[28] Sano *et al.* were the first to report the application of g-C_3N_4 photocatalysts for the oxidation of NO. However, the authors observed low oxidation rates under visible light.[406] Despite the efforts of Wang and co-workers a few years later trying to improve the surface area of the g-C_3N_4 hoping to obtain higher oxidation rates, no satisfactory improvements on the NO oxidation was observed. Thus, the combination of g-C_3N_4 with a cocatalyst seems to be an interesting strategy to improve the photocatalytic activity for NO oxidation reaction.[407] Sun *et al.* resorted to this strategy by hybridizing g-C_3N_4 with Ag NPs. Their results showed that the decoration of Ag NPs not only enhanced the visible light absorption of the hybrid but also benefited the oxidation of NO to the final products (NO_2 and NO_3^-). The authors attributed the visible enhancement in light absorption due to the LSPR of Ag NPs and the increase in the NO oxidation due to improved separation and transfer of photoinduced carriers over Ag/g-C_3N_4 composites, which was supported by the PL spectra.[394] Ma and co-workers reported even more significant increment on the activity for NO oxidation in g-C_3N_4/WS_2 decorated with Ag NPs. Their optimized system was 3.70, 1.90 and 1.17 times more active for NO oxidation than that of g-C_3N_4, WS_2, and g-C_3N_4/WS2, respectively.[395]

Another promising cocatalyst for NO oxidation due to its low-cost is Bi. Jiang *et al.* reported the deposition of Bi NPs on g-C_3N_4. This system was employed as a photocatalyst in removing ppb-level NO in a continuous gas flow under visible light illumination. The Bi NPs significantly enhanced the performance of g-C_3N_4, and this enhancement arises from the heterojunction effect and LSPR effect of Bi NPs. However, Jiang *et al.* also investigated the contribution of each effect (heterojunction and LSPR effect), since they are highly dependent on the size of Bi NPs. By tuning the size of Bi NPs, the authors concluded that Bi NPs with 12 nm represents the optimum size to favor the synergy of these two effects (**Fig. 22c-d**).[393] In another paper, Dong *et al.* constructed an Bi NPs/g-C_3N_4 displaying highly enhanced visible-light photoactivity and stability for NO purification as compared to that of pristine g-C_3N_4.[285] The strengthened photocatalytic performance was attributed to the co-contributions of the notably improved light-harvesting, owing to the LSPR effects of Bi nanospheres, and the increased separation efficiency of electron-hole pairs due to the electron trapping effect of Bi metal in the heterostructured system. The local electromagnetic field arising from the LSPR effects of Bi was simulated with a rigorous Maxwell's solver based on the finite integration techniques (**Fig. 22a**), where a significant enhancement of electromagnetic field

under visible light could be observed. This electromagnetic field accelerates the photoexcited electrons and holes separation. Furthermore, the nearby Bi NPs can act as electron traps to facilitate the separation of photoinduced electron-hole pairs (**Fig. 22b**).[285]

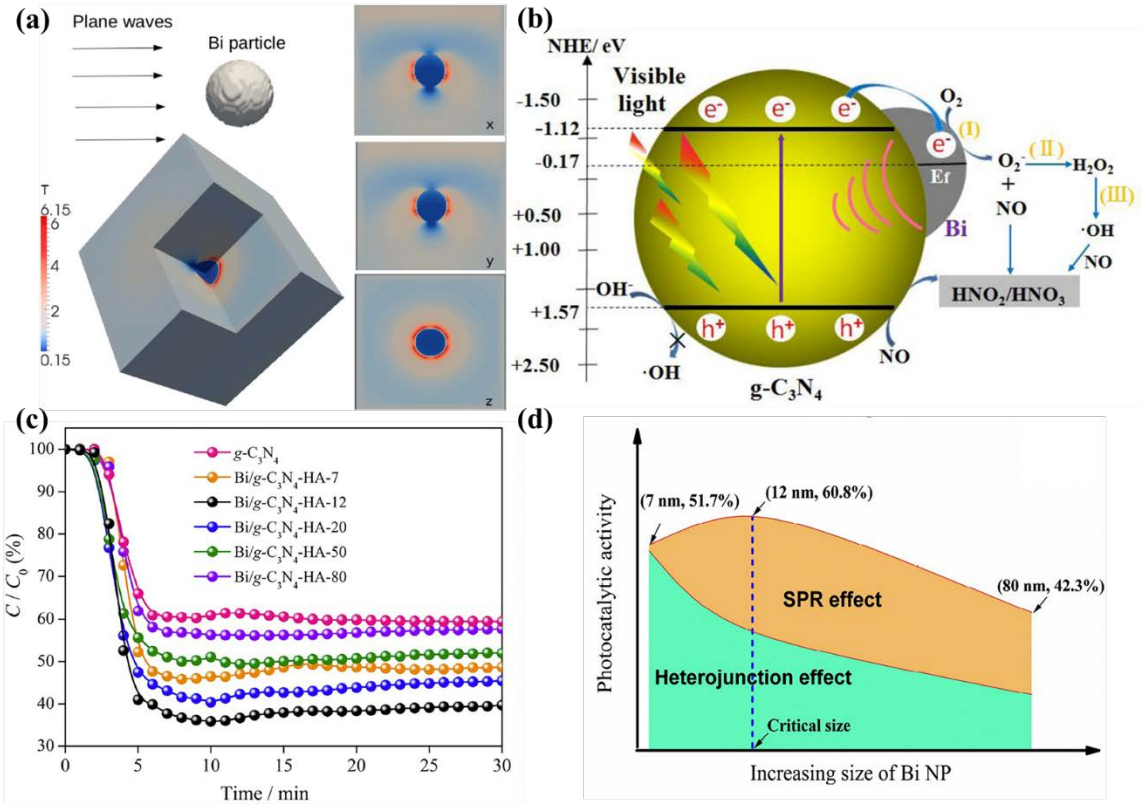

Figure 22. (a) Simulation of the LSPR-induced local electromagnetic field in the Bi NPs when it is illuminated by a plane wave with a wavelength of 420 nm from the z-direction. A three-dimensional view and two-dimensional cross-sections perpendicular to the x, y, and z-axes are shown. The scale bar shows the relative increase in field enhancement $T = |E/E_{inc}|^2$. (b) Visible-light-induced charge separation and a proposed mechanism for NO oxidation photocatalysed by Bi/g-C_3N_4. Reprinted with permission from ref [393]. Copyright 2015 American Chemical Society. (c) Photocatalytic activity for NO oxidation catalyzed by gC_3N_4 and Bi/gC_3N_4 materials containing Bi NPs of different sizes (Bi loading of 11.8 ± 4wt%); (d) Schematic of the synergy of the size-dependent heterojunction and LSPR effect of Bi NPs on the photocatalytic activity. Reprinted with permission from ref[285]. Copyright 2017 Elsevier.

7.5 Other Photocatalytic Applications

In addition to the transformations presented in the previous sections, metal NPs/g-C_3N_4 have also been employed for other transformations. For example, Verma and collaborators studied the photocatalytic C-H activation and oxidative esterification photocatalysed by Pd/g-C_3N_4. The authors reported excellent yields (>90%) for the conversion of a broad scope of aromatic alcohols into esters. Although only preliminary investigations about the reaction mechanism been performed, it is possible to affirm that the reaction proceeds *via* a C-H activation, which depends on O_2 to occur. The activated carbon is then attacked by the alcohol used as reaction solvent, in this case methanol, leading to the ester as final product.[408]

It is important to note that the applications of carbon nitrides are not limited to only photoreactions. Despite not being reviewed in this publication, carbon nitrides and metal NPs/g-C_3N_4 hybrids have been put to work in electrocatalysis, hydrogenations, and oxidations. Moreover, a number of emerging intrinsic properties of g-C_3N_4 allow its novel applications outside of conventional catalysis. Recently, Antonietti *et al.* compiled these unconventional applications in an excellent review, covering applications of g-C_3N_4 in a range of areas, such as sensing, bioimaging, photovoltaic cells, templating, and the construction of carbon nitride based devices.[409]

7. Conclusions and Perspectives

We presented herein a comprehensive overview of metal NPs/g-C_3N_4-based heterostructures, focusing on their design principles, photocatalytic applications, and charge-transfer mechanisms. The versatility of the g-C_3N_4 with respect to control over its electronic band structure, composition, crystallinity, vacancies sites, porosity, and active sites at its surface, make this material an exceptional candidate for the formation of hybrids with metal NPs. The metal NPs can possess a range of tunable properties (e.g. optical and catalytic properties as a function of shape, size, and composition) that, when combined with a g-C_3N_4, can be harnessed for improved photocatalysis. The recent and intense investigation in the synthesis and application of NPs/g-C_3N_4-based hybrids confirm that these materials represent an important class of photocatalysts for transitioning towards a sustainable future.

Despite the great progress in the area, we believe that we are still at the early stages in terms of material design and photocatalytic efficiency, which remains low for widespread applications. In order to overcome these challenges, we believe that several issues need to be addressed as described below:

(1) A fundamental understanding of the mechanism behind the charge transport in metal NPs/g-C_3N_4-based photocatalysts is critical. It is essential to unravel the charge cascading process in detail to allow an optimum utilization of light through photogenerated charge carriers for driving charge-transfer reactions. It is required to understand the charge generation, separation, and transportation across the nanoscale. This is especially important for Z-scheme systems, which remain poorly understood. For instance, *in situ* characterization can be very valuable for probing the electron-hole transfer pathways, being quite promising for enabling the design of more efficient metal NPs/g-C_3N_4-based photocatalysts having higher quantum efficiencies and thus economic viability.

(2) The interface of metal NPs/g-C_3N_4-based photocatalyst is a complex system, but very important for photocatalytic activity. Consequently, it is imperative to investigate interface effects in detail, especially regarding metal-support interactions, shape effect, nanoscale assembly, composition, density of defects, vacancies, and bandgap adjustment.

(3) The development and utilization of theoretical models and approaches to understand metal NPs/g-C_3N_4-based systems, such as electronic structure modelling of surface-adsorbate interactions and its integration it with the effect of light excitation.

(4) Metal NPs/g-C_3N_4 systems exhibit high photocatalytic activities. However, their practical application is limited by the high price and low abundance of noble metals. This limitation can be circumvented by replacing the expensive metal by for low-cost alternatives. This review presented some examples of low-cost metals (e.g. Cu, Bi, and Fe) being used as alternative photocatalysts to noble metals. Another strategy is to enhance the atom utilization efficiency of noble metals, for example by synthesizing highly active systems containing noble metals (which enable one to reduce its loading in the reaction) and single-atom noble metal-deposited g-C_3N_4 materials. So far, facile and efficient methods for preparing single-atom noble metal modified g-C_3N_4 systems are challenging and deserve further exploration. The stability of these systems it is also extremely important to make them economically viable. Hence, it is critical to address chemical corrosion and/or degradation of the photocatalysts.

(5) Finally, synergistic efforts in the areas of controlled synthesis, precise characterization (both *ex* and *in situ*), mechanistic investigation, and modelling will be needed in order to move beyond the state-of-the-art in the field of photocatalysis and enable the

widespread utilization of metal NPs/g-C_3N_4 materials towards sustainable molecular transformations.

It is a consensus in the scientific community that a sustainable economy must have its process driven by sunlight. Hence, photocatalytic systems will have a protagonist role in our journey to a green future. In this context, photocatalytic systems based on earth-abundant elements, such as g-C_3N_4, are particularly attractive. Furthermore, the synthesis of metal NPs and g-C_3N_4 have been recently successfully scaled-up to the kilogram scale,[92, 410, 411] which make these hybrids photocatalysts, even more, promising for future practical applications.

The precise understanding of the charge transport mechanism combined with the high level of control over the materials syntheses, their combination, and characterization can take the topic of photocatalysis with g-C_3N_4 to a new level, potentially enabling us to move from an observation-driven to a design-driven approach (**Fig. 23**). In this case, specific properties and the performance of the photocatalytic systems can be planned in advance, and the target material synthesized accordingly. We are confident that the continuous efforts of the scientific community in synthesis, characterization, and mechanistic understanding, modelling, and assessment in photocatalysis is paving the way for cleaner energy generation as well as more efficient and sustainable processes.

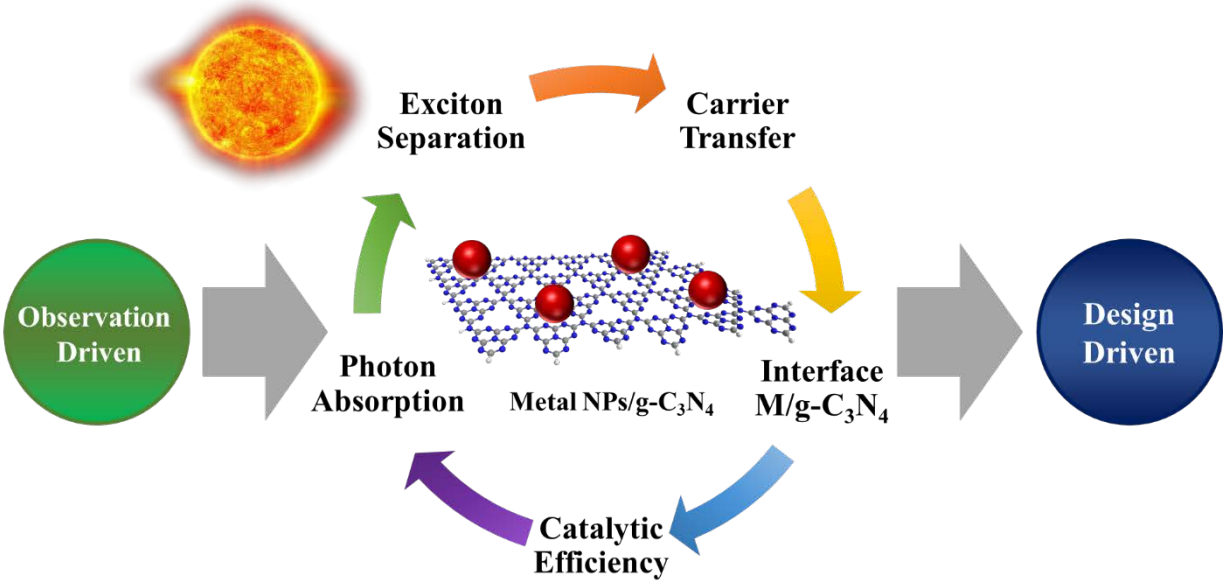

Figure 23. Schematic representation of the critical points which must be understood in photocatalysis promoted by metal NPs/g-C_3N_4 to allow the transition from an observation-driven to a design-driven approach.

8. References

1. N. S. Lewis and D. G. Nocera, *Proceedings of the National Academy of Sciences*, 2006, **103**, 15729-15735.
2. J. Bisquert, *Nature Photonics*, 2008, **2**, 648-649.
3. A. J. Ragauskas, C. K. Williams, B. H. Davison, G. Britovsek, J. Cairney, C. A. Eckert, W. J. Frederick, Jr., J. P. Hallett, D. J. Leak, C. L. Liotta, J. R. Mielenz, R. Murphy, R. Templer and T. Tschaplinski, *Science* 2006, **311**, 484-489.
4. C. Chen, W. Ma and J. Zhao, *Chemical Society Reviews*, 2010, **39**, 4206-4219.
5. S. Linic, P. Christopher and D. B. Ingram, *Nat Mater*, 2011, **10**, 911-921.
6. A. J. Esswein and D. G. Nocera, *Chemical reviews*, 2007, **107**, 4022-4047.
7. J. Yu, J. Low, W. Xiao, P. Zhou and M. Jaroniec, *Journal of the American Chemical Society*, 2014, **136**, 8839-8842.
8. G. Liu, L. Wang, H. G. Yang, H.-M. Cheng and G. Q. M. Lu, *Journal of Materials Chemistry*, 2010, **20**, 831-843.
9. M. D. Hernández-Alonso, F. Fresno, S. Suárez and J. M. Coronado, *Energy & Environmental Science*, 2009, **2**, 1231-1257.
10. H. Tong, S. Ouyang, Y. Bi, N. Umezawa, M. Oshikiri and J. Ye, *Advanced materials*, 2012, **24**, 229-251.
11. S. Peiris, J. McMurtrie and H.-Y. Zhu, *Catalysis Science & Technology*, 2016, **6**, 320-338.
12. M. A. Fox and M. T. Dulay, *Chemical reviews*, 1993, **93**, 341-357.
13. X. Wang, K. Maeda, A. Thomas, K. Takanabe, G. Xin, J. M. Carlsson, K. Domen and M. Antonietti, *Nat Mater*, 2009, **8**, 76-80.
14. Y. Wang, X. Wang and M. Antonietti, *Angewandte Chemie International Edition*, 2012, **51**, 68-89.
15. X. Wang, S. Blechert and M. Antonietti, *ACS Catalysis*, 2012, **2**, 1596-1606.
16. A. Thomas, A. Fischer, F. Goettmann, M. Antonietti, J.-O. Müller, R. Schlögl and J. M. Carlsson, *Journal of Materials Chemistry*, 2008, **18**, 4893-4908.
17. D. S. Su, J. Zhang, B. Frank, A. Thomas, X. Wang, J. Paraknowitsch and R. Schlögl, *ChemSusChem*, 2010, **3**, 169-180.
18. S. Cao, J. Low, J. Yu and M. Jaroniec, *Advanced Materials*, 2015, **27**, 2150-2176.
19. Y. Zheng, J. Liu, J. Liang, M. Jaroniec and S. Z. Qiao, *Energy & Environmental Science*, 2012, **5**, 6717-6731.
20. F. Su, M. Antonietti and X. Wang, *Catalysis Science & Technology*, 2012, **2**, 1005-1009.
21. Y. Si, J. Zhong, J. Li, X. Liu, W. Hu, J. Song, F. Zhang, K. Liu, K. Huang and S. Wu, *Journal of Advanced Oxidation Technologies*, 2016, **19**, 158-164.
22. Q. Yu, X. Li and M. Zhang, *Micro & Nano Letters*, 2014, **9**, 1-5.
23. L. Shi, L. Liang, F. Wang, J. Ma and J. Sun, *Catalysis Science & Technology*, 2014, **4**, 3235-3243.
24. J. Fu, J. Yu, C. Jiang and B. Cheng, *Advanced Energy Materials*, 2017.
25. S. Ye, R. Wang, M.-Z. Wu and Y.-P. Yuan, *Applied Surface Science*, 2015, **358**, 15-27.
26. G. Mamba and A. Mishra, *Applied Catalysis B: Environmental*, 2016, **198**, 347-377.
27. Y. Zheng, L. Lin, B. Wang and X. Wang, *Angewandte Chemie International Edition*, 2015, **54**, 12868-12884.
28. W.-J. Ong, L.-L. Tan, Y. H. Ng, S.-T. Yong and S.-P. Chai, *Chem. Rev*, 2016, **116**, 7159-7329.
29. X. Ma, Y. Lv, J. Xu, Y. Liu, R. Zhang and Y. Zhu, *The Journal of Physical Chemistry C*, 2012, **116**, 23485-23493.
30. G. Liu, P. Niu, C. Sun, S. C. Smith, Z. Chen, G. Q. Lu and H.-M. Cheng, *Journal of the American Chemical Society*, 2010, **132**, 11642-11648.
31. Y. Wang, H. Li, J. Yao, X. Wang and M. Antonietti, *Chemical Science*, 2011, **2**, 446-450.

32. J. Li, B. Shen, Z. Hong, B. Lin, B. Gao and Y. Chen, *Chemical Communications*, 2012, **48**, 12017-12019.
33. Y. Zhang, T. Mori, J. Ye and M. Antonietti, *Journal of the American Chemical Society*, 2010, **132**, 6294-6295.
34. Y. Zhou, L. Zhang, J. Liu, X. Fan, B. Wang, M. Wang, W. Ren, J. Wang, M. Li and J. Shi, *Journal of Materials Chemistry A*, 2015, **3**, 3862-3867.
35. F. Dong, Z. Zhao, T. Xiong, Z. Ni, W. Zhang, Y. Sun and W.-K. Ho, *ACS Applied Materials & Interfaces*, 2013, **5**, 11392-11401.
36. F. Dong, Z. Ni, P. Li and Z. Wu, *New Journal of Chemistry*, 2015, **39**, 4737-4744.
37. F. Goettmann, A. Fischer, M. Antonietti and A. Thomas, *Angewandte Chemie International Edition*, 2006, **45**, 4467-4471.
38. F. Su, S. C. Mathew, G. Lipner, X. Fu, M. Antonietti, S. Blechert and X. Wang, *Journal of the American Chemical Society*, 2010, **132**, 16299-16301.
39. Y.-P. Yuan, L.-S. Yin, S.-W. Cao, L.-N. Gu, G.-S. Xu, P. Du, H. Chai, Y.-S. Liao and C. Xue, *Green Chemistry*, 2014, **16**, 4663-4668.
40. M. J. Bojdys, J. O. Müller, M. Antonietti and A. Thomas, *Chemistry-A European Journal*, 2008, **14**, 8177-8182.
41. L. Xu, J. Xia, H. Xu, S. Yin, K. Wang, L. Huang, L. Wang and H. Li, *Journal of Power Sources*, 2014, **245**, 866-874.
42. J. Xu, L. Zhang, R. Shi and Y. Zhu, *Journal of Materials Chemistry A*, 2013, **1**, 14766-14772.
43. P. Niu, L. Zhang, G. Liu and H. M. Cheng, *Advanced Functional Materials*, 2012, **22**, 4763-4770.
44. P. Xia, B. Zhu, J. Yu, S. Cao and M. Jaroniec, *Journal of Materials Chemistry A*, 2017, **5**, 3230-3238.
45. S. Yang, Y. Gong, J. Zhang, L. Zhan, L. Ma, Z. Fang, R. Vajtai, X. Wang and P. M. Ajayan, *Advanced Materials*, 2013, **25**, 2452-2456.
46. G. Dong, K. Zhao and L. Zhang, *Chemical Communications*, 2012, **48**, 6178-6180.
47. X. Zhou, F. Peng, H. Wang, H. Yu and Y. Fang, *Chemical Communications*, 2011, **47**, 10323-10325.
48. Y. Wang, R. Shi, J. Lin and Y. Zhu, *Energy & Environmental Science*, 2011, **4**, 2922-2929.
49. C. Pan, J. Xu, Y. Wang, D. Li and Y. Zhu, *Advanced Functional Materials*, 2012, **22**, 1518-1524.
50. Y. Hou, A. B. Laursen, J. Zhang, G. Zhang, Y. Zhu, X. Wang, S. Dahl and I. Chorkendorff, *Angewandte Chemie International Edition*, 2013, **52**, 3621-3625.
51. M. Li, L. Zhang, M. Wu, Y. Du, X. Fan, M. Wang, L. Zhang, Q. Kong and J. Shi, *Nano Energy*, 2016, **19**, 145-155.
52. X. Bai, R. Zong, C. Li, D. Liu, Y. Liu and Y. Zhu, *Applied Catalysis B: Environmental*, 2014, **147**, 82-91.
53. Y. Di, X. Wang, A. Thomas and M. Antonietti, *ChemCatChem*, 2010, **2**, 834-838.
54. S. Samanta, S. Martha and K. Parida, *ChemCatChem*, 2014, **6**, 1453-1462.
55. R. Wang, L. Gu, J. Zhou, X. Liu, F. Teng, C. Li, Y. Shen and Y. Yuan, *Advanced Materials Interfaces*, 2015, **2**, 1500037-n/a.
56. H. Wang, X. Yuan, Y. Wu, G. Zeng, X. Chen, L. Leng and H. Li, *Applied Catalysis B: Environmental*, 2015, **174**, 445-454.
57. F. He, G. Chen, Y. Zhou, Y. Yu, L. Li, S. Hao and B. Liu, *Journal of Materials Chemistry A*, 2016, **4**, 3822-3827.
58. Q. Su, J. Sun, J. Wang, Z. Yang, W. Cheng and S. Zhang, *Catalysis Science & Technology*, 2014, **4**, 1556-1562.
59. J. Zhu, P. Xiao, H. Li and S. n. A. Carabineiro, *ACS applied materials & interfaces*, 2014, **6**, 16449-16465.
60. J. Zhang, X. Chen, K. Takanabe, K. Maeda, K. Domen, J. D. Epping, X. Fu, M. Antonietti and X. Wang, *Angewandte Chemie International Edition*, 2010, **49**, 441-444.

61. Y. Zhang, J. Liu, G. Wu and W. Chen, *Nanoscale*, 2012, **4**, 5300-5303.
62. H.-J. Li, B.-W. Sun, L. Sui, D.-J. Qian and M. Chen, *Physical Chemistry Chemical Physics*, 2015, **17**, 3309-3315.
63. Y. Zhang, H. Zhang, L. Cheng, Y. Wang, Y. Miao, G. Ding and Z. Jiao, *RSC Advances*, 2016, **6**, 14002-14008.
64. Y. Yu, Q. Zhou and J. Wang, *Chemical Communications*, 2016, **52**, 3396-3399.
65. B. Jürgens, E. Irran, J. Senker, P. Kroll, H. Müller and W. Schnick, *Journal of the American Chemical Society*, 2003, **125**, 10288-10300.
66. B. Zhu, P. Xia, W. Ho and J. Yu, *Applied Surface Science*, 2015, **344**, 188-195.
67. K. Wang, Q. Li, B. Liu, B. Cheng, W. Ho and J. Yu, *Applied Catalysis B: Environmental*, 2015, **176**, 44-52.
68. C. Yang, B. Wang, L. Zhang, L. Yin and X. Wang, *Angewandte Chemie*, 2017, **129**, 6727-6731.
69. X.-H. Li, X. Wang and M. Antonietti, *Chemical Science*, 2012, **3**, 2170-2174.
70. J. Sun, J. Zhang, M. Zhang, M. Antonietti, X. Fu and X. Wang, *Nature Communications*, 2012, **3**, 1139.
71. X.-H. Li, J. Zhang, X. Chen, A. Fischer, A. Thomas, M. Antonietti and X. Wang, *Chemistry of Materials*, 2011, **23**, 4344-4348.
72. J. Liu, J. Huang, D. Dontosova and M. Antonietti, *RSC Advances*, 2013, **3**, 22988-22993.
73. S. Wang, C. Li, T. Wang, P. Zhang, A. Li and J. Gong, *Journal of Materials Chemistry A*, 2014, **2**, 2885-2890.
74. H. Zhao, H. Yu, X. Quan, S. Chen, Y. Zhang, H. Zhao and H. Wang, *Applied Catalysis B: Environmental*, 2014, **152**, 46-50.
75. K. S. Lakhi, D.-H. Park, K. Al-Bahily, W. Cha, B. Viswanathan, J.-H. Choy and A. Vinu, *Chemical Society Reviews*, 2017, **46**, 72-101.
76. X. Bai, L. Wang, R. Zong and Y. Zhu, *The Journal of Physical Chemistry C*, 2013, **117**, 9952-9961.
77. M. Tahir, C. Cao, N. Mahmood, F. K. Butt, A. Mahmood, F. Idrees, S. Hussain, M. Tanveer, Z. Ali and I. Aslam, *ACS applied materials & interfaces*, 2013, **6**, 1258-1265.
78. W. Wang, C. Y. Jimmy, Z. Shen, D. K. L. Chan and T. Gu, *Chemical Communications*, 2014, **50**, 10148-10150.
79. Y. Yin, J. Han, X. Zhang, Y. Zhang, J. Zhou, D. Muir, R. Sutarto, Z. Zhang, S. Liu and B. Song, *RSC Advances*, 2014, **4**, 32690-32697.
80. L. Ma, H. Fan, M. Li, H. Tian, J. Fang and G. Dong, *Journal of Materials Chemistry A*, 2015, **3**, 22404-22412.
81. H. Xu, J. Yan, X. She, L. Xu, J. Xia, Y. Xu, Y. Song, L. Huang and H. Li, *Nanoscale*, 2014, **6**, 1406-1415.
82. Q. Han, B. Wang, J. Gao, Z. Cheng, Y. Zhao, Z. Zhang and L. Qu, *ACS nano*, 2016, **10**, 2745-2751.
83. L. Ma, H. Fan, J. Wang, Y. Zhao, H. Tian and G. Dong, *Applied Catalysis B: Environmental*, 2016, **190**, 93-102.
84. F. Cheng, H. Wang and X. Dong, *Chemical communications*, 2015, **51**, 7176-7179.
85. J. Tong, L. Zhang, F. Li, K. Wang, L. Han and S. Cao, *RSC Advances*, 2015, **5**, 88149-88153.
86. P. Qiu, H. Chen, C. Xu, N. Zhou, F. Jiang, X. Wang and Y. Fu, *Journal of Materials Chemistry A*, 2015, **3**, 24237-24244.
87. J. Zhu, Y. Wei, W. Chen, Z. Zhao and A. Thomas, *Chemical Communications*, 2010, **46**, 6965-6967.
88. P. Sharma and Y. Sasson, *RSC Advances*, 2017, **7**, 25589-25596.
89. J. Xu, K. Shen, B. Xue and Y.-X. Li, *Journal of Molecular Catalysis A: Chemical*, 2013, **372**, 105-113.
90. H. Wang, C. Wang, Y. Yang, M. Zhao and Y. Wang, *Catalysis Science & Technology*, 2017, **7**, 405-417.

91. Y. Shiraishi, S. Kanazawa, Y. Sugano, D. Tsukamoto, H. Sakamoto, S. Ichikawa and T. Hirai, *Acs Catalysis*, 2014, **4**, 774-780.
92. Y. Dai, C. Li, Y. Shen, T. Lim, J. Xu, Y. Li, H. Niemantsverdriet, F. Besenbacher, N. Lock and R. Su, *Nature communications*, 2018, **9**, 60.
93. M. A. Khan, I. F. Teixeira, M. M. J. Li, Y. Koito and S. C. E. Tsang, *Chemical Communications*, 2016, **52**, 2772-2775.
94. Z. Lin and X. Wang, *Angewandte Chemie International Edition*, 2013, **52**, 1735-1738.
95. Y. Wang, J. Zhang, X. Wang, M. Antonietti and H. Li, *Angewandte Chemie International Edition*, 2010, **49**, 3356-3359.
96. S. C. Yan, Z. S. Li and Z. G. Zou, *Langmuir*, 2010, **26**, 3894-3901.
97. D.-H. Lan, H.-T. Wang, L. Chen, C.-T. Au and S.-F. Yin, *Carbon*, 2016, **100**, 81-89.
98. J. Hong, X. Xia, Y. Wang and R. Xu, *Journal of Materials Chemistry*, 2012, **22**, 15006-15012.
99. G. Zhang, M. Zhang, X. Ye, X. Qiu, S. Lin and X. Wang, *Advanced Materials*, 2014, **26**, 805-809.
100. Q. Han, C. Hu, F. Zhao, Z. Zhang, N. Chen and L. Qu, *Journal of Materials Chemistry A*, 2015, **3**, 4612-4619.
101. X. Wang, X. Chen, A. Thomas, X. Fu and M. Antonietti, *Advanced Materials*, 2009, **21**, 1609-1612.
102. Z. Ding, X. Chen, M. Antonietti and X. Wang, *ChemSusChem*, 2011, **4**, 274-281.
103. S. Hu, X. Qu, P. Li, F. Wang, Q. Li, L. Song, Y. Zhao and X. Kang, *Chemical Engineering Journal*, 2018, **334**, 410-418.
104. S. Hu, F. Li, Z. Fan, F. Wang, Y. Zhao and Z. Lv, *Dalton Transactions*, 2015, **44**, 1084-1092.
105. J. Zhang, S. Hu and Y. Wang, *RSC Advances*, 2014, **4**, 62912-62919.
106. H. Gao, S. Yan, J. Wang and Z. Zou, *Dalton Transactions*, 2014, **43**, 8178-8183.
107. J. Zhao, L. Ma, H. Wang, Y. Zhao, J. Zhang and S. Hu, *Applied Surface Science*, 2015, **332**, 625-630.
108. T. Xiong, W. Cen, Y. Zhang and F. Dong, *Acs Catalysis*, 2016, **6**, 2462-2472.
109. Z. Zhou, Y. Zhang, Y. Shen, S. Liu and Y. Zhang, *Chemical Society Reviews*, 2018, **47**, 2298-2321.
110. L. Jiang, X. Yuan, Y. Pan, J. Liang, G. Zeng, Z. Wu and H. Wang, *Applied Catalysis B: Environmental*, 2017, **217**, 388-406.
111. S. C. Yan, S. B. Lv, Z. S. Li and Z. G. Zou, *Dalton Transactions*, 2010, **39**, 1488-1491.
112. X. Dong and F. Cheng, *Journal of Materials Chemistry A*, 2015, **3**, 23642-23652.
113. Y. Zhang and M. Antonietti, *Chemistry–An Asian Journal*, 2010, **5**, 1307-1311.
114. S. Zhang, J. Li, X. Wang, Y. Huang, M. Zeng and J. Xu, *Journal of Materials Chemistry A*, 2015, **3**, 10119-10126.
115. A. K. Geim and K. S. Novoselov, *Nature materials*, 2007, **6**, 183.
116. A. K. Geim, *science*, 2009, **324**, 1530-1534.
117. Z. Zhao, Y. Sun and F. Dong, *Nanoscale*, 2015, **7**, 15-37.
118. Y. Sun, C. Li, Y. Xu, H. Bai, Z. Yao and G. Shi, *Chemical Communications*, 2010, **46**, 4740-4742.
119. Q. Xiang, J. Yu and M. Jaroniec, *The Journal of Physical Chemistry C*, 2011, **115**, 7355-7363.
120. Y. Li, H. Zhang, P. Liu, D. Wang, Y. Li and H. Zhao, *Small*, 2013, **9**, 3336-3344.
121. W.-J. Ong, L.-L. Tan, S.-P. Chai, S.-T. Yong and A. R. Mohamed, *Nano Energy*, 2015, **13**, 757-770.
122. L. Ge and C. Han, *Applied Catalysis B: Environmental*, 2012, **117**, 268-274.
123. Y. Xu, H. Xu, L. Wang, J. Yan, H. Li, Y. Song, L. Huang and G. Cai, *Dalton Transactions*, 2013, **42**, 7604-7613.
124. B. Chai, X. Liao, F. Song and H. Zhou, *Dalton Transactions*, 2014, **43**, 982-989.
125. X. Bai, L. Wang, Y. Wang, W. Yao and Y. Zhu, *Applied Catalysis B: Environmental*, 2014, **152**, 262-270.
126. Y. Guo, P. Yao, D. Zhu and C. Gu, *Journal of Materials Chemistry A*, 2015, **3**, 13189-13192.

127. H. Zhang, L. Zhao, F. Geng, L.-H. Guo, B. Wan and Y. Yang, *Applied Catalysis B: Environmental*, 2016, **180**, 656-662.
128. J. Liu, Y. Liu, N. Liu, Y. Han, X. Zhang, H. Huang, Y. Lifshitz, S. T. Lee, J. Zhong and Z. Kang, *Science*, 2015, **347**, 970-974.
129. S. Fang, Y. Xia, K. Lv, Q. Li, J. Sun and M. Li, *Applied Catalysis B: Environmental*, 2016, **185**, 225-232.
130. G. Gao, Y. Jiao, F. Ma, Y. Jiao, E. Waclawik and A. Du, *Physical Chemistry Chemical Physics*, 2015, **17**, 31140-31144.
131. X. Jian, X. Liu, H.-m. Yang, J.-g. Li, X.-l. Song, H.-y. Dai and Z.-h. Liang, *Applied Surface Science*, 2016, **370**, 514-521.
132. L. Ge, C. Han and J. Liu, *Journal of Materials Chemistry*, 2012, **22**, 11843-11850.
133. Y. Sui, J. Liu, Y. Zhang, X. Tian and W. Chen, *Nanoscale*, 2013, **5**, 9150-9155.
134. H. Yan and Y. Huang, *Chemical communications*, 2011, **47**, 4168-4170.
135. Z. Xing, Z. Chen, X. Zong and L. Wang, *Chemical Communications*, 2014, **50**, 6762-6764.
136. S. Hu, L. Ma, H. Wang, L. Zhang, Y. Zhao and G. Wu, *RSC Advances*, 2015, **5**, 31947-31953.
137. F. He, G. Chen, Y. Yu, S. Hao, Y. Zhou and Y. Zheng, *ACS applied materials & interfaces*, 2014, **6**, 7171-7179.
138. X. Xia, N. Deng, G. Cui, J. Xie, X. Shi, Y. Zhao, Q. Wang, W. Wang and B. Tang, *Chemical communications*, 2015, **51**, 10899-10902.
139. J. Zhang, M. Zhang, R. Q. Sun and X. Wang, *Angewandte Chemie*, 2012, **124**, 10292-10296.
140. L. Ye, D. Wang and S. Chen, *ACS applied materials & interfaces*, 2016, **8**, 5280-5289.
141. S. Samanta, S. Khilari, D. Pradhan and R. Srivastava, *ACS Sustainable Chemistry & Engineering*, 2017, **5**, 2562-2577.
142. J. Yu, S. Wang, J. Low and W. Xiao, *Physical Chemistry Chemical Physics*, 2013, **15**, 16883-16890.
143. Z. Jiang, C. Zhu, W. Wan, K. Qian and J. Xie, *Journal of Materials Chemistry A*, 2016, **4**, 1806-1818.
144. Q. Sun, K. Lv, Z. Zhang, M. Li and B. Li, *Applied Catalysis B: Environmental*, 2015, **164**, 420-427.
145. M. J. Muñoz-Batista, A. Kubacka and M. Fernandez-Garcia, *Catalysis Science & Technology*, 2014, **4**, 2006-2015.
146. C. Han, Y. Wang, Y. Lei, B. Wang, N. Wu, Q. Shi and Q. Li, *Nano Research*, 2015, **8**, 1199-1209.
147. K. Sridharan, E. Jang and T. J. Park, *Applied Catalysis B: Environmental*, 2013, **142**, 718-728.
148. K. Yang, C. Meng, L. Lin, X. Peng, X. Chen, X. Wang, W. Dai and X. Fu, *Catalysis Science & Technology*, 2016, **6**, 829-839.
149. G. Li, X. Nie, J. Chen, Q. Jiang, T. An, P. K. Wong, H. Zhang, H. Zhao and H. Yamashita, *Water research*, 2015, **86**, 17-24.
150. W. Li, C. Li, B. Chen, X. Jiao and D. Chen, *RSC Advances*, 2015, **5**, 34281-34291.
151. X. Chen, J. Wei, R. Hou, Y. Liang, Z. Xie, Y. Zhu, X. Zhang and H. Wang, *Applied Catalysis B: Environmental*, 2016, **188**, 342-350.
152. R. Hao, G. Wang, H. Tang, L. Sun, C. Xu and D. Han, *Applied Catalysis B: Environmental*, 2016, **187**, 47-58.
153. K. Li, Z. Zeng, L. Yan, M. Huo, Y. Guo, S. Luo and X. Luo, *Applied Catalysis B: Environmental*, 2016, **187**, 269-280.
154. Y. Li, J. Wang, Y. Yang, Y. Zhang, D. He, Q. An and G. Cao, *Journal of hazardous materials*, 2015, **292**, 79-89.
155. J. Yan, H. Wu, H. Chen, Y. Zhang, F. Zhang and S. F. Liu, *Applied Catalysis B: Environmental*, 2016, **191**, 130-137.
156. H. Li, L. Zhou, L. Wang, Y. Liu, J. Lei and J. Zhang, *Physical Chemistry Chemical Physics*, 2015, **17**, 17406-17412.

157. K. Dai, L. Lu, C. Liang, Q. Liu and G. Zhu, *Applied Catalysis B: Environmental*, 2014, **156**, 331-340.
158. D. Lu, G. Zhang and Z. Wan, *Applied Surface Science*, 2015, **358**, 223-230.
159. X. Song, Y. Hu, M. Zheng and C. Wei, *Applied Catalysis B: Environmental*, 2016, **182**, 587-597.
160. H. Chen, Y. Xie, X. Sun, M. Lv, F. Wu, L. Zhang, L. Li and X. Xu, *Dalton Transactions*, 2015, **44**, 13030-13039.
161. L. Zhang, D. Jing, X. She, H. Liu, D. Yang, Y. Lu, J. Li, Z. Zheng and L. Guo, *Journal of Materials Chemistry A*, 2014, **2**, 2071-2078.
162. Y. Zang, L. Li, Y. Xu, Y. Zuo and G. Li, *Journal of Materials Chemistry A*, 2014, **2**, 15774-15780.
163. D. Chen, K. Wang, T. Ren, H. Ding and Y. Zhu, *Dalton Transactions*, 2014, **43**, 13105-13114.
164. J.-X. Sun, Y.-P. Yuan, L.-G. Qiu, X. Jiang, A.-J. Xie, Y.-H. Shen and J.-F. Zhu, *Dalton Transactions*, 2012, **41**, 6756-6763.
165. J. Li, M. Zhou, Z. Ye, H. Wang, C. Ma, P. Huo and Y. Yan, *RSC Advances*, 2015, **5**, 91177-91189.
166. W. Liu, M. Wang, C. Xu and S. Chen, *Chemical Engineering Journal*, 2012, **209**, 386-393.
167. S. Kumar, A. Baruah, S. Tonda, B. Kumar, V. Shanker and B. Sreedhar, *Nanoscale*, 2014, **6**, 4830-4842.
168. K.-i. Katsumata, R. Motoyoshi, N. Matsushita and K. Okada, *Journal of hazardous materials*, 2013, **260**, 475-482.
169. L. Huang, H. Xu, Y. Li, H. Li, X. Cheng, J. Xia, Y. Xu and G. Cai, *Dalton Transactions*, 2013, **42**, 8606-8616.
170. J. Ding, Q. Liu, Z. Zhang, X. Liu, J. Zhao, S. Cheng, B. Zong and W.-L. Dai, *Applied Catalysis B: Environmental*, 2015, **165**, 511-518.
171. J. Chen, S. Shen, P. Guo, M. Wang, P. Wu, X. Wang and L. Guo, *Applied Catalysis B: Environmental*, 2014, **152**, 335-341.
172. S. Ye, L.-G. Qiu, Y.-P. Yuan, Y.-J. Zhu, J. Xia and J.-F. Zhu, *Journal of Materials Chemistry A*, 2013, **1**, 3008-3015.
173. J. Zhang, M. Grzelczak, Y. Hou, K. Maeda, K. Domen, X. Fu, M. Antonietti and X. Wang, *Chemical Science*, 2012, **3**, 443-446.
174. L. Ge, C. Han and J. Liu, *Applied Catalysis B: Environmental*, 2011, **108**, 100-107.
175. J. Ran, J. Yu and M. Jaroniec, *Green Chemistry*, 2011, **13**, 2708-2713.
176. X. Dai, M. Xie, S. Meng, X. Fu and S. Chen, *Applied Catalysis B: Environmental*, 2014, **158**, 382-390.
177. H. Yu, F. Chen, F. Chen and X. Wang, *Applied Surface Science*, 2015, **358**, 385-392.
178. J. Fu, B. Chang, Y. Tian, F. Xi and X. Dong, *Journal of Materials Chemistry A*, 2013, **1**, 3083-3090.
179. M. Lu, Z. Pei, S. Weng, W. Feng, Z. Fang, Z. Zheng, M. Huang and P. Liu, *Physical Chemistry Chemical Physics*, 2014, **16**, 21280-21288.
180. J. Zhang, Y. Wang, J. Jin, J. Zhang, Z. Lin, F. Huang and J. Yu, *ACS applied materials & interfaces*, 2013, **5**, 10317-10324.
181. J. Xie, H. Zhang, S. Li, R. Wang, X. Sun, M. Zhou, J. Zhou, X. W. D. Lou and Y. Xie, *Advanced materials*, 2013, **25**, 5807-5813.
182. H. Zhao, Y. Dong, P. Jiang, H. Miao, G. Wang and J. Zhang, *Journal of Materials Chemistry A*, 2015, **3**, 7375-7381.
183. H. Tian, M. Liu and W. Zheng, *Applied Catalysis B: Environmental*, 2018, **225**, 468-476.
184. J. Wang, Z. Guan, J. Huang, Q. Li and J. Yang, *Journal of Materials Chemistry A*, 2014, **2**, 7960-7966.
185. Y. Hou, Y. Zhu, Y. Xu and X. Wang, *Applied Catalysis B: Environmental*, 2014, **156**, 122-127.
186. Z. Zhang, J. Huang, M. Zhang, Q. Yuan and B. Dong, *Applied Catalysis B: Environmental*, 2015, **163**, 298-305.
187. L. Yin, Y.-P. Yuan, S.-W. Cao, Z. Zhang and C. Xue, *Rsc Advances*, 2014, **4**, 6127-6132.

188. Y. Zhu, Y. Xu, Y. Hou, Z. Ding and X. Wang, *International Journal of Hydrogen Energy*, 2014, **39**, 11873-11879.
189. Y. Shi, S. Jiang, K. Zhou, B. Wang, B. Wang, Z. Gui, Y. Hu and R. K. K. Yuen, *RSC Advances*, 2014, **4**, 2609-2613.
190. P. Suyana, K. R. Sneha, B. N. Nair, V. Karunakaran, A. P. Mohamed, K. G. K. Warrier and U. S. Hareesh, *RSC Advances*, 2016, **6**, 17800-17809.
191. J. Wang, P. Guo, Q. Guo, P. G. Jönsson and Z. Zhao, *CrystEngComm*, 2014, **16**, 4485-4492.
192. D. Jiang, L. Chen, J. Xie and M. Chen, *Dalton Transactions*, 2014, **43**, 4878-4885.
193. A. Dhakshinamoorthy, A. M. Asiri and H. García, *Angewandte Chemie International Edition*, 2016, **55**, 5414-5445.
194. R. Chen, J. Zhang, Y. Wang, X. Chen, J. A. Zapien and C.-S. Lee, *Nanoscale*, 2015, **7**, 17299-17305.
195. J. Hong, C. Chen, F. E. Bedoya, G. H. Kelsall, D. O'Hare and C. Petit, *Catalysis Science & Technology*, 2016, **6**, 5042-5051.
196. R. Jiang, B. Li, C. Fang and J. Wang, *Advanced materials*, 2014, **26**, 5274-5309.
197. C. M. Cobley, S. E. Skrabalak, D. J. Campbell and Y. Xia, *Plasmonics*, 2009, **4**, 171-179.
198. M. Hu, J. Chen, Z.-Y. Li, L. Au, G. V. Hartland, X. Li, M. Marquez and Y. Xia, *Chemical Society Reviews*, 2006, **35**, 1084-1094.
199. M. Rycenga, C. M. Cobley, J. Zeng, W. Li, C. H. Moran, Q. Zhang, D. Qin and Y. Xia, *Chemical reviews*, 2011, **111**, 3669-3712.
200. Y. Xia and N. J. Halas, *MRS bulletin*, 2005, **30**, 338-348.
201. H. A. Atwater and A. Polman, *Nature materials*, 2010, **9**, 205.
202. J. N. Anker, W. P. Hall, O. Lyandres, N. C. Shah, J. Zhao and R. P. Van Duyne, *Nature materials*, 2008, **7**, 442.
203. W. Hou and S. B. Cronin, *Advanced Functional Materials*, 2013, **23**, 1612-1619.
204. S. Linic, P. Christopher and D. B. Ingram, *Nature materials*, 2011, **10**, 911.
205. W. A. Murray and W. L. Barnes, *Advanced materials*, 2007, **19**, 3771-3782.
206. K. A. Willets and R. P. Van Duyne, *Annu. Rev. Phys. Chem.*, 2007, **58**, 267-297.
207. Y. Huang, Z. Liu, G. Gao, G. Xiao, A. Du, S. Bottle, S. Sarina and H. Zhu, *ACS Catalysis*, 2017, **7**, 4975-4985.
208. P. A. DeSario, J. J. Pietron, T. H. Brintlinger, M. McEntee, J. F. Parker, O. Baturina, R. M. Stroud and D. R. Rolison, *Nanoscale*, 2017, **9**, 11720-11729.
209. T. V. Alves, W. Hermoso, F. R. Ornellas and P. H. C. Camargo, *Chemical Physics Letters*, 2012, **544**, 64-69.
210. J. M. McMahon, G. C. Schatz and S. K. Gray, *Physical Chemistry Chemical Physics*, 2013, **15**, 5415-5423.
211. B. Clark, C. R. Jacobson, M. Lou, J. Yang, L. Zhou, S. Gottheim, P. Nordlander, N. J. Halas and C. J. DeSantis, *Nano letters*, 2017.
212. M.-N. Su, P. D. Dongare, D. Chakraborty, Y. Zhang, C. Yi, F. Wen, W.-S. Chang, P. Nordlander, J. E. Sader and N. J. Halas, *Nano letters*, 2017, **17**, 2575-2583.
213. M. W. Knight, N. S. King, L. Liu, H. O. Everitt, P. Nordlander and N. J. Halas, *ACS nano*, 2013, **8**, 834-840.
214. M. J. McClain, A. E. Schlather, E. Ringe, N. S. King, L. Liu, A. Manjavacas, M. W. Knight, I. Kumar, K. H. Whitmire, H. O. Everitt, P. Nordlander and N. J. Halas, *Nano letters*, 2015, **15**, 2751-2755.
215. T. Tumkur, X. Yang, C. Zhang, J. Yang, Y. Zhang, G. V. Naik, P. Nordlander and N. J. Halas, *Nano Letters*, 2018, **18**, 2040-2046.
216. M. L. Tseng, J. Yang, M. Semmlinger, C. Zhang, P. Nordlander and N. J. Halas, *Nano Letters*, 2017, **17**, 6034-6039.
217. S. Linic, U. Aslam, C. Boerigter and M. Morabito, *Nature materials*, 2015, **14**, 567.
218. E. Hao and G. C. Schatz, *The Journal of chemical physics*, 2004, **120**, 357-366.

219. P. Christopher, H. Xin, A. Marimuthu and S. Linic, *Nature materials*, 2012, **11**, 1044.
220. D. B. Ingram, P. Christopher, J. L. Bauer and S. Linic, *ACS Catalysis*, 2011, **1**, 1441-1447.
221. P. Christopher, H. Xin and S. Linic, *Nat Chem*, 2011, **3**, 467-472.
222. D. B. Ingram and S. Linic, *Journal of the American Chemical Society*, 2011, **133**, 5202-5205.
223. G. Baffou and R. Quidant, *Chemical Society Reviews*, 2014, **43**, 3898-3907.
224. C. E. Talley, J. B. Jackson, C. Oubre, N. K. Grady, C. W. Hollars, S. M. Lane, T. R. Huser, P. Nordlander and N. J. Halas, *Nano letters*, 2005, **5**, 1569-1574.
225. M. J. Kale, T. Avanesian and P. Christopher, *Acs Catalysis*, 2013, **4**, 116-128.
226. M. J. Kale, T. Avanesian, H. Xin, J. Yan and P. Christopher, *Nano letters*, 2014, **14**, 5405-5412.
227. J. W. Gadzuk, *The Journal of chemical physics*, 1983, **79**, 6341-6348.
228. M. L. Brongersma, N. J. Halas and P. Nordlander, *Nature nanotechnology*, 2015, **10**, 25.
229. E. Boisselier and D. Astruc, *Chemical society reviews*, 2009, **38**, 1759-1782.
230. B. Pelaz, C. Alexiou, R. A. Alvarez-Puebla, F. Alves, A. M. Andrews, S. Ashraf, L. P. Balogh, L. Ballerini, A. Bestetti and C. Brendel, *Journal*, 2017.
231. F. Meng, W. Hao, S. Yu, R. Feng, Y. Liu, F. Yu, P. Tao, W. Shang, J. Wu and C. Song, *Journal of the American Chemical Society*, 2017, **139**, 12362-12365.
232. L. Cao, D. N. Barsic, A. R. Guichard and M. L. Brongersma, *Nano letters*, 2007, **7**, 3523-3527.
233. L. Zhou, Y. Tan, J. Wang, W. Xu, Y. Yuan, W. Cai, S. Zhu and J. Zhu, *Nature Photonics*, 2016, **10**, 393.
234. C. Wadell, T. J. Antosiewicz and C. Langhammer, *Nano letters*, 2012, **12**, 4784-4790.
235. B. Hammer and J. K. Norskov, *Nature*, 1995, **376**, 238.
236. S. Murphy, L. Huang and P. V. Kamat, *The Journal of Physical Chemistry C*, 2013, **117**, 4740-4747.
237. B. Sharma, R. R. Frontiera, A.-I. Henry, E. Ringe and R. P. Van Duyne, *Materials today*, 2012, **15**, 16-25.
238. J. Wang, R. A. Ando and P. H. C. Camargo, *Angewandte Chemie*, 2015, **127**, 7013-7016.
239. D. Tsukamoto, Y. Shiraishi, Y. Sugano, S. Ichikawa, S. Tanaka and T. Hirai, *Journal of the American Chemical Society*, 2012, **134**, 6309-6315.
240. Z. Zhang and J. T. Yates Jr, *Chemical reviews*, 2012, **112**, 5520-5551.
241. U. Banin, Y. Ben-Shahar and K. Vinokurov, *Chemistry of Materials*, 2013, **26**, 97-110.
242. P. D. Cozzoli, R. Comparelli, E. Fanizza, M. L. Curri, A. Agostiano and D. Laub, *Journal of the American Chemical Society*, 2004, **126**, 3868-3879.
243. Y. Zheng, L. Zheng, Y. Zhan, X. Lin, Q. Zheng and K. Wei, *Inorganic chemistry*, 2007, **46**, 6980-6986.
244. C. Gu, C. Cheng, H. Huang, T. Wong, N. Wang and T.-Y. Zhang, *Crystal Growth and Design*, 2009, **9**, 3278-3285.
245. C. K. N. Peh, L. Ke and G. W. Ho, *Materials Letters*, 2010, **64**, 1372-1375.
246. H. Zhu, E. Zhu, G. Ou, L. Gao and J. Chen, *Nanoscale research letters*, 2010, **5**, 1755.
247. C. George, A. Genovese, F. Qiao, K. Korobchevskaya, A. Comin, A. Falqui, S. Marras, A. Roig, Y. Zhang and R. Krahne, *Nanoscale*, 2011, **3**, 4647-4654.
248. T. C. Damato, C. C. S. de Oliveira, R. A. Ando and P. H. C. Camargo, *Langmuir*, 2013, **29**, 1642-1649.
249. F. V. E. dos Reis, V. S. Antonin, P. Hammer, M. C. Santos and P. H. C. Camargo, *Journal of Catalysis*, 2015, **326**, 100-106.
250. E. C. M. Barbosa, J. L. Fiorio, T. Mou, B. Wang, L. M. Rossi and P. Camargo, *Chemistry-A European Journal*, 2018.
251. X.-F. Wu, H.-Y. Song, J.-M. Yoon, Y.-T. Yu and Y.-F. Chen, *Langmuir*, 2009, **25**, 6438-6447.
252. L. Zhang, D. A. Blom and H. Wang, *Chemistry of Materials*, 2011, **23**, 4587-4598.
253. N. Zhang, S. Liu, X. Fu and Y.-J. Xu, *The Journal of Physical Chemistry C*, 2011, **115**, 9136-9145.

254. P. Ramasamy, D.-M. Seo, S.-H. Kim and J. Kim, *Journal of Materials Chemistry*, 2012, **22**, 11651-11657.
255. P. Du, P. Jing, D. Li, Y. Cao, Z. Liu and Z. Sun, *Small*, 2015, **11**, 2454-2462.
256. C.-H. Kuo, T.-E. Hua and M. H. Huang, *Journal of the American Chemical Society*, 2009, **131**, 17871-17878.
257. M. Fan, C. Song, T. Chen, X. Yan, D. Xu, W. Gu, W. Shi and L. Xiao, *RSC Advances*, 2016, **6**, 34633-34640.
258. S. Ma, S. Zhan, Y. Jia, Q. Shi and Q. Zhou, *Applied Catalysis B: Environmental*, 2016, **186**, 77-87.
259. Y. Zhang, D. A. J. M. Ligthart, X.-Y. Quek, L. Gao and E. J. M. Hensen, *International Journal of Hydrogen Energy*, 2014, **39**, 11537-11546.
260. F. Fina, H. Menard and J. T. S. Irvine, *Physical Chemistry Chemical Physics*, 2015, **17**, 13929-13936.
261. J. Liu, Y. Zhang, L. Lu, G. Wu and W. Chen, *Chemical Communications*, 2012, **48**, 8826-8828.
262. Y. Guo, L. Zhang, K. Zhou, Y. Shen, Q. Zhang and C. Gu, *Journal of Materials Chemistry A*, 2014, **2**, 19594-19597.
263. J. Liu, Y. Yang, N. Liu, Y. Liu, H. Huang and Z. Kang, *Green Chemistry*, 2014, **16**, 4559-4565.
264. N. Cheng, J. Tian, Q. Liu, C. Ge, A. H. Qusti, A. M. Asiri, A. O. Al-Youbi and X. Sun, *ACS applied materials & interfaces*, 2013, **5**, 6815-6819.
265. T. Bhowmik, M. K. Kundu and S. Barman, *RSC Advances*, 2015, **5**, 38760-38773.
266. S. Tonda, S. Kumar and V. Shanker, *Materials Research Bulletin*, 2016, **75**, 51-58.
267. O. Fontelles-Carceller, M. J. Muñoz-Batista, M. Fernández-García and A. Kubacka, *ACS applied materials & interfaces*, 2016, **8**, 2617-2627.
268. Y. Bu, Z. Chen and W. Li, *Applied Catalysis B: Environmental*, 2014, **144**, 622-630.
269. J. Chen, C. L. Dong, Y. Du, D. Zhao and S. Shen, *Advanced Materials Interfaces*, 2015, **2**.
270. M. J. Munoz-Batista, O. Fontelles-Carceller, M. Ferrer, M. Fernández-García and A. Kubacka, *Applied Catalysis B: Environmental*, 2016, **183**, 86-95.
271. W. Bing, Z. Chen, H. Sun, P. Shi, N. Gao, J. Ren and X. Qu, *Nano Research*, 2015, **8**, 1648-1658.
272. L. Ge, C. Han, J. Liu and Y. Li, *Applied Catalysis A: General*, 2011, **409**, 215-222.
273. Y. Yang, Y. Guo, F. Liu, X. Yuan, Y. Guo, S. Zhang, W. Guo and M. Huo, *Applied Catalysis B: Environmental*, 2013, **142**, 828-837.
274. S. Patnaik, D. P. Sahoo and K. Parida, *Renewable and Sustainable Energy Reviews*, 2018, **82**, 1297-1312.
275. Y. Shiraishi, Y. Kofuji, S. Kanazawa, H. Sakamoto, S. Ichikawa, S. Tanaka and T. Hirai, *Chemical communications*, 2014, **50**, 15255-15258.
276. K. Li, Z. Zeng, L. Yan, S. Luo, X. Luo, M. Huo and Y. Guo, *Applied Catalysis B: Environmental*, 2015, **165**, 428-437.
277. W.-J. Ong, L.-L. Tan, S.-P. Chai and S.-T. Yong, *Dalton Transactions*, 2015, **44**, 1249-1257.
278. J. Yu, K. Wang, W. Xiao and B. Cheng, *Physical Chemistry Chemical Physics*, 2014, **16**, 11492-11501.
279. Y. Wang, D. Cao, M. Liu and X. Zhao, *Catalysis Communications*, 2017, **102**, 85-88.
280. Z. Li, R. Lin, Z. Liu, D. Li, H. Wang and Q. Li, *Electrochimica Acta*, 2016, **191**, 606-615.
281. H. Qian, H. Huang and X. Wang, *Journal of Power Sources*, 2015, **275**, 734-741.
282. S. Verma, R. B. Nasir Baig, M. N. Nadagouda and R. S. Varma, *Catalysis Today*, 2017.
283. S. Bai, X. Wang, C. Hu, M. Xie, J. Jiang and Y. Xiong, *Chemical communications*, 2014, **50**, 6094-6097.
284. C. Chang, Y. Fu, M. Hu, C. Wang, G. Shan and L. Zhu, *Applied Catalysis B: Environmental*, 2013, **142**, 553-560.
285. F. Dong, Z. Zhao, Y. Sun, Y. Zhang, S. Yan and Z. Wu, *Environmental science & technology*, 2015, **49**, 12432-12440.

286. P. Zhang, T. Wang and H. Zeng, *Applied Surface Science*, 2017, **391**, 404-414.
287. N. Wang, Z. Han, H. Fan and S. Ai, *RSC Advances*, 2015, **5**, 91302-91307.
288. X. Zhou, Z. Luo, P. Tao, B. Jin, Z. Wu and Y. Huang, *Materials Chemistry and Physics*, 2014, **143**, 1462-1468.
289. Z. Li, C. Kong and G. Lu, *The Journal of Physical Chemistry C*, 2015, **120**, 56-63.
290. L. Bi, D. Xu, L. Zhang, Y. Lin, D. Wang and T. Xie, *Physical Chemistry Chemical Physics*, 2015, **17**, 29899-29905.
291. L. Kong, Y. Dong, P. Jiang, G. Wang, H. Zhang and N. Zhao, *Journal of Materials Chemistry A*, 2016, **4**, 9998-10007.
292. J. Wen, J. Xie, H. Zhang, A. Zhang, Y. Liu, X. Chen and X. Li, *ACS Applied Materials & Interfaces*, 2017, **9**, 14031-14042.
293. C. H. Choi, L. Lin, S. Gim, S. Lee, H. Kim, X. Wang and W. Choi, *ACS Catalysis*, 2018, 4241-4256.
294. R. Mu, Q. Fu, H. Xu, H. Zhang, Y. Huang, Z. Jiang, S. Zhang, D. Tan and X. Bao, *Journal of the American Chemical Society*, 2011, **133**, 1978-1986.
295. B. T. Sneed, A. P. Young, D. Jalalpoor, M. C. Golden, S. Mao, Y. Jiang, Y. Wang and C.-K. Tsung, *Acs Nano*, 2014, **8**, 7239-7250.
296. C. Han, Y. Lu, J. Zhang, L. Ge, Y. Li, C. Chen, Y. Xin, L. Wu and S. Fang, *Journal of Materials Chemistry A*, 2015, **3**, 23274-23282.
297. C. Han, L. Wu, L. Ge, Y. Li and Z. Zhao, *Carbon*, 2015, **92**, 31-40.
298. Q. Lang, Y. Yang, Y. Zhu, W. Hu, W. Jiang, S. Zhong, P. Gong, B. Teng, L. Zhao and S. Bai, *Journal of Materials Chemistry A*, 2017, **5**, 6686-6694.
299. F. Chen, Q. Yang, Y. Wang, J. Zhao, D. Wang, X. Li, Z. Guo, H. Wang, Y. Deng and C. Niu, *Applied Catalysis B: Environmental*, 2017, **205**, 133-147.
300. F. Shi, L. Chen, M. Chen and D. Jiang, *Chemical Communications*, 2015, **51**, 17144-17147.
301. W. Feng, J. Fang, G. Zhou, L. Zhang, S. Lu, S. Wu, Y. Chen, Y. Ling and Z. Fang, *Molecular Catalysis*, 2017, **434**, 69-79.
302. W. Li, C. Feng, S. Dai, J. Yue, F. Hua and H. Hou, *Applied Catalysis B: Environmental*, 2015, **168**, 465-471.
303. K.-E. Byun, H.-J. Chung, J. Lee, H. Yang, H. J. Song, J. Heo, D. H. Seo, S. Park, S. W. Hwang and I. Yoo, *Nano letters*, 2013, **13**, 4001-4005.
304. S. T. Kochuveedu, Y. H. Jang and D. H. Kim, *Chemical Society Reviews*, 2013, **42**, 8467-8493.
305. L. Jiang, X. Yuan, G. Zeng, J. Liang, Z. Wu and H. Wang, *Environmental Science: Nano*, 2018.
306. H. Li, Y. Zhou, W. Tu, J. Ye and Z. Zou, *Advanced Functional Materials*, 2015, **25**, 998-1013.
307. P. Zhou, J. Yu and M. Jaroniec, *Advanced Materials*, 2014, **26**, 4920-4935.
308. J. Low, C. Jiang, B. Cheng, S. Wageh, A. A. Al-Ghamdi and J. Yu, *Small Methods*, 2017.
309. Z. Jiang, W. Wan, H. Li, S. Yuan, H. Zhao and P. K. Wong, *Advanced Materials*, 2018.
310. H. Xu, J. Yi, X. She, Q. Liu, L. Song, S. Chen, Y. Yang, Y. Song, R. Vajtai and J. Lou, *Applied Catalysis B: Environmental*, 2018, **220**, 379-385.
311. J. Yu, S. Wang, B. Cheng, Z. Lin and F. Huang, *Catalysis Science & Technology*, 2013, **3**, 1782-1789.
312. Y. Li, X. Cheng, X. Ruan, H. Song, Z. Lou, Z. Ye and L. Zhu, *Nano Energy*, 2015, **12**, 775-784.
313. A. Mettenbörger, Y. Gönüllü, T. Fischer, T. Heisig, A. Sasinska, C. Maccato, G. Carraro, C. Sada, D. Barreca and L. Mayrhofer, *Nano energy*, 2016, **19**, 415-427.
314. S. Cao and J. Yu, *The journal of physical chemistry letters*, 2014, **5**, 2101-2107.
315. H. Yan, Y. Chen and S. Xu, *International Journal of hydrogen energy*, 2012, **37**, 125-133.
316. X. Zhang, T. Peng, L. Yu, R. Li, Q. Li and Z. Li, *ACS Catalysis*, 2014, **5**, 504-510.
317. R. Marschall, *Advanced Functional Materials*, 2014, **24**, 2421-2440.
318. X. Li, W. Bi, L. Zhang, S. Tao, W. Chu, Q. Zhang, Y. Luo, C. Wu and Y. Xie, *Advanced Materials*, 2016, **28**, 2427-2431.

319. A. B. Jorge, D. J. Martin, M. T. S. Dhanoa, A. S. Rahman, N. Makwana, J. Tang, A. Sella, F. Corà, S. Firth and J. A. Darr, *The Journal of Physical Chemistry C*, 2013, **117**, 7178-7185.
320. D. J. Martin, K. Qiu, S. A. Shevlin, A. D. Handoko, X. Chen, Z. Guo and J. Tang, *Angewandte Chemie International Edition*, 2014, **53**, 9240-9245.
321. W. Tu, Y. Xu, J. Wang, B. Zhang, T. Zhou, S. Yin, S. Wu, C. Li, Y. Huang and Y. Zhou, *ACS Sustainable Chemistry & Engineering*, 2017, **5**, 7260-7268.
322. X. An, W. Wang, J. Wang, H. Duan, J. Shi and X. Yu, *Physical Chemistry Chemical Physics*, 2018.
323. Y. Chen, B. Lin, W. Yu, Y. Yang, S. M. Bashir, H. Wang, K. Takanabe, H. Idriss and J.-M. Basset, *Chemistry – A European Journal*, 2015, **21**, 10290-10295.
324. A. Indra, P. W. Menezes, K. Kailasam, D. Hollmann, M. Schröder, A. Thomas, A. Brückner and M. Driess, *Chemical Communications*, 2016, **52**, 104-107.
325. G. Zhang, C. Huang and X. Wang, *Small*, 2015, **11**, 1215-1221.
326. K. Sridharan, E. Jang, J. H. Park, J. H. Kim, J. H. Lee and T. J. Park, *Chemistry-A European Journal*, 2015, **21**, 9126-9132.
327. J. Qin and H. Zeng, *Applied Catalysis B: Environmental*, 2017, **209**, 161-173.
328. J. Qin, J. Huo, P. Zhang, J. Zeng, T. Wang and H. Zeng, *Nanoscale*, 2016, **8**, 2249-2259.
329. S. C. Warren and E. Thimsen, *Energy & Environmental Science*, 2012, **5**, 5133-5146.
330. X. Wang, R. Long, D. Liu, D. Yang, C. Wang and Y. Xiong, *Nano Energy*, 2016, **24**, 87-93.
331. A. O. Govorov, J. Lee and N. A. Kotov, *Physical Review B*, 2007, **76**, 125308.
332. I. Majeed, U. Manzoor, F. K. Kanodarwala, M. A. Nadeem, E. Hussain, H. Ali, A. Badshah, J. A. Stride and M. A. Nadeem, *Catalysis Science & Technology*, 2018.
333. C. Han, Y. Gao, S. Liu, L. Ge, N. Xiao, D. Dai, B. Xu and C. Chen, *International Journal of Hydrogen Energy*, 2017, **42**, 22765-22775.
334. J. Jiang, J. Yu and S. Cao, *Journal of colloid and interface science*, 2016, **461**, 56-63.
335. X. Ding, Y. Li, J. Zhao, Y. Zhu, Y. Li, W. Deng and C. Wang, *APL Materials*, 2015, **3**, 104410.
336. X. Ma, Q. Jiang, W. Guo, M. Zheng, W. Xu, F. Ma and B. Hou, *RSC Advances*, 2016, **6**, 28263-28269.
337. H. Zhao, X. Ding, B. Zhang, Y. Li and C. Wang, *Science Bulletin*, 2017, **62**, 602-609.
338. W. Yin, L. Bai, Y. Zhu, S. Zhong, L. Zhao, Z. Li and S. Bai, *ACS applied materials & interfaces*, 2016, **8**, 23133-23142.
339. D. Lu, H. Wang, X. Zhao, K. K. Kondamareddy, J. Ding, C. Li and P. Fang, *ACS Sustainable Chemistry & Engineering*, 2017, **5**, 1436-1445.
340. L. Bi, D. Meng, Q. Bu, Y. Lin, D. Wang and T. Xie, *Physical Chemistry Chemical Physics*, 2016, **18**, 31534-31541.
341. A. Brandt, J. Graesvik, J. P. Hallett and T. Welton, *Green Chem.*, 2013, **15**, 550-583.
342. A. J. Ragauskas, C. K. Williams, B. H. Davison, G. Britovsek, J. Cairney, C. A. Eckert, W. J. Frederick Jr, J. P. Hallett, D. J. Leak, C. L. Liotta, J. R. Mielenz, R. Murphy, R. Templer and T. Tschaplinski, *Science*, 2006, **311**, 484-489.
343. W.-H. Wang, Y. Himeda, J. T. Muckerman, G. F. Manbeck and E. Fujita, *Chemical reviews*, 2015, **115**, 12936-12973.
344. L.-L. Tan, W.-J. Ong, S.-P. Chai and A. R. Mohamed, *Applied Catalysis B: Environmental*, 2015, **166**, 251-259.
345. X. Chang, T. Wang and J. Gong, *Energy & Environmental Science*, 2016, **9**, 2177-2196.
346. G. Dong and L. Zhang, *Journal of Materials Chemistry*, 2012, **22**, 1160-1166.
347. P. Niu, Y. Yang, J. C. Yu, G. Liu and H.-M. Cheng, *Chemical Communications*, 2014, **50**, 10837-10840.
348. S. Zhou, Y. Liu, J. Li, Y. Wang, G. Jiang, Z. Zhao, D. Wang, A. Duan, J. Liu and Y. Wei, *Applied Catalysis B: Environmental*, 2014, **158**, 20-29.
349. W. Yu, D. Xu and T. Peng, *Journal of Materials Chemistry A*, 2015, **3**, 19936-19947.

350. K. Li, B. Peng, J. Jin, L. Zan and T. Peng, *Applied Catalysis B: Environmental*, 2017, **203**, 910-916.
351. J. Mao, T. Peng, X. Zhang, K. Li, L. Ye and L. Zan, *Catalysis Science & Technology*, 2013, **3**, 1253-1260.
352. M. Li, L. Zhang, X. Fan, Y. Zhou, M. Wu and J. Shi, *Journal of Materials Chemistry A*, 2015, **3**, 5189-5196.
353. G. Gao, Y. Jiao, E. R. Waclawik and A. Du, *Journal of the American Chemical Society*, 2016, **138**, 6292-6297.
354. H. Shi, G. Chen, C. Zhang and Z. Zou, *Acs Catalysis*, 2014, **4**, 3637-3643.
355. H. Shi, C. Zhang, C. Zhou and G. Chen, *RSC Advances*, 2015, **5**, 93615-93622.
356. S. Cao, Y. Li, B. Zhu, M. Jaroniec and J. Yu, *Journal of Catalysis*, 2017, **349**, 208-217.
357. H. Park, J. H. Lee, E. H. Kim, K. Y. Kim, Y. H. Choi, D. H. Youn and J. S. Lee, *Chemical Communications*, 2016, **52**, 14302-14305.
358. J. Hong, W. Zhang, Y. Wang, T. Zhou and R. Xu, *ChemCatChem*, 2014, **6**, 2315-2321.
359. Y. Bai, T. Chen, P. Wang, L. Wang, L. Ye, X. Shi and W. Bai, *Solar Energy Materials and Solar Cells*, 2016, **157**, 406-414.
360. Y. He, L. Zhang, B. Teng and M. Fan, *Environmental science & technology*, 2014, **49**, 649-656.
361. H. Li, Y. Gao, X. Wu, P.-H. Lee and K. Shih, *Applied Surface Science*, 2017, **402**, 198-207.
362. Y. Huang, Y. Wang, Y. Bi, J. Jin, M. F. Ehsan, M. Fu and T. He, *RSC Advances*, 2015, **5**, 33254-33261.
363. M. R. Hoffmann, S. T. Martin, W. Choi and D. W. Bahnemann, *Chemical reviews*, 1995, **95**, 69-96.
364. M. Humayun, Y. Qu, F. Raziq, R. Yan, Z. Li, X. Zhang and L. Jing, *Environmental science & technology*, 2016, **50**, 13600-13610.
365. Q. Zheng, D. P. Durkin, J. E. Elenewski, Y. Sun, N. A. Banek, L. Hua, H. Chen, M. J. Wagner, W. Zhang and D. Shuai, *Environmental science & technology*, 2016, **50**, 12938-12948.
366. Y. Cui, Z. Ding, P. Liu, M. Antonietti, X. Fu and X. Wang, *Physical Chemistry Chemical Physics*, 2012, **14**, 1455-1462.
367. Y. Fu, T. Huang, L. Zhang, J. Zhu and X. Wang, *Nanoscale*, 2015, **7**, 13723-13733.
368. Z. Li, J. Wang, K. Zhu, F. Ma and A. Meng, *Materials Letters*, 2015, **145**, 167-170.
369. Y. Yang, W. Guo, Y. Guo, Y. Zhao, X. Yuan and Y. Guo, *Journal of hazardous materials*, 2014, **271**, 150-159.
370. X. Xiao, J. Wei, Y. Yang, R. Xiong, C. Pan and J. Shi, *ACS Sustainable Chemistry & Engineering*, 2016, **4**, 3017-3023.
371. J. Wu, X. Shen, X. Miao, Z. Ji, J. Wang, T. Wang and M. Liu, *European Journal of Inorganic Chemistry*, 2017, **2017**, 2845-2853.
372. X. Li, T. Wan, J. Qiu, H. Wei, F. Qin, Y. Wang, Y. Liao, Z. Huang and X. Tan, *Applied Catalysis B: Environmental*, 2017, **217**, 591-602.
373. J. Luo, X. Zhou, L. Ma and X. Xu, *Applied Surface Science*, 2016, **390**, 357-367.
374. X. Yang, H. Tang, J. Xu, M. Antonietti and M. Shalom, *ChemSusChem*, 2015, **8**, 1350-1358.
375. H. Katsumata, T. Sakai, T. Suzuki and S. Kaneco, *Industrial & Engineering Chemistry Research*, 2014, **53**, 8018-8025.
376. C. Tang, E. Liu, J. Fan, X. Hu, Y. Ma and J. Wan, *RSC Advances*, 2015, **5**, 91979-91987.
377. L. Zhou, W. Zhang, L. Chen and H. Deng, *Journal of colloid and interface science*, 2017, **487**, 410-417.
378. L. Shi, L. Liang, F. Wang, M. Liu and J. Sun, *Journal of materials science*, 2015, **50**, 1718-1727.
379. Y. Su, Y. Zhao, Y. Zhao, J. Lang, X. Xin and X. Wang, *Applied Surface Science*, 2015, **358**, 213-222.
380. D. Vidyasagar, S. G. Ghugal, A. Kulkarni, P. Mishra, A. G. Shende, Jagannath, S. S. Umare and R. Sasikala, *Applied Catalysis B: Environmental*, 2018, **221**, 339-348.

381. A. Zada, Y. Qu, S. Ali, N. Sun, H. Lu, R. Yan, X. Zhang and L. Jing, *Journal of hazardous materials*, 2018, **342**, 715-723.
382. R. C. Pawar, Y. Pyo, S. H. Ahn and C. S. Lee, *Applied Catalysis B: Environmental*, 2015, **176**, 654-666.
383. R. C. Pawar, S. Kang, S. H. Ahn and C. S. Lee, *Rsc Advances*, 2015, **5**, 24281-24292.
384. J. Xue, S. Ma, Y. Zhou and Q. Wang, *Rsc Advances*, 2015, **5**, 88249-88257.
385. J. Wu, Y. Zhang, T. Wang, Y. Xin and D. Ma, *Materials Research Bulletin*, 2017.
386. D. Peng, H. Wang, K. Yu, Y. Chang, X. Ma and S. Dong, *RSC Advances*, 2016, **6**, 77760-77767.
387. J. Xue, S. Ma, Y. Zhou, Z. Zhang and M. He, *ACS Applied Materials & Interfaces*, 2015, **7**, 9630-9637.
388. M. A. Gondal, A. A. Adeseda, S. G. Rashid, A. Hameed, M. Aslam, I. M. I. Ismail, U. Baig, M. A. Dastageer, A. R. Al-Arfaj and A. U. Rehman, *Journal of Molecular Catalysis A: Chemical*, 2016, **423**, 114-125.
389. G. Darabdhara and M. R. Das, *Chemosphere*, 2018.
390. J. Gao, J. Wang, X. Qian, Y. Dong, H. Xu, R. Song, C. Yan, H. Zhu, Q. Zhong and G. Qian, *Journal of Solid State Chemistry*, 2015, **228**, 60-64.
391. Y. Bao and K. Chen, *Molecular Catalysis*, 2017, **432**, 187-195.
392. J. Wang, L. Tang, G. Zeng, Y. Liu, Y. Zhou, Y. Deng, J. Wang and B. Peng, *ACS Sustainable Chemistry & Engineering*, 2016, **5**, 1062-1072.
393. G. Jiang, X. Li, M. Lan, T. Shen, X. Lv, F. Dong and S. Zhang, *Applied Catalysis B: Environmental*, 2017, **205**, 532-540.
394. Y. Sun, T. Xiong, Z. Ni, J. Liu, F. Dong, W. Zhang and W.-K. Ho, *Applied Surface Science*, 2015, **358**, 356-362.
395. Y. Ma, J. Li, E. Liu, J. Wan, X. Hu and J. Fan, *Applied Catalysis B: Environmental*, 2017, **219**, 467-478.
396. M. Ou, S. Wan, Q. Zhong, S. Zhang, Y. Song, L. Guo, W. Cai and Y. Xu, *Applied Catalysis B: Environmental*, 2018, **221**, 97-107.
397. X. Yang, Z. Chen, J. Xu, H. Tang, K. Chen and Y. Jiang, *ACS applied materials & interfaces*, 2015, **7**, 15285-15293.
398. H. Li, Y. Sun, B. Cai, S. Gan, D. Han, L. Niu and T. Wu, *Applied Catalysis B: Environmental*, 2015, **170**, 206-214.
399. Y. Liang, S. Lin, L. Liu, J. Hu and W. Cui, *Applied Catalysis B: Environmental*, 2015, **164**, 192-203.
400. H. Ji, L. Lyu, L. Zhang, X. An and C. Hu, *Applied Catalysis B: Environmental*, 2016, **199**, 230-240.
401. Y. Bao and K. Chen, *Nano-Micro Letters*, 2016, **8**, 182-192.
402. Y. Chang, Z. Liu, X. Shen, B. Zhu, D. K. Macharia, Z. Chen and L. Zhang, *Journal of Hazardous Materials*, 2018, **344**, 1188-1197.
403. Z. Xu, S. Xu, N. Li, F. Wu, S. Chen, W. Lu and W. Chen, *ACS Sustainable Chemistry & Engineering*, 2017, **5**, 9667-9672.
404. D. P. Subagio, M. Srinivasan, M. Lim and T.-T. Lim, *Applied Catalysis B: Environmental*, 2010, **95**, 414-422.
405. M. Sierra, E. Borges, P. Esparza, J. Méndez-Ramos, J. Martín-Gil and P. Martín-Ramos, *Science and Technology of advanced MaTerialS*, 2016, **17**, 659-668.
406. T. Sano, S. Tsutsui, K. Koike, T. Hirakawa, Y. Teramoto, N. Negishi and K. Takeuchi, *Journal of materials chemistry A*, 2013, **1**, 6489-6496.
407. A. Nikokavoura and C. Trapalis, *Applied Surface Science*, 2018, **430**, 18-52.
408. S. Verma, R. B. N. Baig, M. N. Nadagouda and R. S. Varma, *Catalysis Today*, 2017.
409. J. Liu, H. Wang and M. Antonietti, *Chemical Society Reviews*, 2016, **45**, 2308-2326.
410. H. Hiramatsu and F. E. Osterloh, *Chemistry of Materials*, 2004, **16**, 2509-2511.
411. H. Duan, D. Wang and Y. Li, *Chemical Society Reviews*, 2015, **44**, 5778-5792.